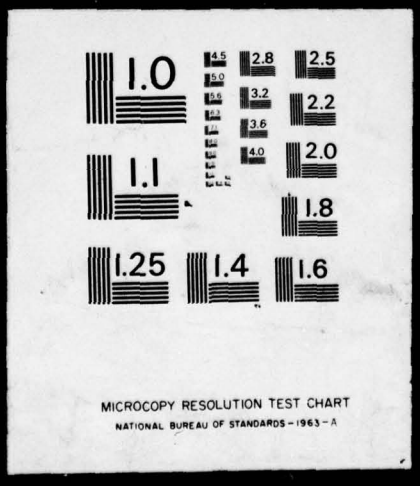
AD-A033 680 TORONTO UNIV (ONTARIO) INST FOR AEROSPACE STUDIES F/G 4/1
DIAGNOSTICS WITH ROCKETBORNE ELECTRON BEAM FLUORESCENCE PROBES.(U)
OCT 75 J H DELEEUW, W E DAVIES, A A HAASZ AF-AFOSR-2091-71
UNCLASSIFIED UTIAS-197 AFOSR-TR-76-1408 NL

1 OF 2
AD A033680



1 OF 2

AD
A033680



ADA033680

INSTITUTE
FOR
AEROSPACE STUDIES

UNIVERSITY OF TORONTO

AFOSR - TR - 76 - 1408

DIAGNOSTICS WITH ROCKETBORNE ELECTRON BEAM FLUORESCENCE PROBES

by

J. H. deLeeuw, W.E.R. Davies, A. A. Haasz, J. I. Unger

DDC
RECEIVED
DEC 27 1976
A

Approved for public releast; distribution unlimited.

October, 1975

UTIAS Report No. 197
CN ISSN 0082-5255

Qualified requestors may obtain additional copies from the Defense Documentation Center, all others should apply to the National Technical Information Service.

Conditions of Reproduction

Reproduction, translation, publication, use and disposal in whole or in part by or for the United States Government is permitted.

AIR FORCE OFFICE OF SCIENTIFIC RESEARCH (AFSC)
NOTICE OF TRANSMITTAL TO DDC
This technical report has been reviewed and is approved for public release IAW AFR 190-12 (7b).
Distribution is unlimited.
A. D. BLOSE
Technical Information Officer

DIAGNOSTICS WITH ROCKETBORNE ELECTRON BEAM FLUORESCENCE PROBES

by

J. H. deLeeuw, W.E.R. Davies, A.A. Haasz, J. I. Unger

ACCESSION for
NTIS White Section
DDC Buff Section
UNANNOUNCED
JUSTIFICATION
BY
DISTRIBUTION/AVAILABILITY CODES
Dist. AVAIL. and/or SPECIAL

October, 1975

UTIAS Report No. 197
CN ISSN 0082-5255

Acknowledgements

Our thanks are extended to the members of the UTIAS Rocket Shop and the UTIAS Workshop. In particular, we thank Mr. J. Leffers for his valuable contributions throughout the development of the EBFP instrument.

The enlightening discussions with Dr. G. E. McMichael are gratefully acknowledged. Also, the assistance of Mr. S. Raimondo with the computer calculations is appreciated.

This work was supported by the National Research Council of Canada under Grant No. A3942, and by the United States Air Force Office of Scientific Research under Grant No. 71-2091C.

Abstract

An Electron Beam Fluorescence Probe (EBFP) has been developed for rocket flight applications in the 65 - 200 km altitude range. The EBFP is a non-perturbing probe which is capable of measuring vibrational and rotational temperatures as well as neutral gas species concentrations remote from the rocket payload. The spatial resolution of the probe is approximately equal to the beam diameter (1 - 2 mm). The instrument employs a 2.5 keV energy electron beam to induce fluorescence in the ambient gas. The resulting radiation is analyzed with a spectrally selective electro-optical detection system. Several versions of the EBFP were flown on Black Brant rockets from Fort Churchill, Manitoba, Canada; the results from these flights as well as the development of the instrumentation are discussed.

TABLE OF CONTENTS

		Page
	Acknowledgement	ii
	Abstract	iii
1.	INTRODUCTION	1
2.	ELECTRON BEAM FLUORESCENCE PROBE	2
	2.1 Electron Beam Diagnostic Technique	2
	2.2 Species Concentration and Rotational and Vibrational Temperature Measurements	3
	2.3 Effect of Reflected Molecules on Rotational Temperature Measurements in Free Molecular Flow	6
3.	EBFP ELECTRON GUNS FOR ROCKET FLIGHT	11
	3.1 Electron Gun Types	12
	3.2 Operating Pressure Range and High Voltage Breakdown for Electron Guns	13
	3.3 Cathodes for Electron Guns	14
	3.4 Selection of the Flight Electron Gun	14
	3.5 Focussing the Electron Beam	15
	3.6 Location of the Observation Region	17
	3.7 Electron Beam Collector and Optical Backstop	18
4.	OPTICAL DETECTION SYSTEM FOR EBFP	19
	4.1 Interference Filters and Fibre Optics	20
	4.2 Photomultiplier Tubes	20
	4.3 Spectral Response Function Calibration for EBFP	21
	4.4 Optical Signal Characteristics	23
	4.5 Background Light and Its Rejection	24
5.	ROCKET EXPERIMENTS AND FLIGHT RESULTS	25
	5.1 Initial Flight of EBFP: Black Brant Rocket AEF-II-118	25
	5.2 Black Brant Rockets VB-32, VB-28, VB-39 Employing the Multi-Spectral Channel Fibre Optic System	27
6.	CONCLUSIONS	29
	REFERENCES	31
	APPENDIX A: REVIEW OF ATMOSPHERIC MEASUREMENT TECHNIQUES	
	APPENDIX B: RADIATION DISTRIBUTION IN THE N_2^+ 1N SYSTEM VIBRATIONAL BANDS	
	APPENDIX C: SOURCES OF ERRORS FOR EBFP DENSITY AND TEMPERATURE MEASUREMENTS	
	APPENDIX D: ELECTRONIC SUBSYSTEMS FOR THE EBFP	
	FIGURES	

1. INTRODUCTION

The electron beam fluorescence technique has been used extensively in laboratory investigations of low density gases. In this regard it has proved to be a valuable diagnostic method for flow visualization and measurements of rotational and vibrational temperatures as well as determinations of local gas specie concentrations. The application of the technique to upper altitudes of the atmosphere was first carried out by UTIAS in 1969, resulting in measurements of rotational temperature and nitrogen density (Refs. 1 and 2). Since that time, other experimenters have flown electron beam probes and UTIAS has continued its work with rocket flights carrying a variety of electron beam instruments.

A review of some of the techniques available for investigating the upper atmosphere (see Appendix A) shows that although much effort has been expended in the design and application of instrumentation, much work remains to be done in the region from 65 to 200 km. A continuing lack of suitable techniques has traditionally plagued measurement of this area and the difficulties involved in providing adequate diagnostics for this region should not be underestimated. From 65 to 300 km the density varies over a dynamic range of about 7 decades with the temperature varying from approximately 200K to 1400K. The composition supplies an additional variable as evidenced by the change in molecular weight from 28.96 at 65 km to 22.66 at 200 km.

Free molecular conditions for a 10 cm body are not achieved until about 110 km. This further complicates the problem of designing a single instrument that can adequately cover the altitude range under discussion whilst moving at sounding rocket velocity (1 - 4 km/s).

Apart from the electron beam diagnostic method, direct measurements of temperature in the 65 - 200 km region have been made by auroral observation, which provides only an integrated measurement along the line of sight (it is also difficult to measure the auroral height with accuracy). Temperature determinations can also be derived from pressure, density or scale height measurements using an appropriate model. However, because of the variables involved, some assumptions or additional measurements are required before the temperature can be calculated explicitly.

Atmospheric models are continuously being refined as more data become available; models for the high altitude region (above 50 km) especially, have been revised drastically in recent years. Because of the lack of adequate instrumentation and the expense for launching the apparatus to the required altitude there is still a real need for reliable data in the 50 - 200 km region, a range that at the present time can be covered only by sounding rockets.

The electron beam fluorescence technique has been developed to fill the diagnostics gap in the 65 - 200 km region; it is the only current technique permitting direct and local measurements of rotational and vibrational temperature, density and composition, simultaneously.

In essence, this report presents a description of the Electron Beam Fluorescence Probe (EBFP) technique (Sec. 2) and elaborates on the design and

development of a rocket-borne EBFP instrument. Section 3 deals with the selection of an electron gun for rocket flights, and Section 4 details the optical detection system for the EBFP. A comprehensive summary of the instruments flown up to date and the experimental results obtained is presented in Section 5.

2. ELECTRON BEAM FLUORESCENCE PROBE

2.1 Electron Beam Diagnostic Technique

The electron beam fluorescence probe (EBFP) essentially consists of a high energy electron beam (keV energy range) used to induce fluorescence in the gas sample to be studied, and a spectrally selective electro-optical detection system which analyzes the resulting electromagnetic radiation.

The major advantage of the probe lies in the fact that the point of observation in the flow can be located sufficiently far away from the probe structural components and thus probe induced disturbances can be avoided. This is of particular importance for rocket flight application where aerodynamic disturbances occur due to the motion of the payload through the ambient atmosphere. Another advantage from the point of view of rocket research is that by proper selection of the spectral features to be analyzed it is possible to obtain static measurements of the gas properties independent of rocket velocity. In order to achieve this, emissions resulting from optically allowed direct excitation-emission transitions with transition probabilities greater than about 10^7 have to be selected. This implies that at typical payload velocities of 1 - 2 km/s the displacement of the observation point during the time interval between the electron-gas particle impact and the radiation emission is approximately 0.1 - 0.2 mm. This is an order of magnitude less than the nominal beam diameter (about 1 - 2 mm) which in most cases defines the spatial resolution of the instrument. Another advantage of the EBFP is that it is capable of measuring the concentration of unstable atomic species such as atomic oxygen which poses difficulties for most 'material probes'.

Although the EBFP is a versatile and powerful diagnostic tool, its usefulness is limited to low density studies. The upper density limit is a function of several parameters such as the type of species present in the gas and the exciting electron beam energy. The gas composition and the beam energy will determine the secondary electron production rate, the primary beam attenuation due to scattering by gas particles as well as the collision quenching rate of gas particles in excited states. These secondary effects, as well as several others discussed in detail by Muntz (Ref. 3), can in some cases introduce nonlinearities in the emission intensity versus gas density curves. For example, the fluorescence contribution by secondary electrons is a critical function of the relative dimensions of the secondary electron mean free path and the observation region. The densities, total and partial, at which the effect of secondary processes becomes significant vary for different spectral characteristics.

The extent of beam attenuation estimated by the Thomas-Fermi statistical method (Ref. 4) is given in Fig. 1 for elastic scattering by nitrogen over a 10 cm beam path length; the curves yield attenuation as a function of pressure for several beam energies. For example, at 1 mtorr N_2 pressure the

fraction of 2.5 keV beam electrons that have not encountered elastic scattering collisions is about 97%. This is a conservative estimate since small angle scattering which does not contribute to appreciable beam spreading may be acceptable. However, it should be noted that inelastic scattering and multiple elastic scattering was not included; inelastic scattering tends to dominate at small angles. Experimental measurements of beam attenuation obtained from the laboratory static nitrogen calibrations of the EBFP instruments flown on Black Brant rockets VB-32, VB-28 and VB-39 are shown in Fig. 2; the theoretical curve based on Thomas-Fermi elastic scattering is also included. The difference between the experimental curves, of course, results from the fact that different beam collector configurations were employed. It should be noted that the simple scattering theory is only useful in determining the approximate upper pressure limit at which beam scattering starts to become important. At pressures above about 3 mtorr the simple elastic scattering prediction underestimates the beam attenuation. This is probably due to the fact that at such pressures the effect of multiple scattering collisions becomes significant. The experimental curves in Fig. 2 indicate that beam attenuation in nitrogen for a 2.5 keV beam of 10 cm path is negligible at densities below about 1 - 2 equiv. mtorr.* This corresponds to an altitude of about 90 km. However, during actual flights, because of the presence of shock waves produced by the EBFP gun housing and back stop as the apparatus travels through the continuum flow regime, the beam electrons encounter higher density regions resulting in greater beam attenuation. This effect can be observed by comparing the preflight calibration in Fig. 2 and in-flight results for AEF-II-118 shown in Fig. 3.

How does primary beam electron scattering affect the EBFP results? As long as the observation region is large enough so that the fluorescence produced by all the beam electrons, including the scattered ones, is collected by the optical system and the total beam current passing through the observation volume is known then the probe measurements will not be affected by scattering. However, if scattering outside of the observation volume occurs, the interpretation of the results becomes difficult.

2.2 Species Concentration and Rotational and Vibrational Temperature Measurements

The fluorescence induced by a high energy electron beam is a function of the thermodynamic variables of the gas. Under desirable operating conditions of the EBFP, when the effect of secondary processes is negligible, it is possible to obtain species concentrations by measuring the intensities of spectral emissions produced by the different gas components. The characteristic spectral features are chosen in such a way as to minimize the optical interference among channels. Narrow band interference filters are used to locate the channels in the fluorescence spectrum.

In the case of molecular species where the spectral features exhibit vibrational and rotational fine structure it is possible to determine the vibrational and rotational temperatures by examining the fine structure of the emissions. For nitrogen containing mixtures the N_2^+ First Negative (1N) system has been extensively used in laboratory investigations and recently in upper atmospheric studies for the determination of these temperatures.

A detailed analysis of fluorescence induced by a 2.5 keV energy electron beam in molecular nitrogen and molecular and atomic oxygen was

*Throughout this paper densities are expressed in terms of equivalent pressures at 300K temperature.

performed by Haasz (Ref. 5), and based on the results of that study, the following spectral characteristics in the visible spectral region were recommended for upper atmospheric diagnostics with the EBFP. In the altitude range of interest (80 km - 200 km), the major neutral constituents are N_2, O_2 and O_1.

N_2 concentration measurements:

N_2^+ 1N (0,1) band (head at 4278Å)

Filter: 4270Å, 30Å HBW*

O_2 concentration measurements:

(a) O_2^+ 1N (5250Å) bands, (2,0) sequence

Filter: 5250Å, 60Å HBW

(b) O_2^+ 1N (5600Å) bands, (1,0) sequence

Filter: 5590Å, 70Å HBW

O_1 concentration measurements:

(a) OII 4351Å line

Filter: 4351Å ± 1Å†, 6Å HBW

(b) OII 4415Å and 4417Å lines

Filter: 4416Å ± 1Å†, 6Å HBW

N_2 rotational temperature measurements:

N_2^+ 1N (0,1) band (head at 4278Å)

Filter No. 1: 4254Å ± 1Å†, 8Å HBW

Filter No. 2: 4271Å ± 1Å†, 8Å HBW

N_2 vibrational temperature measurements:

N_2^+ 1N (0,1) band (head at 4278Å)

N_2^+ 1N (1,2) band (head at 4236Å)

Filter No. 1: 4270Å, 30Å HBW

Filter No. 2: 4230Å, 30Å HBW

---

*HBW: "half intensity bandwidth".

† The long wavelength tolerance limit should be used when constructing the filters; shorter wavelength may then be obtained if necessary by changing the angle of the light incident on the filter.

The studies of Ref. 5 concluded that: "For the characteristic emissions selected for upper atmospheric composition and temperature measurements, with the exception of the O_2^+ 1N system, the effect of collisional quenching is expected to be negligible at densities below 10 equiv. mtorr corresponding to altitudes above 80 km. For the O_2^+ 1N system the quenching density,* in both air and O_2, is approximately 50 equiv. mtorr; this would result in a 20% reduction of the O_2^+ 1N system radiation at 10 equiv. mtorr total pressure. However, for the O_2^+ 1N emission, the effect of secondary electron excitations reduces the upper total density limit for O_2 concentration measurements to about 1 equiv. mtorr (corresponding to 95 km altitude). At about 4 equiv. mtorr total pressure (85 km altitude), the contribution of the O_2^+ 1N (5600Å) band group radiation by secondaries is approximately 15%. The effect of secondary electron excitation on the N_2^+ 1N (0,1) band and the OII 4351Å and OII 4416Å lines is expected to be negligible at altitudes above 80 km."

It should be mentioned that the vibrational bands of the O_2^+ 2N system (in the 2000Å to 4000Å wavelength range) may also be used for molecular oxygen concentration and vibrational temperature measurements. A spectral trace of the O_2^+ 2N system appears in Ref. 5; the intensities of these bands were approximately 10^{-4} of the N_2^+ 1N (0,0) band. The radiation intensity of this system was found to vary linearly with pressure up to 300 mtorr by Petrie, Boiarski and Lazdinis (Ref. 6), which implies that collisional quenching is negligible below 300 mtorr pressures.

The sensitivities of the various EBFP channels to molecular nitrogen and molecular oxygen were determined for all the EBFP instruments launched to date by laboratory calibrations under static conditions in N_2, O_2 and air. By calibrating in air it is possible to determine the extent of gasdynamic interference among the gas species. For the EBFP apparatus flown on VB-28 (Ref. 5) it was found that the selected spectral features were not affected by the presence of the other specie in an N_2 - O_2 gas mixture (78% N_2, 21% O_2) for total pressures below about 1 mtorr.

Since static gas calibrations of the EBFP in atomic oxygen are difficult, the sensitivity of the atomic oxygen concentration measuring channel to O_1 gas can be determined from a knowledge of the excitation cross-section of the atomic oxygen emissions of interest (published in Ref. 5) and the spectral response function of the channel. It should be noted, however, that in gas mixtures containing both atomic and molecular oxygen it is possible to excite atomic lines from both the atomic and molecular species. Thus, the contribution to the O_1 channel signal due to the presence of O_2 has to be subtracted. Further corrections will have to be made for mixtures containing N_2 as well, as is the case in the upper atmosphere altitude range of interest.

The selection of the interference filter locations and half intensity bandwidths for N_2 and O_2 concentration measurements should be made in such a way as to minimize the rotational temperature effects on the transmitted light intensity. This effect is expected to be negligible for the O_2 measurements where the filter includes several vibrational bands. However, for N_2, where only one vibrational band is viewed, corrections may have to be made. This can be done by analyzing the intensity distribution in the rotational lines of the vibrational

*"Quenching density" is the density at which the radiation intensity is reduced by collisional quenching to 1/2 the radiation intensity that would occur in the absence of collisional quenching.

band in question as a function of rotational temperature. Such an analysis using Muntz's (Ref. 7) theoretical approach is presented in Appendix B for the N_2^+ 1N (0,1) and (1,2) bands for several rotational temperatures. The intensities have been normalized to yield total intensities of 1.0 and 0.124 for the (0,1) and (1,2) bands, respectively.

As mentioned before, rotational and vibrational temperature measurements for a molecular gas can be made by analyzing the light intensity distribution in the rotational lines and vibrational bands, respectively, of characteristic emissions for which the excitation-emission processes are understood. For the rocket flight EBFP instruments the rotational temperature, T_R, was measured by locating two narrow band interference filters in the N_2^+ 1N (0,1) vibrational band and obtaining the ratio of the transmitted radiation intensities. Filter locations were selected in such a way as to obtain optimum conditions for both the transmitted light levels and the sensitivity in the intensity ratio with respect to T_R. A theoretical calibration curve for intensity ratio versus T_R can be obtained from the rotational energy distribution analysis presented in Appendix B. Such a calibration curve will be presented in Sec. 2.3 where the effect of reflected particles as well as the effect of the N_2^+ 1N (1,2) band radiation on rotational temperature measurements will be considered.

2.3 Effect of Reflected Molecules on Rotational Temperature Measurements in Free Molecular Flow

At high altitudes, where the mean free path of the ambient gas is many times the apparatus dimension, the flow is free molecular. Under such conditions, gas molecules that have first struck portions of the payload may be reflected into the observation region resulting in an increase of the fluorescent signal. An estimate of the effect of molecules reflected off the rocket payload surfaces into the EBFP observation region, and thus contributing to the emitted radiation, can be obtained by the following analysis. Let it be assumed that:

1. The incoming particles striking the payload surfaces undergo diffuse reflections (that is, the distribution of particles leaving the surfaces is isentropic and is characterized by a Maxwellian velocity distribution at a temperature T').

2. In addition, perfect accommodation of the kinetic and rotational degrees of freedom occurs at the reflecting surface (that is, the temperature T' and T_R are equal to the surface temperature T_w, T_R being the rotational temperature).

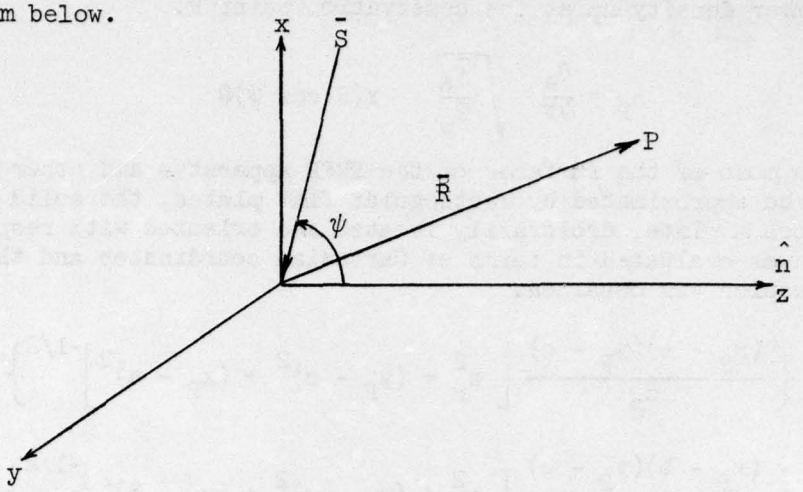
3. No adsorption, association or dissociation occurs at the surfaces.

The incident particle flux on the surface of a plate is given by,

$$\frac{n_a \, c_{m_a}}{2\sqrt{\pi}} \chi(S \cos \psi) \tag{2.1}$$

where n_a is the number density of the incident (in this case ambient) particles, c_{m_a} is the most probable velocity associated with the incident particles, S is

the speed ratio and ψ is the angle of incidence of the particles as shown in the diagram below.



The function $\chi(S \cos \psi)$ is defined as,

$$\chi(S \cos \psi) = \exp(-S^2 \cos^2 \psi) + \sqrt{\pi}\, S \cos \psi \, [1 + \operatorname{erf}(S \cos \psi)] \qquad (2.2)$$

Using the assumptions made earlier, one can describe the gas particles striking the surface as being contained in an imaginary reservoir behind the surface and characterized by a Maxwellian velocity distribution function at rest. The density and temperature of the gas in the "reservoir" are n_w and T_w, respectively. Thus, in order to satisfy the conservation of mass requirement at the surface the incident flux must be equal to the reflected flux. Note that this analysis does not take into account adsorption nor recombination of species at the surface.

$$\frac{n_a \, c_{m_a}}{2\sqrt{\pi}} \, \chi(S \cos \psi) = \frac{n_w \, c_{m_w}}{2\sqrt{\pi}} \, \chi(0) \qquad (2.3)$$

From this relation the number density n_w can be obtained in terms of T_w and incident gas parameters.

$$n_w = n_a \sqrt{T_a/T_w} \; \chi(S \cos \psi) \qquad (2.4)$$

The contribution to the net reflected number density at the EBFP observation point P by an elemental surface area dA is given by,

$$dn_P = n_w (d\Omega/4\pi) \qquad (2.5)$$

where

$$d\Omega = dA \cos \phi / R^2 \qquad (2.6)$$

Thus

$$dn_P = \frac{n_a}{4\pi} \sqrt{\frac{T_a}{T_w}} \; \chi(S \cos \psi) d\Omega \qquad (2.7)$$

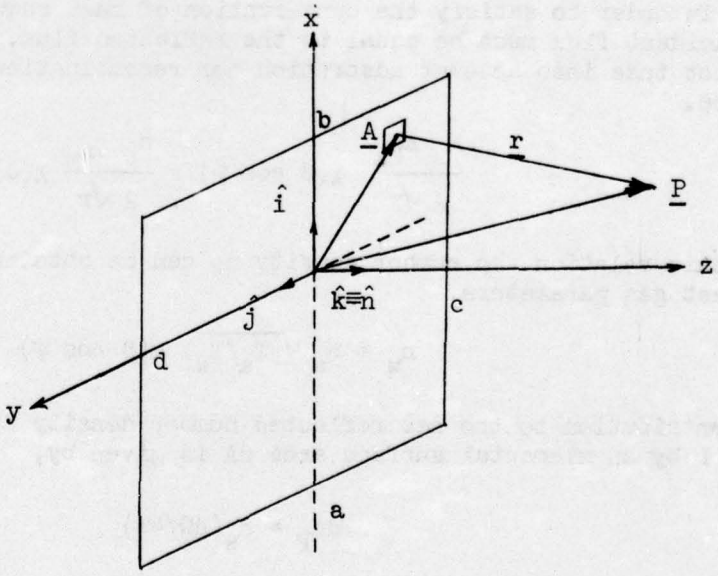
Therefore, a finite surface area, subtending a solid angle Ω, will contribute a reflected number density n_P at the observation point P.

$$n_P = \frac{n_a}{4\pi} \sqrt{\frac{T_a}{T_w}} \quad \chi(S \cos \psi)\Omega \tag{2.8}$$

Since most of the surfaces of the EBFP apparatus and other payload structures can be approximated by rectangular flat plates, the solid angle Ω subtended by such a plate, arbitrarily located and oriented with respect to a field point P, was evaluated in terms of Cartesian coordinates and the following expression was obtained.

$$\begin{aligned}
\Omega = &\tan^{-1}\left\{\frac{(x_P - a)(y_P - c)}{z_P}\left[z_P^2 + (y_P - c)^2 + (x_P - a)^2\right]^{-1/2}\right\} \\
&- \tan^{-1}\left\{\frac{(x_P - b)(y_P - c)}{z_P}\left[z_P^2 + (y_P - c)^2 + (x_P - b)^2\right]^{-1/2}\right\} \\
&- \tan^{-1}\left\{\frac{(x_P - a)(y_P - d)}{z_P}\left[z_P^2 + (y_P - d)^2 + (x_P - a)^2\right]^{-1/2}\right\} \\
&+ \tan^{-1}\left\{\frac{(x_P - b)(y_P - d)}{z_P}\left[z_P^2 + (y_P - d)^2 + (x_P - b)^2\right]^{-1/2}\right\}
\end{aligned} \tag{2.9}$$

The coordinate system is defined in the diagram below:



$$\underline{A} = \hat{i}\, x_A + \hat{j}\, y_A$$

$$\underline{P} = \hat{i}\, x_P + \hat{j}\, y_P + \hat{k}\, z_P$$

$$\underline{r} = \underline{P} - \underline{A}$$

$$d\Omega = \frac{\hat{n} \cdot \underline{r}}{|\underline{r}|^3}$$

$$d\Omega = \frac{z_P\, dx_A\, dy_A}{[(x_P - x_A)^2 + (y_P - y_A)^2 + z_P^2]^{3/2}}$$

With a knowledge of the total solid angle subtended by all the surfaces contributing to the reflected particle density at the observation point P, the partial densities of the ambient and reflected particles can be expressed, respectively, as:

$$n_a = \frac{1}{\left[1 + \frac{\Omega}{4\pi}\sqrt{\frac{T_a}{T_w}}\,\chi(S\cos\psi)\right]} \tag{2.10}$$

$$n_{refl} = \frac{\frac{\Omega}{4\pi}\sqrt{\frac{T_a}{T_w}}\,\chi(S\cos\psi)}{\left[1 + \frac{\Omega}{4\pi}\sqrt{\frac{T_a}{T_w}}\,\chi(S\cos\psi)\right]} \tag{2.11}$$

For the EBFP apparatus flown on Black Brant Rocket AEF-II-118 Ω was estimated to be 1.1 sr. For the special case when the angle of attack, α, is zero (corresponding to $\psi = 90°$), where the reduction of flight data was done, the variation of the partial density of the reflected molecules as a function of ambient temperature is shown in Fig. 4 for $\Omega = 1.0$ and 1.1. The payload surface temperature was $T_w = 300K$. The effect of 10° variation in angle of attack for different speed ratios on n_{refl} as a function of T_a is illustrated in Fig. 4.

As discussed in Section 2.2, rotational temperature measurements with the EBFP can be made by measuring the relative intensity ratio of light transmitted through two narrow band interference filters located in the N_2^+ 1N (0,1) vibrational band. A theoretical calibration curve for light intensity ratio versus T_R was evaluated for the apparatus flown on AEF-II-118. For the prediction the effect of reflected molecules as well as the contribution of the N_2^+ 1N (1,2) band radiation was considered.

Expressions for the relative emission intensities of the rotational lines originating from the K' level for the P and R branches of the N_2^+ 1N (0,1) and (1,2) vibrational bands were derived in Appendix B and are given below for a temperature T_R. (For notation refer to Appendix B.)

$$I_{K'}^{P(0,1)} = \frac{\phi(K')(K'+1)\nu_{P(0,1)}^4}{\left[(K'+1)\,\nu_{P(0,1)}^4 + K'\nu_{R(0,1)}^4\right]} \tag{2.12}$$

$$I_{K'}^{R(0,1)} = \frac{\phi(K')\,K'\nu_{R(0,1)}^4}{\left[(K'+1)\,\nu_{P(0,1)}^4 + K'\nu_{R(0,1)}^4\right]} \tag{2.13}$$

$$I^{P(1,2)}_{K'} = \frac{0.124\ \phi(K')(K'+1)\ \nu^4_{P(1,2)}}{[(K'+1)\ \nu^4_{P(1,2)} + K'\nu^4_{R(1,2)}]} \tag{2.14}$$

$$I^{R(1,2)}_{K'} = \frac{0.124\ \phi(K')\ K'\nu^4_{R(1,2)}}{[(K'+1)\ \nu^4_{P(1,2)} + K'\nu^4_{R(1,2)}]} \tag{2.15}$$

Assuming that for the incident nitrogen molecules the kinetic and rotational degrees of freedom are in equilibrium ($T_a = T_R$), then for a particular T_a the relative light emission from level K' in the observation region of the EBFP due to ambient and reflected molecules can be expressed as:

$$I^{P(0,1)}_{K'amb,refl} = \frac{(K'+1)\ \nu^4_{P(0,1)}}{[(K'+1)\ \nu^4_{P(0,1)} + K'\nu^4_{R(0,1)}]} \{\phi(K')_{T_a} n_a + \phi(K')_{T_w} n_{refl}\} \tag{2.16}$$

$$I^{R(0,1)}_{K'amb,refl} = \frac{K'\nu^4_{R(0,1)}}{[(K'+1)\ \nu^4_{P(0,1)} + K'\nu^4_{R(0,1)}]} \{\phi(K')_{T_a} n_a + \phi(K')_{T_w} n_{refl}\} \tag{2.17}$$

$$I^{P(1,2)}_{K'amb,refl} = \frac{0.124\ (K'+1)\ \nu^4_{P(1,2)}}{[(K'+1)\ \nu^4_{P(1,2)} + K'\nu^4_{R(1,2)}]} \{\phi(K')_{T_a} n_a + \phi(K')_{T_w} n_{refl}\} \tag{2.18}$$

$$I^{R(1,2)}_{K'amb,refl} = \frac{0.124\ K'\nu^4_{R(1,2)}}{[(K'+1)\ \nu^4_{P(1,2)} + K'\nu^4_{R(1,2)}]} \{\phi(K')_{T_a} n_a + \phi(K')_{T_w} n_{refl}\} \tag{2.19}$$

After measuring the relative spectral transmissivities of the two optical channels of the EBFP, the relative light levels S_1 and S_2 transmitted through the two channels can be expressed for a particular T_a, as:

$$S(T_a)_{\substack{1\\2}} = \sum_{K'=0,1,2..} \left\{ I^{P(0,1)}_{K'amb,refl} \times \tau^{P(0,1)}_{\substack{1\\2},K'} + I^{R(0,1)}_{K'amb,refl} \times \tau^{R(0,1)}_{\substack{1\\2},K'} \right.$$

$$\left. + I^{P(1,2)}_{K'amb,refl} \times \tau^{P(1,2)}_{\substack{1\\2},K'} + I^{R(1,2)}_{K'amb,refl} \times \tau^{R(1,2)}_{\substack{1\\2},K'} \right\} \tag{2.20}$$

where $\tau^{P(0,1)}_{i,K'}$ is the spectral response function of channel i at wave number $\nu_{P(0,1)}$ corresponding to an emission transition from level K'. (Spectral

response function calibrations are to be discussed in Sec. 4.3, and the relative spectral response functions for the EBFP-RTA flown on rocket AEF-II-118 are presented in Fig. 5.) The resulting relationship between intensity ratio (S_1/S_2) and the ambient temperature (T_a) can serve as a theoretical calibration curve for the EBFP-RTA. Such a curve for the AEF-II-118 payload is presented in Fig. 6. The figure also shows the effect of a 10° angle of attack (ψ = 80°) at typical flight speed ratios on the intensity ratio curve. It should be noted that the above analysis for the effect of reflected molecules on the RTA calibration curve is only applicable in the free molecular flow regime; for a 10 cm dimension instrument, such as the one on AEF-II-118, free molecular flow conditions occur about 110 km. Below 110 km altitude (temperature below 300K) the curve in Fig. 6 corresponding to Ω = 0 is applicable.

3. EBFP ELECTRON GUNS FOR ROCKET FLIGHT

In order to make the 'fast' accurate measurements that are required during a rocket flight, it is important to generate as much useful light as possible with the available beam power from the electron gun.

Weight and volume restrictions place an upper limit on the total beam power that can be provided. The current and voltage relationship in which the beam power is provided is governed by the following factors:

1. Gun perveance.
2. Gun efficiency.
3. Filament and accelerating power requirements.
4. Deflection of the beam by the earth's magnetic field.
5. Electrical (Paschen) breakdown inside the gun at high gas pressures (above 10 mtorr).
6. Scattering of the beam, the production of secondary electrons, and gas focussing of the beam.
7. Focussing of the electron beam to the observation region.
8. Fluorescence of the lens and backstop.
9. Flight volume and payload weight limitations.

The final selection of the gun operating conditions was made after carefully evaluating all the above items. A plausibility argument for the final choice may then be made after examining Figs. 7 and 8 in conjunction with the items mentioned previously. Figure 7 gives the gun input power and relative fluorescence yield for the (0,0) band of the First Negative System of the nitrogen molecular ion as a function of electron beam energy. The light yield curve was obtained by scaling the electron gun current according to the 3/2 power law and using the cross sections obtained by McConkey and Latimer (Ref. 8). Figure 8 shows calculated beam deflections due to the earth's magnetic field (see Sec. 3.4) as a function of electron beam energy for several distances from the electron gun.

It is pertinent to point out that current flight batteries have an energy density of approximately 200 joules/cm^3 and about 20,000 joule is required for a 6-minute flight with a 2500 volt gun operating at 10 mA. A DC-DC converter for these same conditions has a volume of approximately 500 cm^3 and a weight of 850 grams.

It is tempting to consider a high voltage, high perveance pulsed gun, enabling discrete measurements to be carried out at some distance from the vehicle whilst simultaneously keeping the energy requirements at a reasonable level. Background light could be rejected using such a scheme and in addition any accumulated charge on the vehicle can be given time to dissipate. The observation volume could be located many metres from the vehicle since gas scattering and deflection of the beam would be minimized. However, from Fig. 7 it can be seen that a 100 kV 2.5A gun will increase the light yield for the N_2^+ 1N (0,0) vibrational band by about a factor of 25 over a 2.5 kV gun operating at 10 mA, and thus the 100 kV, 2.5A gun would require a high duty cycle to yield light levels comparable to those obtained by a 2.5 kV, 10 mA DC gun. For equal signal levels, the 100 keV and 2.5 keV guns would then be operating at power levels of about 10 kW and 250 W, respectively. In addition, the high voltage gun can achieve long distance operation only at the expense of a loss in optical collection efficiency; the latter usually scaling inversely as the square of the distance from the rocket to the observation point.

3.1 Electron Gun Types

Traditionally, high voltage oxide cathode guns of the type used in televisions have been used for much of the low density gasdynamic investigations in wind tunnels. While these are well suited for this purpose, they are not the best choice for a rocket application. Table 1 lists some of the more important parameters for several types of electron guns. Although there is some overlap in the performance values associated with each gun, in general the following observations can be made.

TABLE 1

SOME CHARACTERISTICS OF ELECTRON GUNS

	WELDING TYPE	T.V. TYPE	MAGNETICALLY CONFINED ELECTRON BEAM
Nominal Voltage	1-100 kV	20 kV	See Eqn. 3.1 of text
$G = \frac{\text{Perveance}}{\frac{I_{beam}\ (\text{amps})}{V_{beam}^{3/2}\ (\text{volts})}}$	1×10^{-7}-3×10^{-6}	$\simeq 5\times10^{-11}$	$\simeq 25\times10^{-6}$ with appropriate $\vec{B}$ field
Beam Angle θ	12° - 30°	< 10°	< 10°
Diameter of Primary focus	0.5mm - > 5mm	< 2mm	Variable
Ruggedized	yes	no	Yes

Welding Electron Guns

These are usually compact, rugged, high perveance devices. With suitable electrode spacing and equipped with pure tungsten cathodes they may

be operated at high ambient pressures. In some cases it may be necessary to refocus the beam to provide a secondary focus at the optical observation region (a point remote from the rocket).

T.V. Type Electron Guns

The majority of T.V. guns are designed using oxide coated cathodes, although tungsten cathodes are available on special order. In general they are low perveance, electrostatically focussed devices, with an electrode structure that is accurately aligned and not inherently rugged.

Pressures greater than about 1 mtorr (typical in many low density wind tunnel applications) are required to provide sufficient light for accurate observations when using the low current (approximately 100μA) from a T.V. gun. At low density the optical signal is down at least two orders of magnitude when compared with that obtained from a 2.5 kV, 5 mA gun.

The high voltage (~ 20 kV) is advantageous at high pressures since less of the beam electrons are scattered out of the nominal beam diameter. A high energy beam is essential in many aerodynamic flow simulation studies where the electron beam is used to spatially define the observation region in the flow field.

Magnetically Confined Electron Guns

Very high perveance beams may be obtained using magnetic confinement of the electrons. Pierce (Ref. 9) gives the following equations for the maximum beam current I_{max} attainable with an acceleration potential V.

$$I_{max} = 25.4 \times 10^{-6} V^{3/2} \qquad (3.1)$$

The magnetic field B required to confine the electrons to a beam diameter 'a' is given by

$$B = \frac{5.5 \times 10^{-6}}{a} \sqrt{V} \qquad (3.2)$$

where 'a' is in metres, B in Wb/m^2 and V in volts. The main drawback with this type of gun is the obstruction to the flow field caused by the large magnets required to produce beam confinement. Field strengths of 0.1 Wb/m^2 or greater are necessary over the beam length when the beam energy exceeds 1 keV. Such large magnetic fields may also perturb peripheral equipment on a rocket payload.

3.2 Operating Pressure Range and High Voltage Breakdown for Electron Guns

Ideally the electron gun should operate over a wide range of pressures without arcing or deterioration. Vacuum arcing, or Paschen breakdown can be a serious problem over a pressure range that is determined by the operating voltage and the product of the pressure and the gun electrode spacing. Although relationships for the breakdown voltage, pressure and distance may be helpful, curing an arcing problem is largely an empirical art.

In general all high voltage supplies, and any batteries or regulators held at high voltage should be held at atmospheric pressure; this makes servicing

simpler. High voltage leads to the gun and the corresponding feedthroughs should be vacuum encapsulated.

3.3 Cathodes for Electron Guns

The gun cathode should be rugged and capable of operating at pressures up to about 50 mtorr. The heating power should be low since this power will cause outgassing from the gun surfaces which may arrive at the observation region.

Oxide Coated Cathodes

Oxide coated cathodes deteriorate when the pressure rises beyond about 10^{-5} torr (air); this means that pumping would be required in flight below 120 km if the deleterious effects of cathode poisoning and subsequent loss of emission are to be avoided. Under similar operational conditions oxide coated cathodes require considerably less heating power than all other materials. For example, a 2500 V, 10 mA gun requires about 5 W of cathode heater power using an oxide coated cathode, and about 25 W for its tungsten counterpart. The reader is referred to Spangenberg (Ref. 10, p. 23 et seq.) for a good description of cathode characteristics.

Pure Tungsten Cathodes

The physical and electronic properties of tungsten are well known and documented. Its workable properties are less than desirable, but it is a rugged stable material and its low electron emission efficiency, shown in Fig. 9, is offset by its ability to provide electron emission at high pressures (greater than 10 torr in air). Although prolonged operation at these high pressures will result in oxidation and eventual destruction of a tungsten cathode, it is operating in a region where almost all other cathode materials would have effectively ceased to function.

Some Other Cathode Materials

Perhaps because Ba Sr O has been used for T.V. gun cathodes, this material is used in most other electron guns. MacNair (Ref. 11, p. 470) has suggested that in oxidizing gases Ba Zr O_3 is a useful cathode material.

Thoriated tungsten is also a more efficient electron emitter than pure tungsten; however, it too can be poisoned at high air pressures drastically reducing its electron emission.

Tantalum has a lower melting point than tungsten but is easier to work and gives 10 times the emission of tungsten at temperatures less than 2500 K.

3.4 Selection of the Flight Electron Gun

Several types of guns were investigated before choosing the version used in the latest series of flight experiments. Spangenberg (Ref. 10) gives details and curves which enable a Pierce type gun to be designed for a range of perveances and beam angles (beam angle θ is defined in Fig. 10). Following the Spangenberg procedure, a gun was designed and constructed to operate at 5 kV and 10 mA. Performance was satisfactory using a properly shaped molybdenum cathode heated to electron emission temperature by electron bombardment.

However, operation in this manner was considered undesirable because of the high thermal inertia involved. Attempts to use ribbon or wire cathodes resulted in unacceptably low gun efficiency and it was concluded that guns with this type of geometry do not operate satisfactorily unless the cathode is a continuous equipotential surface.

The electron gun used in all the UTIAS flights to date is a modified welding gun type MC2-01003 manufactured by Energy Beams Inc., Haskell, N.J. This gun, depicted in Fig. 10, operates with a space charge limited perveance of 0.1×10^{-6}; it is of modified Pierce geometry enabling it to be operated with 0.25 mm dia. tungsten filament cathodes. The primary beam focus is a spot about 0.5 mm in diameter approximately 6 mm from the external anode surface and the total beam angle is 6.5 degrees.

The gun functions at 80% efficiency over the pressure range below 10^{-7} to 10^{-2} torr (in air at 300 K temperature) and will operate without arcing at pressures below 1 torr. On flight VB-32 the gun was flown in an unevacuated state and performed satisfactorily. The densities encountered during flight were between 5×10^{-2} and 5×10^{-6} equiv. torr.

All metal portions of the gun are machined from non-magnetic stainless steel; mica is used to insulate the filament supports and fired lava is employed for positioning the beam forming or cathode electrode. (The spacing of this electrode with respect to the anode plate is critical as is the cathode location.) Tungsten, 0.25 mm diameter wire is used for the cathodes which are wound at room temperature. With the short supporting wires these cathodes are extremely rugged and the assembled gun can easily withstand the necessary vibration tests for rocket flights.*

Several of these guns have been operated over long periods (7 hours continuously at 2-5 kV and 7 mA) in laboratory studies. When combined with a suitable emission controller, they are a valuable adjunct to the low density diagnostic equipment inventory.

The addition of magnetic deflection coils with their axes near the plane of the cathode allows the gun to be operated in a pulsed mode permitting the optical fluorescence signal to be synchronously detected.

3.5 Focussing the Electron Beam

In many welding type guns the primary focus is close to the gun structure and refocussing of the electrons is desirable in order to maintain a reasonable beam cross-section at the observation region. Electrostatic or magnetic lenses may be used and an excellent account of both types may be found in Ref. 12.

Electrostatic Lenses

Electrostatic lenses (Fig. 11a) are simple to construct and have low power consumption; an einzel type should preferably be used for refocussing the beam. This ensures that the potential before and after the lens is the same.

*Vibration specifications: 15 g peak, 20 to 2000 Hz. One 40 second frequency sweep in each of the 3 major axes.

Whilst electrostatic lenses are attractive by virtue of their simplicity, they expose large surface areas at high potential to the ambient atmosphere. Paschen breakdown is therefore likely at low altitudes with this type of lens and for this reason they have been avoided in the present study.

Magnetic Lenses

Permanent magnets may be used to focus an electron beam. The annular magnets should be energized in the orientation shown in Fig. 11b.

A solenoidal coil lens, depicted in Fig. 11c, is more efficient if magnetic shielding is employed to confine the flux leakage to a narrow circular region perpendicular to the coil axis. Confining the flux also helps to define the principal plane of the lens for calculation purposes. Using the notation of Fig. 11c, the conjugates and image sizes may be calculated using the simple lens equation

$$\frac{1}{u} + \frac{1}{v} = \frac{1}{f} \tag{3.3}$$

where u and v are the distances from the lens plane to the primary beam focus point in front of the gun anode plate, and to the desired observation point, respectively. The quantity f is the effective focal length of the lens and it can be obtained from Ref. 12:

$$f = \frac{Gv}{(NI)^2} \tag{3.4}$$

where G is known as the coil-form factor and has a value $G \approx 98\ R$ when the coil is operated in air, R being the effective coil radius. The product NI is the number of ampere turns and V is the gun acceleration potential in volts. Klemperer (Ref. 12) quotes a practical upper limit for coil current of 2.3 amp/mm^2 when the lens is air cooled.

For the VB-39 apparatus (to be discussed in Sec. 5.2), u and v were 3.18 cm and 10.8 cm, respectively. The coil was composed of 1100 turns of No. 30 AWG magnet wire (24.3 Ω) and was operated at 220 mA to give a current density of 1.85 amp/mm^2 and a calculated effective focal length of 41.8 mm for a 2.5 kV electron beam and R = 1 cm. The actual focal length under these conditions was about 25 mm and the increased efficiency was due to magnetic shielding.

The Seidel aberrations are present in an uncorrected magnetic lens; however, from a practical standpoint they do not present a serious impediment. The focussed beam is well defined and of adequate cross-section (1-2 mm dia) at the focal region for the type of measurement optics to be described later.

Deflection of the Electron Beam

In most cases viewing of the beam in the observation region is accomplished by an optical system which views a finite portion of the beam fluorescence. Wandering of the beam can therefore introduce serious complications in analysis. In laboratory experiments it has been observed that electron beams of less than 10 keV energy are easily perturbed when operating in close

proximity to large masses or iron or steel due to the residual magnetism of these items. In a rocket experiment care must be taken to project the electron beam into a region free from stray magnetic fields, and a similar philosophy must also be adopted during calibration of the EBFP. During the flight the beam will be perturbed by the earth's magnetic field; on many payloads there is some spin associated with the vehicle resulting in subsequent periodic movements of the beam in the observation region.

The deflection of the beam as a function of the accelerating voltage by the component of the earth's magnetic field perpendicular to the beam is shown in Fig. 8. It should be noted that if the beam is aligned with the earth's field then this effect disappears. Fort Churchill is a poor location for minimizing this effect, having a magnetic declination of 83.5°.

In the situation where a low energy beam is projected some distance from the rocket, a partial compensation of the beam shift may be made using electrostatic deflection plates to change the beam's direction before it reaches the observation region; this technique was employed in the apparatus flown on rocket AEF-II-118. The following relationship may be used for correcting a beam displacement D at a distance L from a pair of parallel plates of length ℓ and separation d. The accelerating potential is assumed to be V and a potential V' is maintained between the places

$$D = \frac{\ell L}{2d} V'/V \qquad (3.5)$$

3.6 Location of the Observation Region

The EBFP enables gas to be sampled at some distance from the payload without the introduction of 'material' probes in the observation region. How representative of the ambient atmosphere the sampled gas is, depends on several factors. For example, the vehicle motion, outgassing from the rocket payload, as well as reflection of ambient gas particles from payload surfaces may affect the measurements in the observation region. Thus, in order to facilitate the interpretation of the flight results it is desirable to minimize such effects.

Below altitudes of about 80 km the EBFP, with a characteristic dimension of approximately 10 cm, is in the continuum flow regime with a Knudsen number of the order of 0.05. Consequently, on a vehicle travelling at supersonic speeds, the EBFP observation region, if chosen to be too close to the payload, may be disturbed by the bow shock wave formed in front of the apparatus. This is shown in Fig. 12 which is a flow field visualization on a 1/14th scale model of the EBFP apparatus flown on AEF-II-118 (Fig. 13). The photograph indicates the density variation in the flow which simulates atmospheric densities corresponding to 90 km altitude and a flow Mach number of M = 5. The location of the observation volume for the flight was chosen to exclude the regions disturbed by the presence of the shock wave.

If the electron gun can be mounted in the tip of the rocket, firing forward as shown in Fig. 14, it is possible to prepare the apparatus in such a way as to produce an attached shock wave. As a result, minimal perturbations of ambient atmospheric conditions would occur at the observation region ahead of the apparatus. However, it should be mentioned that this operating configuration introduces other complications. First, the observation region will

be in an unfavourable location for measuring during the down-leg portion of the flight, unless the payload is turned to point towards the earth. Secondly, a backstop cannot be employed to either collect the beam or for optical background light rejection.

At high altitudes, where the mean free path of the ambient gas is many times the apparatus dimension, the flow is free molecular. Under such flow conditions, it is possible for molecules originating from outgassing of the vehicle or components to reach the observation volume. In addition, ambient gas molecules that have first struck portions of the payload may be reflected into the observation region. Corrections may be made for reflected ambient gas molecules, if certain assumptions are made concerning the accommodation coefficient of the reflecting surfaces. Goldberg (Ref. 13) examined this problem for the tip mounted gun and Fig. 14 shows the reflected number density for two angles of attack at speed ratio of unity. The effect of reflected molecules for the AEF-II-118 EBFP apparatus has been treated in Sec. 2.3.

3.7 Electron Beam Collector and Optical Backstop

Rocketborne electron beam studies up to the present time have employed an electron beam collector to avoid excessive charge buildup on the vehicle. In the case of the UTIAS probes, the beam collector serves a dual purpose by providing an optically black background for the viewing optics.

If a direct return path for the electrons to the power supply, such as a backstop, is not provided, the rocket will acquire a net positive charge. Using the analysis of Beard and Johnson (Ref. 14) and assuming charge condensation occurs on a spherical vehicle of 0.25 metre radius (a conservative value for a separated payload), the rocket potential will then be less than 150 V at 110 km and less than 1600 V at 75 km for a 10 mA 2.5 kV DC beam. It is important to note that even with an electron collector enough electrons miss the backstop due to scattering at low altitude to produce a charge buildup which seriously perturbs potential and charge measuring experiments on the same payload. On the UTIAS flight VB-28, the backstop did not deploy and the beam was discharged with no collection other than that provided by return conduction due to the plasma properties of the ambient atmosphere. The excessively high light yield on this flight has been tentatively ascribed to optical excitation caused by secondary electrons spiraling back to the rocket along the magnetic lens field lines.

For appropriately chosen spectral features, the optical fluorescence signal is proportional to the beam current passing through the observation region. However, because of electron scattering at high gas densities, there may be a considerable difference between the current leaving the gun and that collected by the backstop. Thus the actual current passing through the observation region may not be known. A laboratory calibration with gases of known density must be used in order to validate the EBFP as a density gauge. The variation of collected beam current as a function of altitude for flight AEF-II-118 is shown in Fig. 3.

If the electron beam is modulated, it is possible to measure the beam current anywhere along its length using a current type transformer probe. The location of this device is chosen to introduce minimum aerodynamic disturbance and is usually placed at the gun exit orifice. A comparison of the two

beam current measuring techniques over a range of pressures for the apparatus flown on VB-39 is presented in Fig. 15. It is evident that at higher pressures the beam current collected at the backstop is less than that measured at the gun exit orifice.

Optical Properties of Backstops

In principle, the combination of the stop S and the backstop B shown in Fig. 16a provides for complete rejection of background light from the optical detector. In practice, surface imperfections of the lens, as at P, may scatter light into the detector; similarly, some light may be reflected or scattered from the backstop into the system.

A compact low reflectance backstop may be made from a stack of razor blades, as shown in Fig. 16b. The reflectance varies with the direction of illumination changing from about 10^{-2} to 2×10^{-3} for light parallel and perpendicular to the grooves, respectively, when directed at 45° to the backstop plane normal. The optical trapping principle is shown in Fig. 16c; light entering the wedge should be specularly reflected and it is important that all surfaces be dust free.

A superior optical trap is shown in Fig. 16d. The edge of each wedge is a razor blade and the wedge interiors are coated with Apiezon black wax which has an extremely low diffuse reflection coefficient. This method produces a background at least two orders of magnitude blacker than the razor blades; however, it cannot receive the beam directly and the operating temperature is restricted to below 120°C. Neither point is a serious restriction on a rocket flight.

4. OPTICAL DETECTION SYSTEM FOR EBFP

In order to spectrally analyze the electron beam induced fluorescence of the EBFP two methods of light transport were employed. On flight AEF-II-118 the radiation originating from the observation volume was collected by the direct viewing method depicted in Fig. 17a. For the other flights, namely VB-28, VB-32 and VB-39, the collected radiation was transported by optical fibres as shown in Fig. 17b.

For the direct viewing method of AEF-II-118, the apparatus was so arranged that the electrons travelled from the gun through a light-tight metal tube and exited via an axial hole in the first lens, L_1 (refer to Fig. 17a), the latter having an aperture of f/2.3. Light was collected from about 1 cm of beam length located at about 15 cm from the lens and then directed by a mirror and lens L_2 through the stop S to the photomultiplier tubes after being collimated and passed through two narrow band interference filters. Light from a small 6V tungsten lamp was reflected into the main optical path using a thin clear glass splitter allowing the photomultiplier tube sensitivities to be checked during laboratory calibrations and flight operation.

Although providing the distinct advantage that each channel views the same optical volume, the direct viewing method becomes cumbersome when a large number of spectral channels are required. Greater flexibility in providing light for each optical channel and in locating portions of the apparatus in the payload is possible by using optical fibres for light transport as shown in

Fig. 17b. The light may also be shared unequally by choosing fibre bundles of varying widths but the dimensions should be large enough to allow for beam wandering. Since interstices between the fibres represent zero transmission, it is important to select fibres with the smallest diameter so that movements of the beam image may be adequately resolved. Each fibre bundle is transformed from rectangular to circular cross section to provide optimum optical coupling to the collimator which precedes the interference filter.

4.1 Interference Filters and Fibre Optics

The bandwidth of an optical interference filter at half the peak transmission is given by the following approximation:

$$\Delta\lambda \simeq \frac{\lambda_o \alpha^2}{2n^2} \qquad (4.1)$$

where α is the angle of incidence in radians, n the effective refractive index of the filter and λ_o the peak wavelength at normal incidence.

It is especially important if one wishes to preserve the normal incidence spectral characteristics of a filter, to ensure that all light passing through the filter does so at a low divergence angle. The fibre optic must have a numerical aperture large enough to collect the light from the beam efficiently; this light will then leave the bundle with an angular spread (about 45° for the optic used in the experiments described in this report). Passing light directly from a fibre optic through an interference filter can easily triple the bandwidth of a 10Å filter.

Spectral broadening can be reduced using the arrangement shown in Fig. 18a, the fibres being placed in the focal plane of the lens. An even better method entails optically coupling the lens to the fibre optic as shown in Fig. 18b. For f/1 coupling this results in a light gain of about a factor of 2.5 over the previous method for the same incidence angles on the filter. The lenses are easily fabricated from plexiglass and when properly aligned produce less than 1Å of broadening on a 10Å filter.

Additional protection against spectral broadening of the filter transmission function may be acquired by constructing the filters with high refractive index materials.

The optical fibres used in the flights to date were of low divergence with 75 μm diameter. They were supplied by Dyonics Ltd. A spectral transmission curve for the Dyonics fibres is shown in Fig. 19 along with the characteristics for a relatively new U.V. transmitting fibre.

4.2 Photomultiplier Tubes

For the experiment flown on Black Brant Rocket AEF-II-118, EMR 541D-01-14 photomultipliers were used. These tubes had a dark current of about 10^{-11} amps at a gain of 10^6 and a quantum efficiency of about 4% at 4000Å. These tubes functioned satisfactorily in all aspects but time response, showing a small hysteresis signal for several seconds after the light had been removed from the cathode.

EMI 9781A photomultipliers are currently used; with treatment as described in Ref. 15 these tubes have a comparable or lower dark current than the EMR tubes and a quantum efficiency of about 20% at 4000Å. Although these tubes are not ruggedized, they are less than one-tenth the cost of the EMR tubes and when immersed in a 5 mm envelope of RTV 615 compound conform to all the usual vibration specifications.

4.3 Spectral Response Function Calibration for EBFP

The spectral response function of an EBFP optical channel is required in cases where gas samples of the desired composition and temperature cannot be introduced into the probe region, when employing the calibration procedure described in Section 5.

Although an exact knowledge of the spectral properties of all channels is not mandatory, this information can be helpful and the spectral characteristics of all parts of an EBFP system are routinely measured. A method has been developed which allows both the relative and absolute spectral sensitivities of all EBFP channels to be determined and a step-by-step description of the procedure is given below.

1. A diffuse reflector* of appropriate size is placed in the probe region as shown in Fig. 20a and illuminated with narrow band radiation of a variable wavelength obtained from a tungsten source passed through a monochromator. The illuminated portion of the diffuser should correspond to that area usually occupied by the electron beam fluorescence in the probe region. The monochromator should be adjusted to provide a wavelength interval $\Delta\lambda$ which is one-tenth (or less) of the 'half intensity band width' of the transmission function under study (Fig. 20b) to ensure accurate measurements. The relative spectral response function $\tau_{i,\lambda}$ is defined as the product of the transmittance $T_{i\lambda}$ of all optical elements in the i^{th} EBFP channel and the corresponding photodetector sensitivity $D_{i\lambda}$ at a wavelength λ. The radiation collected by the EBFP lens L_1 in Fig. 20a will produce a signal $S_{i\lambda}$ in the i^{th} channel photodetector after passing through all the optical elements in that channel, that is:

$$S_{i\lambda} = \tau_{i\lambda} E_{\lambda} \qquad (4.2)$$

   where E_λ is the spectral radiance of the radiation originating from the white surface at wavelength λ. Wavelength scanning enables complete $S_i\lambda$ curves to be obtained (care should be taken to apply appropriate corrections if the monochromator bandwidth $\Delta\lambda$ or the gain of the amplifier used to measure the photo current is changed for different channels). The relative spectral response functions $\tau_{i\lambda}$ may then be obtained from Eq. 4.2 by two alternative ways as described in (2) and (3) below.

2. A photodetector whose relative quantum efficiency, $Q\lambda$, as a function of wavelength is known, is placed at the location of the lens L_1 in Fig. 20a.

---

*Eastman white reflectance standard, Eastman Kodak Co., Rochester, N.Y. This material has 100% reflectance to +0% - 3% over the region 2500Å-8000Å.

The radiation E_λ falling on this detector will give rise to a detector signal R_λ given by

$$R_\lambda = k\, E_\lambda\, Q_\lambda \tag{4.3}$$

(k is a normalising constant allowing for the detector gain and the solid angle of the radiation collected from the diffuse reflector). The relative spectral response functions $\tau_{i\lambda}$ may now be derived from Eqs. 4.2 and 4.3 since Q_λ is known and R_λ and $S_{i\lambda}$ are measured signal quantities. If in addition the absolute sensitivity of the standard photodetector is known then the constant k in Eq. 4.3 may be evaluated and the absolute values for the spectral response functions also deduced.

3. Alternatively, the following procedure for the determination of the relative spectral response functions may be employed. Narrow band filters of 10Å to 50Å half-width are usually used with the EBFP and although there may be quite large variations in the function E_λ from filter to filter, the energy function is relatively constant over each individual filter bandwidth. If the assumption is made that E_λ does not vary over a filter bandwidth then for each channel i, $E_{\lambda i}$ can be substituted by a constant C_i. Thus Eq. 4.2 can be rewritten as

$$\tau_{i\lambda} = \frac{S_{i\lambda}}{C_i} \tag{4.4}$$

In order to determine the $\tau_{i\lambda}$, once $S_{i\lambda}$ have been measured as described in (1), it only remains to evaluate the constants C_i. A standard lamp of known relative spectral energy distribution H_λ is positioned as shown in Fig. 20c to illuminate the diffuse reflector situated in the probe region. The lens L_1 then passes the reflected radiation simultaneously to all EBFP optical channels. The measured relative detector output ρ_m^i of the i^{th} channel will then be given by

$$\rho_m^i = \frac{1}{C_i} \int_\lambda S_{i\lambda}\, H_\lambda\, d\lambda \tag{4.5}$$

Thus, by numerically evaluating the integral in Eq. 4.5 the constants C_i can be obtained which allows $\tau_{i\lambda}$ to be determined by Eq. 4.4.

4. If the spectral response functions $\tau_{i\lambda}$ have been obtained using the method outlined in (2) then the standard lamp procedure just described can serve as a consistency check between the channels. For this test the calculated relative response of each channel when illuminated as shown in Fig. 20c are obtained from the following equation

$$\rho_c^i = \int_\lambda \tau_{i\lambda}\, H_\lambda\, d\lambda \tag{4.6}$$

Equation 4.7 should hold for all values of i if C_i can be assumed to be constant over the bandwidth of channel i.

$$\frac{\rho_c^i}{\rho_m^i} = \frac{\rho_c^{i+1}}{\rho_m^{i+1}} \simeq \text{constant} \tag{4.7}$$

Absolute values for the spectral response functions may also be assigned if the absolute spectral radiance of the standard lamp and the geometrical optical constants are known.

4.4 Optical Signal Characteristics

Optical Signal Levels

The photomultiplier anode current, S, due to the fluorescence radiation is given by

$$S = 1.6 \times 10^{-19}\ \eta\ \frac{G\Omega}{4\pi} \int_{\lambda_1}^{\lambda_2} \tau(\lambda)\ E(\lambda)\ d\lambda \ \text{(amps)} \qquad (4.8)$$

where

η = photomultiplier quantum efficiency

G = photomultiplier gain

Ω = optics solid angle

$\tau(\lambda)$ = combined transmittance of all optical elements

$E(\lambda)$ = fluorescence flux (photons/s emitted from the focal region into 4π steradians)

The quantity $E(\lambda)$ is a function of the gas species present and also a function of the particle density and the electron beam current passing through the observation volume. Figure 21 shows the magnitude of the signals which may be expected using a 5 mA 2500 eV DC beam where the optical fibre method of light transport is employed.

Signal Statistics

Statistical fluctuations of the anode count rate (N/s) place a limit on the measurement precision of the photomultiplier signal. With all other factors (i.e., beam current, optics, etc.) fixed, the precision can be improved only by increasing the observation time.

If a DC beam is observed for a period of time, resulting in an anode count N, then the value $1/\sqrt{N}$ gives the statistical accuracy for that observation. For the nitrogen channel, shown in Fig. 21, a 1% measurement can be made at all altitudes lower than 120 km in a 10 ms interval; this corresponds to an altitude differential of about 20 metres for a vehicle moving at 2 km/s.

In the situation where an equal interval modulated electron beam produces a signal of S counts/s which combines with a background input of D counts/s, then an integration time 't' is required to produce a precision 'a' in the measurement.

$$t = \left(\frac{\sqrt{D + S} + \sqrt{D}}{aS} \right)^2 \qquad (4.9)$$

Using Eq. 4.9, t has been calculated as a function of altitude for the same parameters detailed in Fig. 21 where a dark count of D = 500 s^{-1} has been assumed; the results are presented in Fig. 22.

4.5 Background Light and Its Rejection

A small fraction of the electrons striking the backstop will be reflected somewhat specularly at or near the primary beam energy; these may strike the optical lens and other structures in the field of view causing fluorescence. This spurious optical radiation cannot be rejected by synchronous detection and will set a lower limit for reliable operation of the EBFP. Vacuum oils and greases fluoresce very well under electron bombardment as does pyrex and the optical glasses. It has been found experimentally that at least for 2.5 keV electrons, quartz (GE 101) and plexiglass have a low fluorescence yield and both have been used for fabricating the first collection lens.

In addition, stray light may enter the optical system from aurora, moonlight, or even from Rayleigh scattered sunlight if the solar depression is inadequate. In a detection system employing phase sensitive detection, light from sources other than the beam may be partially rejected but the time required to reach a certain measurement precision given by Eq. 4.9 may be inordinately long. It is therefore highly desirable to provide as much attenuation to background light as possible by careful optical design.

With the optical design of the direct viewing method (AEF-II-118) shown in Fig. 17a the stop S provides good attenuation for all light not on axis; the angular dependence of the rejection is shown in Fig. 23a. Calculations show that the instrument can tolerate ~ 1 kr at 10° from the optic axis, resulting in a 10% error in a nitrogen density measurement at 150 km. The center of the lens L_1 in Fig. 17a is essentially opaque; this serves two useful purposes. First, the length of the beam viewed by this lens is confined to a region midway between the lens and the backstop, thus occluding from view the disturbed regions at lower altitudes. Figure 23b shows the light collection efficiency along the optical axis. Secondly, light from the gun filament which illuminated only a small central portion of the backstop was prevented from entering the optical system since paraxial rays could not pass through the lens-stop combination.

Although the fibre optic method has advantages in compactness and flexibility, it is more difficult to reject background radiation with this arrangement. If the maximum amount of light from the beam is to be utilized, then the equivalent stop S of Fig. 17a must be so large as to make its use of questionable value. The fibre optic detection system employs lens hoods and a large stop shown in Fib. 17b. The hoods are kept as short as possible to minimize aerodynamic disturbances. The angular rejection of stray light for the fibre optic system is shown in Fig. 24 and shows a better rate of attenuation than the direct viewing arrangement (the latter could be improved significantly with the addition of lens hoods). The calculated background tolerance for a 10% error in the nitrogen density measurement at 150 km is 2.5 kr at 30° from the optic axis.

5. ROCKET EXPERIMENTS AND FLIGHT RESULTS

5.1 Initial Flight of EBFP: Black Brant Rocket AEF-II-118

A Black Brant II rocket, AEF-II-118 launched on 28 January, 1969, from Fort Churchill, Manitoba, carried the first version of the EBFP. A complete rocket payload was available for the experiment permitting procedures that would not ordinarily be possible when flying as a passenger experiment. The flight package is shown in Fig. 13 using the direct viewing optical configuration of Fig. 17a. The primary purpose of the instrument was to demonstrate the application of the EBFP for upper atmospheric diagnostics. The apparatus, previously referred to as a Rotational Temperature Apparatus (RTA) in Refs. 1 and 2, used two narrow band optical channels located in the N_2^+ first negative system (0,1) vibrational band in order to obtain rotational temperature measurements.

Vacuum Procedures for AEF-II-118

Vehicle and component outgassing continues to bother many rocket launched experiments and an attempt was made to alleviate this problem using the procedures outlined below:

(a) The whole nose cone section of the payload was vacuum sealed,* providing a pressure of 10^{-5} torr during all testing phases prior to flight. Figure 25 shows the portable vacuum system attached to the payload. With pumping discontinued the pressure rose to 300 m torr in 24 hours. At launch, the cone pressure was below 100 m torr.

(b) All pyrotechnics were either qualified as gas containing or separately confined in O-ring sealed compartments.

(c) All portions of the payload at atmospheric pressure were sealed to prevent gas leakage in flight.

(d) The payload section was separated from the spent motor with a relative separation velocity of 1.2 m/s.

Backstops, Dynamic Balance and Cone Deployment (AEF-II-118)

A razor blade backstop was employed on AEF-II-118 and symmetrical mass distribution was achieved using a dummy arm. The total payload was then dynamically balanced to 0.7 kg-cm at 3 rps, to minimize attitude changes after payload separation.

The deployment of the clamshells at a spin rate of 3 rps posed some difficulties. There is a tendency for the cone halves to shear as they are separated (Fig. 27a). This shearing is brought about by the cone halves rotating more slowly with respect to the payload as they move outwards conserving their angular momentum. Clean deployment was finally achieved using

*The technique for sealing the cone is shown in Fig. 26. The problem of intersecting seal paths was solved with the aid of a metal spacer and a small viton rubber insert, providing a seal for the upper and lower portions of the spacer and also sealing against the two O-rings contained in each half-cone section.

mechanical restraints as shown in Fig. 27b; the lower guides prevented slippage of the clamshells around the payload base, whilst the fingers located on the cones acting on the instrument section ensured that the clamshells were clear of all internal structure before shearing action could take place.

Deflection of the Beam at Fort Churchill

An experimental check on the influence of the earth's magnetic field was carried out at the Churchill Research Range (C.R.R.) A tube of sufficient length and diameter to permit optical observation of the beam was attached to the nose cone and the gun was operated at a pressure of about 20 mtorr in air. The optical signal was unchanged when the payload was tilted to $\pm$ 45° in all azimuths about the vertical; this confirmed the prediction from laboratory tests.

Calibration Lamp

A carefully regulated CM 2181 6V tungsten filament lamp run at about 1750 K temperature was used to measure changes in the photomultiplier sensitivities during calibration, before launch and during the flight.

Spectral Calibration of the EBFP-RTA

In order to bypass the interference filter problems mentioned earlier in this report it was decided than an in situ calibration of spectral sensitivity functions for the complete instrument would be carried out. The optical arrangement for this procedure is outlined in Fig. 28a. An Eastman white reflectance standard, having properties approaching an ideal Lambertian diffuser was placed at the focal point of the EBFP lens L_1 (refer to Fig. 17a). Monochromatic radiation of known intensity was then imaged onto this surface and the relative spectral response functions of the EBFP could be determined from the photomultiplier outputs (refer to Sec. 4.3).

The spectral response functions given in Fig. 28b were identical for all spot sizes of light reflected from the Eastman white surface, including that which filled the defining aperture shown in Fig. 17a. This ensured that wandering of the beam would not result in calibration changes. Figures 28b and 28c also show the light intensity distribution in the rotational lines of the N_2^+ 1N (0,1) band at 293 and 77 K, respectively.

Gas Temperature Calibration of EBFP-RTA

Ideally a gas calibration of the EBFP in the laboratory should provide for duplication of the conditions encountered in flight. These would include simulation of composition, density, temperature and directed velocity of the gas for the entire altitude range. These requirements, superficially simple, are actually quite formidable and only a static check on various gases at different densities and temperatures was attempted. Static calibrations should suffice if the characteristic radiations chosen for EBFP diagnostics are optically allowed emissions resulting from direct excitation-emission transitions; hence the measured quantities should be velocity independent. The N_2^+ First Negative system used for the AEF II-118 apparatus satisfied these requirements.

Using the apparatus shown in Fig. 29, an attempt was made to obtain a curve for the variation of the ratio of photomultiplier signals in the two channels with temperature using the two-channel photometric scheme described in Sec. 2. The source heater/cooler supplied gas at temperatures in the 77 K to 750 K range to the observation region of the EBFP-RTA. The experimental signal ratios obtained using this method are shown in Fig. 30 together with the theoretical curve calculated in Sec. 2.3 for $\Omega = 0$ using the instrumental spectral sensitivities and the theoretical spectral intensity distribution for the N_2^+ 1N (0,1) vibrational band.

It should be pointed out that at the higher temperatures outgassing contaminates the source gas and raises the pump load making cleanup more difficult. In view of these problems and the uncertainties in ascertaining the true temperature of the source gas, the theoretically predicted curve (Fig. 6) was used for the reduction of the flight results.

Ratio Measurement Using Logarithmic Amplifiers

In flight the ratio of the two signals (I_{4254}/I_{4271}) is conveniently handled electronically by taking the difference of the logarithms of both signal outputs as shown in Fig. 17a; the final output is then the log of the desired ratio.

Flight Results with the Rotational Temperature Apparatus (EBFP-RTA)

The flight temperature data for AEF II-118 have been reduced and are compared with the CIRA 1972 model atmosphere in Fig. 31. On the upleg, with the fore portion of the RTA directed into the wind, the measured temperature shows good agreement with the reference atmosphere. However, on the downleg there is a sharp increase in the RTA temperature, commencing at approximately 110 km where transition flow conditions occur. These results point out the importance of locating the probe region in a position free from aerodynamic interference. The spurious downleg temperature measurements are the result of shock disturbance from the lower portion of the instrument package. The vehicle orientation, although important in the free molecular region as far as reflected molecules are concerned, becomes critical at higher densities where the probe may be sampling a shock contaminated region.

Although the RTA was designed primarily as a temperature sensor, by comparing the absolute photomultiplier flight signals with those obtained under laboratory conditions, it is possible to derive density information. The narrow band filters did not include all the rotational line emissions from the N_2^+ 1N band and an adjustment is necessary which corrects the measured density for temperature variation; this adjustment has been applied and the derived density results are given in Fig. 32.

Two hot cathode Bayard Alpert type ion gauges were included in the payload enabling atmospheric density to be obtained using a modulation method described by Grenda in Ref. 16. For comparison purposes these density results are also included in Fig. 32.

5.2 Black Brant Rockets VB-32, VB-28, VB-39 Employing the Multi-Spectral Channel Fibre Optic System

Two compact versions of the EBFP have been flown as passenger experiments; they are shown in Figs. 33-35. Up to 4 real time synchronously detected

channels or 5 DC time shared channels are available for spectral filters.

Black Brant VB-32: Experiment and Flight Data

This vehicle was launched on March 3, 1971 into an intense aurora (> 50 kr), all parts of the experiment functioned well, yielding good data. The electron gun on this package was flown in an unevacuated condition being vented only through the gun exit orifice. The functional operation of the gun was checked prior to flight by subjecting the entire apparatus to a conservative flight pressure profile.

Typical telemetry signal traces obtained with 5 DC time shared channels are shown in Fig. 36; the sequencing time was chosen to allow for just over one rocket spin cycle in each filter observation period.

Molecular nitrogen concentrations measured during flight VB-32 are presented in Fig. 37. Auroral light from the OI 5577Å forbidden transition affected the molecular oxygen channel signal and these data have been omitted. The O_2 concentration measuring channel was located in the (1,0) band sequence of the O_2^+ 1N system located at about 5590Å; the filter half intensity bandwidth was about 70Å.

Time did not permit a test of the stray light rejection characteristics of this instrument. They are, however, significantly inferior to the newer fibre optic systems employing lens hoods.

Black Brant VB-28: Experiment and Flight Data

For this experiment two EBFP units, each employing 5 DC time-shared channels, were placed in a back-to-back configuration as shown in Fig. 34. The gun and the upper optics units were placed in the topmost portion of the payload and optically coupled with 1.8 m of fibre optics. Launching took place at 0943 GMT on March 24, 1972 from Fort Churchill.

The channels were selected in such a way as to enable molecular nitrogen, molecular oxygen and atomic oxygen concentrations to be measured. For N_2 concentration the N_2^+ 1N (0,1) vibrational band was selected. Two channels were allocated to O_2: the (1,0) and (2,0) band sequences of the O_2^+ 1N system. The atomic oxygen channel was located at 4416Å to collect light from the OII 4415 and 4417Å spectral lines. A detailed description of the spectral response function calibration and static gas calibration as well as the reduction of flight results for the VB-28 EBFP is given in Ref. 5.

To alleviate outgassing problems the EBFP was launched with the gun in an evacuated state. The vacuum arrangement can be seen from Fig. 17b. Buna N O-rings were used since these have a very low permeability for air (6 atm cm^3/year per linear metre of seal). Opening the gun in flight was accomplished with a bellows actuated O-ring sealed cover. Final evacuation of the guns was carried out at C.R.R. with the internal pressure at launch being below 200 mtorr air.

During clamshell ejection the backstops were damaged and did not deploy completely. This resulted in light leakage into the optical system. Signal leakage from the moon can be seen quite clearly on the sample telemetry record shown in Fig. 36b, appearing cyclically at the rocket roll rate.

The VB-28 flight results for N_2 and O_2 concentrations presented in Fig. 37 have been normalized to the nitrogen concentrations obtained during flight VB-32 over the 110-120 km range (a region where beam losses due to scattering are acceptably small); this was necessary since the beam current could not be determined without the backstops.

Channels were also allocated to the 4416Å OII line for atomic oxygen concentration measurements but light leakage from the moon prevented an accurate reduction of these data.

Black Brant VB-39: Experiment and Flight Data

Black Brant VB-39 was launched from C.R.R. at 0253 GMT on February 28, 1974, carrying an EBFP as part of the 14 experiment payload complement. The EBFP incorporated four real time synchronously detected optical channels using a fibre optic arrangement; the instrumentation is shown in Fig. 35. The four channels were allocated to obtain N_2, O_2 and O_1 concentrations as well as vibrational temperature measurements. For N_2, O_2 and O_1 concentrations the filters were located in the N_2^+ 1N (0,1) band, the (1,0) band sequence of the O_2^+ 1N system, and the OII 4415 and OII 4417Å lines, respectively. Vibrational temperature was to be obtained by measuring the ratio of the N_2^+ 1N (0,1) and (1,2) band signals.

In order to apply the phase sensitive synchronous detection technique, the electron beam was magnetically modulated at 250 Hz using two phased coils, carrying 680 mA current, positioned in close proximity to the gun cathode; 90% extinction of the beam was achieved.

Static gas calibration of the instrument was performed for N_2, O_2 and air in the UTIAS space simulator which has a pumping speed of about 10 kℓ/s in the 10^{-8} to 10^{-4} torr pressure range. The blank-off pressure in the simulator is about 10^{-8} torr. A typical calibration curve for the 4270Å channel used for N_2 concentration measurements is presented in Fig. 38 for nitrogen, oxygen and air. The nonlinear portion of the curves at low pressures is partially due to outgassing of the apparatus since it has been noted that an increase in the pumping speed from 150 ℓ/s to 10 kℓ/s results in an extended linear region.

During flight the vehicle developed a large coning motion (about 45°) after despinning and the clamshells struck the EBFP on deployment. Due to some malfunction, still not understood, the vacuum gun cover was not opened; hence no beam was generated in the observation region. The EBFP functioned normally in all other respects; the transformer probe showed that the guns provided beam current except for some arcing during the last 50 s of the flight, probably due to the pressure rise in the gun chamber.

The flight, however, did provide an opportunity to test the background light rejection capabilities of the system. The auroral intensity was > 10 kr but the background signals in all channels were below 10^{-10}A.

6. CONCLUSIONS

The Electron Beam Fluorescence Probe has been successfully applied to obtain simultaneous measurements of neutral gas species concentrations

and nitrogen rotational temperature in the upper atmosphere; the measurement of vibrational temperature can also be made with appropriate spectral detectors. The EBFP diagnostic technique enables such measurements to be made remote from the carrier vehicle and in a continuous and non-perturbing manner.

The altitude range over which the EBFP is most effective is dependent to some extent on the electron beam energy. For a 2.5 keV beam carried at a velocity of a few km/s a lower limit of approximately 65 km is applicable, with the upper altitude being set by the observation time which can be tolerated. Less than 0.05 s is required to complete a determination of the nitrogen concentration at 150 km with 1% precision; this time increases to 1 s at 300 km for 5% precision.

The EBFP is unique in affording the only currently available technique for the direct measurement of rotational temperature. When used for the determination of gas density it has an accuracy comparable to other methods presently available, whilst offering the additional advantage of being a non-perturbing probe.

REFERENCES

1. deLeeuw, J. H. Davies, W.E.R. — Simultaneous Measurement of Temperature and Density by an Electron Beam Luminescence Technique. "Small Rocket Instrumentation Techniques", North Holland Publ. Co., Amsterdam (1969).

2. deLeeuw, J. H. Davies, W.E.R. — Measurement of Temperature and Density in the Upper Atmosphere Using an Electron Beam. Can. J. Phys., 50, 1044 (1972).

3. Muntz, E. P. — The Electron Beam Fluorescence Technique. AGARDograph 132 (1968).

4. Mott, N. F. Massey, H.S.W. — "The Theory of Atomic Collisions". Oxford University Press (Clarendon), London and New York (1952).

5. Haasz, A. A. — Electron Impact Excitation of N_2, O_2 and O_1 and Upper Atmospheric Diagnostics with Electron Beam Fluorescence Probes. Ph.D. Thesis, UTIAS Report No. 194, University of Toronto, Toronto, Ontario, Canada (1973).

6. Petrie, S. L. Boiarski, A. A. Lazdinis, S. S. — Electron Beam Studies of the Properties of Molecular and Atomic Oxygen in Nonequilibrium Flows. AIAA Paper No. 71-271 (1971).

7. Muntz, E. P. — Measurement of Rotational Temperature, Vibrational Temperature and Molecule Concentration in Nonradiating Flows of Low Density Nitrogen. UTIA Report No. 71 (1961).

8. McConkey, J. W. Latimer, I. D. — Proceedings of the Physical Society, Vol. 86, p. 463 (1965).

9. Pierce, J. R. — "Theory and Design of Electron Beams." D. Van Nostrand, N.Y. (1954).

10. Spangenberg, K. R. — "Vacuum Tubes." McGraw-Hill, N.Y. (1948).

11. MacNair, D. — IEEE J. of Quantum Electronics, Vol. QE-5, No. 9, p. 460 (1969).

12. Klemperer, O. — "Electron Optics". Cambridge Univ. Press, 2nd ed. (1953).

13. Goldberg, H. S. — Atmospheric Rotational Temperature Determination by Rocket-borne Electron Gun. A Design Study. B.A.Sc. Thesis, Univ. of Toronto (1966).

14. Beard, D. B. Johnson, F. S. — Ionospheric Limitations on Attainable Satellite Potential. J. Geophysical Res., Vol. 66, No. 12, p. 4113 (1961).

15. Davies, W.E.R. Reduction of Dark Current in Photomultiplier Tubes. Rev. Scient. Inst., 43, 556 (1972).

16. Grenda, R. N. Rocket Measurements of Upper Atmospheric Density and Temperature over Fort Churchill, Manitoba. UTIAS Report No. 117, University of Toronto (1966).

17. Herzberg, G. "Spectra of Diatomic Molecules". D. Van Nostrand, New York (1950).

APPENDIX A: REVIEW OF ATMOSPHERIC MEASUREMENT TECHNIQUES

Much attention has been paid to the lower ionosphere (below 160 km) which has been intensively investigated for its plasma properties since these directly influence the propagation of radio waves. Much effort has also been expended on determining other atmospheric parameters such as the temperature and composition of the neutral constituents. Measurements of these properties have been and still are impeded by a lack of suitable instruments and the necessity for carrying the measuring apparatus through the altitude region of interest.

(1) Ground Based Observations

Sound Skipping

This method had its inception when artillery fire in World War I was heard in certain approximately circular zones, often large distances from the guns, whilst closer locations were silent. The refraction of the sound could be explained by a high temperature region at approximately 40-65 km.

Grenades

The sound technique has also been applied from 30-100 km by microphone observation of the sound transmission times from a sequence of grenade firings, the latter being ejected from a rocket at preselected altitudes. The method gives integrated and combined temperature and density information along the sound path but is limited in altitude to regions where the gas density is sufficiently high to perturb the sound waves.

Balloons and Clouds

From very early times the movements of clouds have provided information on upper atmospheric motions. Noctilucent clouds have been tracked at 600 km/h at 75-90 km. A great deal of information on atmospheric winds is obtained by tracking free balloons; they have been observed with velocities of 300 km/h. Currently, balloons carry a variety of instrumentation but the payloads are restricted in altitude to about 40 km.

Meteors

The commonly observed streaks of light caused by the tiny pinhead size particles of extra-terrestrial matter travelling at about 100 km/s have been extensively studied. The ionization and dissociation of air molecules during the passage of the meteoroid can be observed from about 130 km to 15 km providing information on atmospheric composition and temperature. More recently, radar reflection from these tracks has enabled winds to be monitored in the 80-105 km region.

Aerodynamic Drag Methods

The decay of satellite orbits due to aerodynamic drag has been well documented. Typically, they provide density information at altitudes above 200 km. The radar tracking of spheres released from rockets has also been employed to examine the region below 100 km. The latest methods use

sensitive accelerometers to monitor the drag on a free falling inflated sphere carrying its own transmitter.

Searchlights

With an appropriately located searchlight and detector it is possible to use Mie and Rayleigh scattering to determine the local density along the beam of the searchlight.

Auroral Lights

Intense aurora, adequate for observation, is confined to the polar and sub-polar regions and the altitude range from 60 km to 400 km. Many elements (H, Na, He, O, N, etc.) have been identified in auroral displays. Extensive studies of auroral spectra have enabled vibrational and rotational temperatures to be calculated from ground based observations of the molecular nitrogen emission spectrum.

Seeding

The release of chemicals at high altitudes (above 90 km) enables wind speeds to be obtained from optical tracking of the chemiluminescent radiation caused by the ejected material. Above 120 km spectroscopic examination of the radiation from these trails can also give temperature information. Chemiluminescent materials such as barium and trimethyl aluminum may be observed at night time; others, such as sodium, require excitation from the sun or other sources and these are therefore only useful at twilight.

(2) Flight Observations

A variety of instruments have been developed to enable local measurements of pressure, density, temperature and composition to be made from rockets and satellites. There is no single instrument to this date which permits accurate measurements to be made of the aforementioned parameters from ground level, to say 300 km. The range below about 90 km is fairly well served by some of the devices mentioned in the previous section but the 90 to 250 km range is still a problem area.

Thermistors

The small (0.25 mm diameter) semiconductor beads currently available are ideal for synoptic measurements; they are inexpensive, simple and consume little power. With an appropriate reflective coating they may be used up to 50 km providing corrections are made for radiation, thermal conduction and dynamic heating effects.

Pressure Gauges

Pitot-static probes involve the reduction of data from a forward pointing gauge. Using continuum measurements from wind tunnel studies and making relevant corrections to the flight data extends the use of these devices up to an altitude of 80 km.

Above 90 km, ionization gauges of various types have been used to derive density and temperature information. The reduction of free molecular

gauge data requires a knowledge of the rocket attitude; also, outgassing of the gauge itself is sometimes a serious factor.

Mass Spectrometers

The mass spectrometer is a versatile instrument and is widely used for the determination of atmospheric composition for altitudes above 100 km. By pumping the instrument during flight the operating range can be extended down to about 65 km. Quadrupole, magnetic and R.F. versions have been flown on rockets on many occasions providing data with good height resolution. Satellite-borne mass spectrometers are also widely used. The absorption of atomic oxygen and its desorption as molecular oxygen has restricted the usefulness of the mass spectrometer; however, this problem is now well understood and great care is taken when measuring reactive gases.

Upper atmosphere measuring techniques and their range of applicability are summarized in the table below.

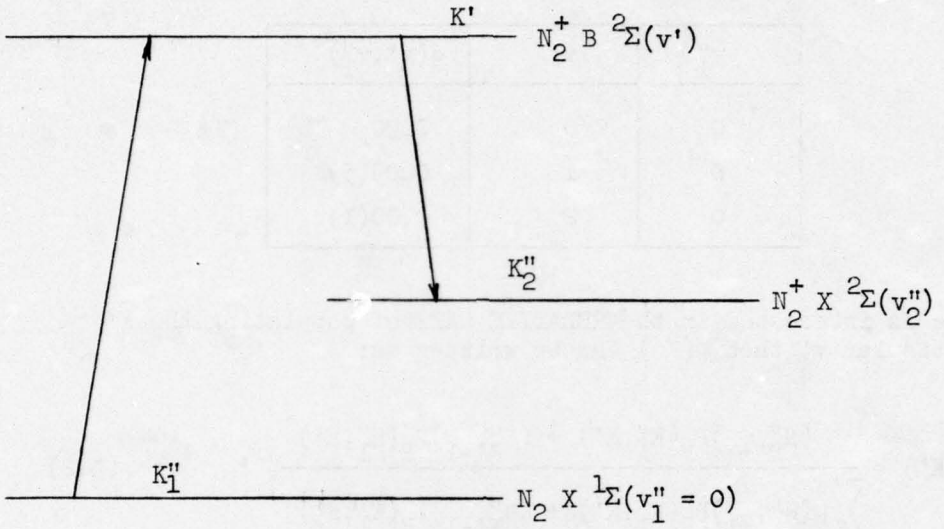
ATMOSPHERIC DIAGNOSTIC TECHNIQUES AND THEIR RANGE OF APPLICABILITY

Altitude (km)	Density	Composition	Temperature	Winds
0-50	Searchlight Falling spheres	Meteors	Thermistors*	Clouds Balloons Chaff
50-100	Pressure gauges Mass spectrometer Falling spheres Grenades	Mass spectrometer Meteors Absorption in spectrum of Sun EBFP †	Grenades EBFP †	Grenades
100-300	EBFP † Aerospec‡	Mass spectrometer EBFP † Aerospec‡ Auroral observation	EBFP † Aerospec‡ Auroral observation	Chemical releases

*Direct and local measurement
†EBFP: 'Electron Beam Fluorescence Probe'
‡Aerospec: 'Aerodynamic Spectrometer', currently being developed at UTIAS

APPENDIX B: RADIATION DISTRIBUTION IN THE N_2^+ 1N SYSTEM VIBRATIONAL BANDS

The electron beam induced N_2^+ 1N system has been studied in detail by several investigators. With the use of Muntz's analysis (Ref. 7), theoretical predictions of the relative intensities of the rotational lines were made for the N_2^+ 1N system vibrational bands.



The following assumptions were made:

(a) The excitation emission process is not affected by gas kinetic collisions.

(b) The vibrational temperature is low ($T_V < 800$ K) and there is no excitation of vibrational levels of N_2 X $^1\Sigma$ other than v" = 0.

(c) The rotational distribution in the $N_2X^1\Sigma$ vibrational levels is assumed to be a Boltzmann distribution.

For high energy electrons, when the excitation function of the electron can be assumed to be constant (independent of wave number), the population rate from the $v_1'' = 0$ level of the N_2 X $^1\Sigma$ state to a rotational level K' of a particular v' of the N_2^+ B $^2\Sigma$ state is:

$$\phi(v',K') = Eq(v',v''_{1=0}) \frac{(N''_{K'+1})P_P(K_1'',K') + (N''_{K'-1})P_R(K_1'',K')}{\sum_{K'=0,1,..} [(N''_{K+1})P_P(K_1'',K') + (N''_{K'-1})P_R(K_1'',K')]} \qquad (B.1)$$

where $q(v',v_1'')$ is the Franck-Condon factor, E the excitation function of the electrons, N" the population of the K_1'' rotational level and $P_P(K_1'',K')$ and

PRECEDING PAGE BLANK-NOT FILMED

$P_R(K_1'',K')$ are the relative rotational transition probabilities or Honl-London factors for the P and R branches, respectively, in the excitation. The expression $\Sigma_{K'}[\ ]$ is a normalizing factor.

The Franck-Condon factors of interest for the transition N_2 X $^1\Sigma$ to N_2^+ B $^2\Sigma$ are given in Ref. 7 as:

v_1''	v'	$q(v',v_1'')$
0	0	0.90
0	1	0.09(5)
0	2	0.00(1)

If one is interested in the RELATIVE RATE of populating the K' levels of a particular v' then $\phi(K')$ can be written as:

$$\phi(K') = \frac{(N''_{K'+1})P_P(K_1'',K') + (N''_{K'-1})P_R(K_1'',K')}{\sum_{K'=0,1,..}[(N''_{K'+1})P_P(K_1'',K') + (N''_{K'-1})P_R(K_1'',K')]} \qquad (B.2)$$

and consequently,

$$\sum_{K'=0,1,2..} \phi(K') = 1 \qquad (B.3)$$

Since the rotational distribution in the N_2 X $^1\Sigma$ vibrational levels is assumed to be Boltzmannian, characterized by the rotational temperature T_R, the relative population of the K_1'' levels of the $v_1'' = 0$ level are:

$$N_{K_1''} = \frac{(N_{v_1''=0})F(2K_1''+1)\exp[-B_{v_1''}K_1''(K_1''+1)hc/kT_R]}{[Q_R(T_R)]_{v_1''=0}} \qquad (B.4)$$

where

$$[Q_R(T_R)]_{v_1''=0} = \sum_{K_1''=0,1,2,..} F(2K_1''+1)\exp[-B_{v_1''}K_1''(K_1''+1)hc/kT_R] \qquad (B.5)$$

and $B_{v_1''}$ is the rotational constant of the v_1'' vibrational level, h is Planck's constant, k is Boltzmann's constant, c is the speed of light, and F is the

population factor for the N_2 X $^1\Sigma$ state resulting from nuclear spin. F = 0.5 for K_1'' = odd and F = 1.0 for K_1'' = even. If the population of the $v_1'' = 0$ vibrational level of the N_2 X $^1\Sigma$ state ($N_{v_1''=0}$) is assumed to be unity, then

$$\sum_{K_1''=0,1,2,..} N_{K_1''} = 1 \tag{B.6}$$

The transition probabilities P_P and P_R for excitation are given by:

P branch $(K_1'' = K' + 1)$: $P_P(K_1'',K') = (K' + 1)/(2K' + 3)$ (B.7)

R branch $(K_1'' = K' - 1)$: $P_R(K_1'',K') = K'/(2K' - 1)$ (B.8)

Then,

$$P_P(K_1'',K')N''_{K'+1} = \frac{F(K'+1)\exp[-B_{v_1''}(K'+1)(K'+2)hc/kT_R]}{[Q_R(T_R)]_{v_1''=0}} \tag{B.9}$$

and

$$P_R(K_1'',K')N''_{K'-1} = \frac{F\,K'\exp[-B_{v_1''}K'(K'-1)hc/kT_R]}{[Q_R(T_R)]_{v_1''=0}} \tag{B.10}$$

With the use of Eqs. B.9 and B.10, Eq. B.2 becomes:

$$\phi(K') = \frac{F(K'+1)\exp[-B_{v_1''}(K'+1)(K'+2)hc/kT_R] + F\,K'\exp[-B_{v_1''}K'(K'-1)hc/kT_R]}{[Q_R(T_R)]_{v_1''=0}\ x\left\{\sum_{K'=0,1,2,..}[(N''_{K'+1})P_P(K_1'',K') + (N''_{K'-1})P_R(K_1'',K')]\right\}} \tag{B.11}$$

The relative intensities of the rotational line emissions (K',K_2'') occurring in a particular vibrational band corresponding to the vibrational levels v' and v_2'' of the N_2^+ B $^2\Sigma$ and N_2^+ X $^2\Sigma$ states, respectively, can be expressed as:

$$I_{K',K_2''} = \frac{\phi(K')q(v',v_2'')P(K',K_2'')hc\,\nu^4_{K',K_2''}}{\sum_{K_2''=\substack{K'+1\\K'-1}}[q(v',v_2'')P(K',K_2'')hc\,\nu^4_{K',K_2''}]} \tag{B.12}$$

where $q(v',v_2'')$ is the Franck-Condon factor for the emission transition, $P(K',K_2'')$ represents the rotational transition probability of the (K',K_2'') rotational line and $\nu_{K',K_2''}$ is the wave number of the emission. For a particular vibrational band of interest $q(v',v_2'')$ is a constant and thus Eq. B.12 can be rewritten as:

$$I_{K',K_2''} = \frac{\phi(K')P(K',K_2'')\ \nu^4_{K',K_2''}}{\sum_{K_2''=K'-1}^{K'+1}[P(K',K_2'')\ \nu^4_{K',K_2''}]} \tag{B.13}$$

For the P and R branches the emission transitions, assuming that the doublet states are not resolved, $P_P(K',K_2'')$ and $P_R(K',K_2'')$ are:

P branch $(K_2'' = K' + 1)$: $P_P(K',K_2'') = (K' + 1)/(2K' + 1)$ (B.14)

R branch $(K_2'' = K' - 1)$: $P_R(K',K_2'') = K'/(2K' + 1)$ (B.15)

Thus, the intensities in the P and R branches are:

$$I^P_{K'} = \frac{\phi(K')(K' + 1)\ \nu^4_P}{[(K' + 1)\ \nu^4_P + K'\ \nu^4_R]} \tag{B.16}$$

$$I^R_{K'} = \frac{\phi(K')\ K'\ \nu^4_R}{[(K' + 1)\ \nu^4_P + K'\ \nu^4_R]} \tag{B.17}$$

The total intensity of all the rotational lines (P and R branches) in a particular vibrational band is:

$$I_{total} = \sum_{K'=0,1,2,..}[I^P_{K'} + I^R_{K'}] = \sum_{K'=0,1,2,..}\phi(K') = 1 \tag{B.18}$$

The wave numbers ν_P and ν_R for the P and R branches of the N_2^+ 1N (0,1) and (1,2) vibrational bands are given by Herzberg (Ref. 17) as:

(0,1) band: $\nu_P = 23{,}397.64 + 3.975(-K'-1) + 0.171(K'+1)^2$ (B.19)

$\nu_R = 23{,}397.64 + 3.975(K') + 0.171\ (K')^2$ (B.20)

(1,2) band: $\nu_P = 23{,}626.66 + 3.936(-K'-1) + 0.172\ (K'+1)^2$ (B.21)

$\nu_R = 23{,}626.66 + 3.936\ (K') \quad + 0.172\ \ (K')^2$ (B.22)

For several rotational temperatures, T_R, relative emission intensities in the P and R branches of emissions originating from the K' level were calculated for the N_2^+ 1N (0,1) and (1,2) vibrational bands. The results are tabulated in Figs. B-1 to B-8. For the (1,2) band the intensities are expressed relative to the (0,1) band intensities. That is, for a particular K' level,

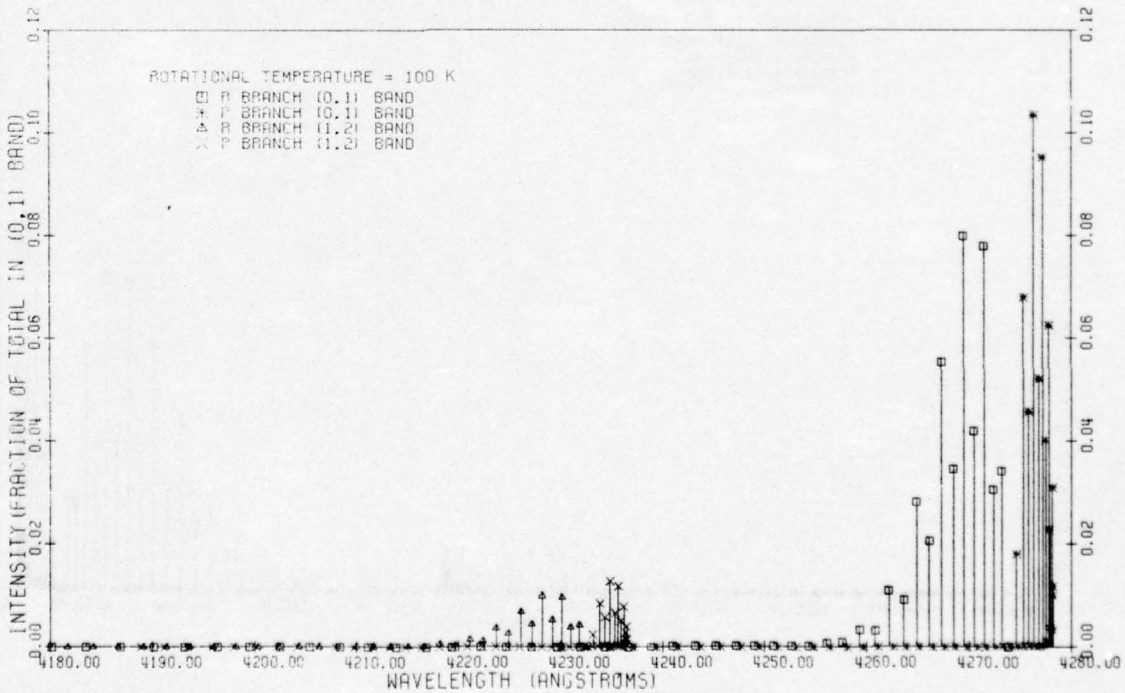
$$\frac{I_{K'}(1,2)}{I_{K'}(0,1)} = \left[\frac{q(0,1)}{q(0,0)} \right]_{\text{excitation}} \times \left[\frac{p(1,2)}{p(0,1)} \right]_{\text{emission}} \tag{B.23}$$

where $p(v',v_2'')$ are the "Smoothed Relative Vibrational Transition Probabilities" for the N_2^+ B $^2\Sigma$ to N_2^+ X $^2\Sigma$ transition. After substitution for the q and p factors (Ref. 7) one obtains:

$$I_{K'}(1,2)/I_{K'}(0,1) = 0.124 \tag{B.24}$$

FIG. 8-1 RELATIVE INTENSITIES IN THE ROTATIONAL LINES OF THE N2PLUS 1N(0,1) AND (1,2) VIBRATIONAL BANDS (ROTATIONAL TEMPERATURE = 100 K)

K'	R BRANCH (0,1) BAND		P BRANCH (0,1) BAND		R BRANCH (1,2) BAND		P BRANCH (1,2) BAND	
	WAVELENGTH (A)	INTENSITY I K'R(0,1)	WAVELENGTH (A)	INTENSITY I K'P(0,1)	WAVELENGTH (A)	INTENSITY I K'R(1,2)	WAVELENGTH (A)	INTENSITY I K'P(1,2)
0	4273.936	0.000E+00	4274.631	1.794E-02	4232.507	0.000E+00	4233.181	2.207E-03
1	4273.179	3.403E-02	4275.264	6.794E-02	4231.771	4.188E-03	4233.794	8.340E-03
2	4272.360	3.056E-02	4275.834	4.569E-02	4230.974	3.760E-03	4234.346	5.622E-03
3	4271.479	7.796E-02	4276.342	1.034E-01	4230.116	9.593E-03	4234.836	1.273E-02
4	4270.535	4.186E-02	4276.788	5.202E-02	4229.197	5.151E-03	4235.265	6.402E-03
5	4269.530	7.983E-02	4277.171	9.512E-02	4228.217	9.822E-03	4235.632	1.170E-02
6	4268.463	3.460E-02	4277.492	4.002E-02	4227.176	4.257E-03	4235.938	4.925E-03
7	4267.335	5.521E-02	4277.750	6.249E-02	4226.074	6.793E-03	4236.182	7.690E-03
8	4266.144	2.042E-02	4277.946	2.272E-02	4224.911	2.513E-03	4236.364	2.797E-03
9	4264.893	2.817E-02	4278.079	3.091E-02	4223.688	3.465E-03	4236.485	3.804E-03
10	4263.579	9.077E-03	4278.149	9.850E-03	4222.404	1.116E-03	4236.544	1.212E-03
11	4262.205	1.096E-02	4278.157	1.178E-02	4221.059	1.348E-03	4236.541	1.449E-03
12	4260.769	3.105E-03	4278.103	3.309E-03	4219.655	3.820E-04	4236.477	4.073E-04
13	4259.273	3.305E-03	4277.986	3.497E-03	4218.190	4.066E-04	4236.351	4.304E-04
14	4257.715	8.271E-04	4277.806	8.656E-04	4216.665	1.017E-04	4236.163	1.070E-04
15	4256.097	7.749E-04	4277.564	8.143E-04	4215.080	9.582E-05	4235.914	1.002E-04
16	4254.418	1.726E-04	4277.259	1.795E-04	4213.436	2.123E-05	4235.603	2.209E-05
17	4252.678	1.441E-04	4276.892	1.491E-04	4211.731	1.773E-05	4235.231	1.836E-05
18	4250.878	2.834E-05	4276.463	2.921E-05	4209.968	3.486E-06	4234.797	3.595E-06
19	4249.018	2.100E-05	4275.971	2.156E-05	4208.145	2.584E-06	4234.302	2.653E-06
20	4247.098	3.669E-06	4275.416	3.751E-06	4206.262	4.513E-07	4233.745	4.617E-07
21	4245.118	2.416E-06	4274.800	2.461E-06	4204.321	2.972E-07	4233.127	3.030E-07
22	4243.079	3.750E-07	4274.121	3.808E-07	4202.321	4.613E-08	4232.447	4.687E-08
23	4240.980	2.195E-07	4273.380	2.222E-07	4200.262	2.701E-08	4231.706	2.735E-08
24	4238.821	3.030E-08	4272.576	3.058E-08	4198.144	3.727E-09	4230.904	3.764E-09
25	4236.604	1.577E-08	4271.711	1.587E-08	4195.969	1.940E-09	4230.041	1.954E-09
26	4234.327	1.336E-09	4270.784	1.943E-09	4193.735	2.382E-10	4229.117	2.392E-10
27	4231.992	8.668E-10	4269.795	8.976E-10	4191.443	1.103E-10	4228.131	1.104E-10
28	4229.598	9.794E-11	4268.743	9.777E-11	4189.093	1.204E-11	4227.085	1.203E-11
29	4227.146	4.035E-11	4267.631	4.018E-11	4186.686	4.963E-12	4225.978	4.946E-12
30	4224.635	3.921E-12	4266.456	3.895E-12	4184.221	4.823E-13	4224.810	4.795E-13
31	4222.067	1.437E-12	4265.220	1.425E-12	4181.699	1.768E-13	4223.581	1.754E-13
32	4219.441	1.243E-13	4263.923	1.229E-13	4179.121	1.529E-14	4222.292	1.513E-14
33	4216.757	4.057E-14	4262.564	4.003E-14	4176.485	4.990E-15	4220.943	4.928E-15
34	4214.016	3.122E-15	4261.144	3.074E-15	4173.793	3.840E-16	4219.533	3.785E-16
35	4211.218	9.070E-16	4259.663	8.912E-16	4171.045	1.115E-16	4218.063	1.097E-16
36	4208.363	6.213E-17	4258.121	6.093E-17	4168.240	7.642E-18	4216.533	7.500E-18
37	4205.452	1.606E-17	4256.519	1.572E-17	4165.380	1.975E-18	4214.944	1.935E-18
38	4202.484	9.797E-19	4254.855	9.569E-19	4162.464	1.204E-19	4213.293	1.178E-19
39	4199.461	2.255E-19	4253.131	2.198E-19	4159.493	2.773E-20	4211.585	2.706E-20
40	4196.381	1.224E-20	4251.347	1.191E-20	4156.467	1.505E-21	4209.816	1.466E-21
41	4193.246	2.509E-21	4249.502	2.436E-21	4153.386	3.085E-22	4207.988	3.000E-22
42	4190.055	1.212E-22	4247.598	1.175E-22	4150.250	1.491E-23	4206.100	1.447E-23
43	4186.810	2.213E-23	4245.633	2.141E-23	4147.060	2.721E-24	4204.154	2.636E-24
44	4183.509	9.525E-25	4243.609	9.201E-25	4143.816	1.171E-25	4202.149	1.132E-25
45	4180.154	1.547E-25	4241.525	1.492E-25	4140.518	1.903E-26	4200.085	1.837E-26
46	4176.745	5.931E-27	4239.382	5.709E-27	4137.166	7.293E-28	4197.963	7.029E-28
47	4173.282	8.580E-28	4237.180	8.246E-28	4133.761	1.055E-28	4195.782	1.015E-28
48	4169.765	2.928E-29	4234.918	2.809E-29	4130.303	3.601E-30	4193.543	3.459E-30
49	4166.195	3.772E-30	4232.598	3.613E-30	4126.793	4.639E-31	4191.246	4.449E-31
50	4162.571	1.146E-31	4230.219	1.096E-31	4123.230	1.410E-32	4188.892	1.350E-32



PRECEDING PAGE BLANK-NOT FILMED

FIG. B-2 RELATIVE INTENSITIES IN THE ROTATIONAL LINES OF THE N2PLUS 1N(0,1) AND (1,2) VIBRATIONAL BANDS (ROTATIONAL TEMPERATURE = 200 K)

K'	R BRANCH (0,1) BAND		P BRANCH (0,1) BAND		R BRANCH (1,2) BAND		P BRANCH (1,2) BAND	
	WAVELENGTH (A)	INTENSITY I K'R(0,1)	WAVELENGTH (A)	INTENSITY I K'P(0,1)	WAVELENGTH (A)	INTENSITY I K'R(1,2)	WAVELENGTH (A)	INTENSITY I K'P(1,2)
0	4273.936	0.000E+00	4274.631	9.278E-03	4232.507	0.000E+00	4233.181	1.141E-03
1	4273.179	1.806E-02	4275.264	3.606E-02	4231.771	2.223E-03	4233.794	4.437E-03
2	4272.360	1.709E-02	4275.834	2.556E-02	4230.974	2.103E-03	4234.346	3.148E-03
3	4271.479	4.719E-02	4276.342	6.264E-02	4230.116	5.807E-03	4234.836	7.708E-03
4	4270.535	2.815E-02	4276.788	3.498E-02	4229.197	3.464E-03	4235.265	4.305E-03
5	4269.530	6.124E-02	4277.171	7.296E-02	4228.217	7.535E-03	4235.632	8.979E-03
6	4268.463	3.109E-02	4277.492	3.596E-02	4227.176	3.825E-03	4235.938	4.426E-03
7	4267.335	5.969E-02	4277.750	6.755E-02	4226.074	7.343E-03	4236.182	8.313E-03
8	4266.144	2.728E-02	4277.946	3.036E-02	4224.911	3.357E-03	4236.364	3.736E-03
9	4264.893	4.776E-02	4278.079	5.242E-02	4223.688	5.876E-03	4236.485	6.451E-03
10	4263.579	2.007E-02	4278.149	2.178E-02	4222.404	2.469E-03	4236.544	2.680E-03
11	4262.205	3.248E-02	4278.157	3.491E-02	4221.059	3.996E-03	4236.541	4.296E-03
12	4260.769	1.267E-02	4278.103	1.350E-02	4219.655	1.559E-03	4236.477	1.662E-03
13	4259.273	1.909E-02	4277.986	2.021E-02	4218.190	2.349E-03	4236.351	2.487E-03
14	4257.715	6.954E-03	4277.806	7.311E-03	4216.665	8.555E-04	4236.163	8.998E-04
15	4256.097	9.797E-03	4277.564	1.074E-02	4215.080	1.205E-03	4235.914	1.260E-03
16	4254.418	3.340E-03	4277.259	3.474E-03	4213.436	4.109E-04	4235.603	4.275E-04
17	4252.678	4.412E-03	4276.892	4.566E-03	4211.731	5.427E-04	4235.231	5.620E-04
18	4250.878	1.411E-03	4276.463	1.454E-03	4209.968	1.736E-04	4234.797	1.790E-04
19	4249.018	1.750E-03	4275.971	1.796E-03	4208.145	2.153E-04	4234.302	2.211E-04
20	4247.098	5.263E-04	4275.416	5.381E-04	4206.262	6.474E-05	4233.745	6.623E-05
21	4245.118	6.138E-04	4274.800	6.254E-04	4204.321	7.551E-05	4233.127	7.697E-05
22	4243.079	1.735E-04	4274.121	1.762E-04	4202.321	2.135E-05	4232.447	2.169E-05
23	4240.980	1.905E-04	4273.380	1.928E-04	4200.262	2.343E-05	4231.706	2.373E-05
24	4238.821	5.071E-05	4272.576	5.118E-05	4198.144	6.238E-06	4230.904	6.299E-06
25	4236.604	5.241E-05	4271.711	5.273E-05	4195.969	6.447E-06	4230.041	6.491E-06
26	4234.327	1.314E-05	4270.784	1.318E-05	4193.735	1.616E-06	4229.117	1.623E-06
27	4231.992	1.279E-05	4269.795	1.280E-05	4191.443	1.573E-06	4228.131	1.576E-06
28	4229.598	3.022E-06	4268.743	3.017E-06	4189.093	3.718E-07	4227.085	3.714E-07
29	4227.146	2.773E-06	4267.631	2.761E-06	4186.686	3.411E-07	4225.978	3.399E-07
30	4224.635	6.176E-07	4266.456	6.135E-07	4184.221	7.596E-08	4224.810	7.552E-08
31	4222.067	5.342E-07	4265.220	5.294E-07	4181.699	6.570E-08	4223.581	6.517E-08
32	4219.441	1.121E-07	4263.923	1.109E-07	4179.121	1.379E-08	4222.292	1.365E-08
33	4216.757	9.146E-08	4262.564	9.025E-08	4176.485	1.125E-08	4220.943	1.111E-08
34	4214.016	1.810E-08	4261.144	1.783E-08	4173.793	2.227E-09	4219.533	2.194E-09
35	4211.218	1.392E-08	4259.663	1.368E-08	4171.045	1.712E-09	4218.063	1.684E-09
36	4208.363	2.600E-09	4258.121	2.549E-09	4168.240	3.198E-10	4216.533	3.139E-10
37	4205.452	1.886E-09	4256.519	1.845E-09	4165.380	2.319E-10	4214.944	2.272E-10
38	4202.484	3.322E-10	4254.855	3.244E-10	4162.464	4.085E-11	4213.294	3.994E-11
39	4199.461	2.273E-10	4253.131	2.215E-10	4159.493	2.795E-11	4211.585	2.727E-11
40	4196.381	3.776E-11	4251.347	3.674E-11	4156.467	4.644E-12	4209.816	4.523E-12
41	4193.246	2.437E-11	4249.502	2.367E-11	4153.386	2.997E-12	4207.988	2.914E-12
42	4190.055	3.820E-12	4247.598	3.703E-12	4150.250	4.698E-13	4206.100	4.559E-13
43	4186.810	2.326E-12	4245.633	2.251E-12	4147.060	2.860E-13	4204.154	2.771E-13
44	4183.509	3.439E-13	4243.609	3.323E-13	4143.816	4.230E-14	4202.149	4.091E-14
45	4180.154	1.976E-13	4241.525	1.905E-13	4140.518	2.430E-14	4200.085	2.346E-14
46	4176.745	2.757E-14	4239.382	2.654E-14	4137.166	3.390E-15	4197.963	3.268E-15
47	4173.282	1.494E-14	4237.180	1.436E-14	4133.761	1.838E-15	4195.782	1.768E-15
48	4169.765	1.967E-15	4234.918	1.887E-15	4130.303	2.419E-16	4193.543	2.324E-16
49	4166.195	1.006E-15	4232.598	9.639E-16	4126.793	1.237E-16	4191.246	1.186E-16
50	4162.571	1.249E-16	4230.219	1.195E-16	4123.230	1.537E-17	4188.892	1.471E-17

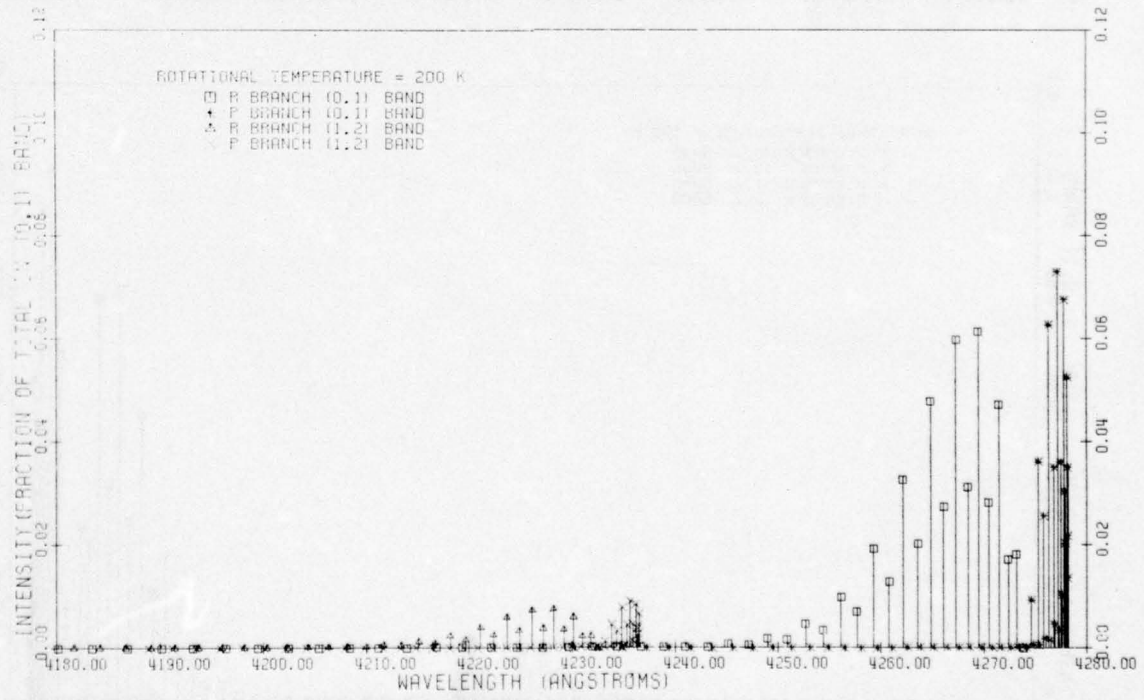


FIG. B-3 RELATIVE INTENSITIES IN THE ROTATIONAL LINES OF THE N2PLUS IN(0,1) AND (1,2) VIBRATIONAL BANDS (ROTATIONAL TEMPERATURE = 300 K)

K'	R BRANCH (0,1) BAND		P BRANCH (0,1) BAND		R BRANCH (1,2) BAND		P BRANCH (1,2) BAND	
	WAVELENGTH (A)	INTENSITY I K'R(0,1)	WAVELENGTH (A)	INTENSITY I K'P(0,1)	WAVELENGTH (A)	INTENSITY I K'R(1,2)	WAVELENGTH (A)	INTENSITY I K'P(1,2)
0	4273.936	0.000E+00	4274.631	6.255E-03	4232.507	0.000E+00	4233.181	7.696E-04
1	4273.179	1.229E-02	4275.264	2.453E-02	4231.771	1.512E-03	4233.794	3.019E-03
2	4272.360	1.184E-02	4275.834	1.771E-02	4230.974	1.457E-03	4234.346	2.179E-03
3	4271.479	3.361E-02	4276.342	4.461E-02	4230.116	4.135E-03	4234.836	5.489E-03
4	4270.535	2.019E-02	4276.788	2.584E-02	4229.197	2.558E-03	4235.265	3.180E-03
5	4269.530	4.735E-02	4277.171	5.641E-02	4228.217	5.825E-03	4235.632	6.942E-03
6	4268.463	2.539E-02	4277.492	2.937E-02	4227.176	3.124E-03	4235.938	3.614E-03
7	4267.335	5.196E-02	4277.750	5.881E-02	4226.074	6.394E-03	4236.182	7.237E-03
8	4266.144	2.556E-02	4277.946	2.844E-02	4224.911	3.144E-03	4236.364	3.499E-03
9	4264.893	4.858E-02	4278.079	5.331E-02	4223.688	5.977E-03	4236.485	6.561E-03
10	4263.579	2.237E-02	4278.149	2.427E-02	4222.404	2.752E-03	4236.544	2.987E-03
11	4262.205	4.004E-02	4278.157	4.303E-02	4221.059	4.926E-03	4236.541	5.295E-03
12	4260.769	1.743E-02	4278.103	1.858E-02	4219.655	2.145E-03	4236.477	2.287E-03
13	4259.273	2.959E-02	4277.986	3.131E-02	4218.190	3.640E-03	4236.351	3.854E-03
14	4257.715	1.225E-02	4277.806	1.288E-02	4216.665	1.507E-03	4236.163	1.585E-03
15	4256.097	1.980E-02	4277.564	2.070E-02	4215.080	2.436E-03	4235.914	2.548E-03
16	4254.418	7.819E-03	4277.259	8.132E-03	4213.436	9.620E-04	4235.603	1.000E-03
17	4252.678	1.207E-02	4276.892	1.249E-02	4211.731	1.485E-03	4235.231	1.537E-03
18	4250.878	4.556E-03	4276.463	4.695E-03	4209.968	5.605E-04	4234.797	5.779E-04
19	4249.018	6.729E-03	4275.971	6.907E-03	4208.145	8.278E-04	4234.302	8.501E-04
20	4247.098	2.431E-03	4275.416	2.486E-03	4206.262	2.991E-04	4233.745	3.060E-04
21	4245.118	3.440E-03	4274.800	3.505E-03	4204.321	4.231E-04	4233.127	4.314E-04
22	4243.079	1.191E-03	4274.121	1.209E-03	4202.321	1.465E-04	4232.447	1.488E-04
23	4240.980	1.615E-03	4273.380	1.635E-03	4200.262	1.987E-04	4231.706	2.013E-04
24	4238.821	5.367E-04	4272.576	5.416E-04	4198.144	6.602E-05	4230.904	6.666E-05
25	4236.604	6.984E-04	4271.711	7.028E-04	4195.969	8.591E-05	4230.041	8.651E-05
26	4234.327	2.226E-04	4270.784	2.234E-04	4193.735	2.738E-05	4229.117	2.750E-05
27	4231.992	2.781E-04	4269.795	2.783E-04	4191.443	3.421E-05	4228.131	3.426E-05
28	4229.598	8.512E-05	4268.743	8.497E-05	4189.093	1.047E-05	4227.085	1.046E-05
29	4227.146	1.021E-04	4267.631	1.017E-04	4186.686	1.256E-05	4225.978	1.251E-05
30	4224.635	3.002E-05	4266.456	2.982E-05	4184.221	3.692E-06	4224.810	3.671E-06
31	4222.067	3.460E-05	4265.220	3.429E-05	4181.699	4.255E-06	4223.581	4.221E-06
32	4219.441	9.772E-06	4263.923	9.664E-06	4179.121	1.202E-06	4222.292	1.189E-06
33	4216.757	1.082E-05	4262.564	1.067E-05	4176.485	1.331E-06	4220.943	1.314E-06
34	4214.016	2.937E-06	4261.144	2.892E-06	4173.793	3.613E-07	4219.533	3.560E-07
35	4211.218	3.126E-06	4259.663	3.072E-06	4171.045	3.845E-07	4218.063	3.782E-07
36	4208.363	8.157E-07	4258.121	7.998E-07	4168.240	1.003E-07	4216.533	9.846E-08
37	4205.452	8.346E-07	4256.519	8.167E-07	4165.380	1.026E-07	4214.944	1.005E-07
38	4202.484	2.093E-07	4254.855	2.044E-07	4162.464	2.574E-08	4213.294	2.516E-08
39	4199.461	2.059E-07	4253.131	2.007E-07	4159.493	2.532E-08	4211.585	2.471E-08
40	4196.381	4.965E-08	4251.347	4.831E-08	4156.467	6.106E-09	4209.816	5.947E-09
41	4193.246	4.696E-08	4249.502	4.561E-08	4153.386	5.775E-09	4207.988	5.615E-09
42	4190.055	1.088E-09	4247.598	1.055E-08	4150.250	1.339E-09	4206.100	1.299E-09
43	4186.810	9.904E-09	4245.633	9.584E-09	4147.060	1.218E-09	4204.154	1.180E-09
44	4183.509	2.208E-09	4243.609	2.133E-09	4143.816	2.716E-10	4202.149	2.626E-10
45	4180.154	1.931E-09	4241.525	1.862E-09	4140.518	2.375E-10	4200.085	2.293E-10
46	4176.745	4.142E-10	4239.382	3.988E-10	4137.166	5.094E-11	4197.963	4.910E-11
47	4173.282	3.485E-10	4237.180	3.349E-10	4133.761	4.285E-11	4195.782	4.123E-11
48	4169.765	7.188E-11	4234.918	6.896E-11	4130.303	8.839E-12	4193.543	8.491E-12
49	4166.195	5.816E-11	4232.598	5.571E-11	4126.793	7.152E-12	4191.246	6.859E-12
50	4162.571	1.153E-11	4230.219	1.103E-11	4123.230	1.418E-12	4188.892	1.358E-12

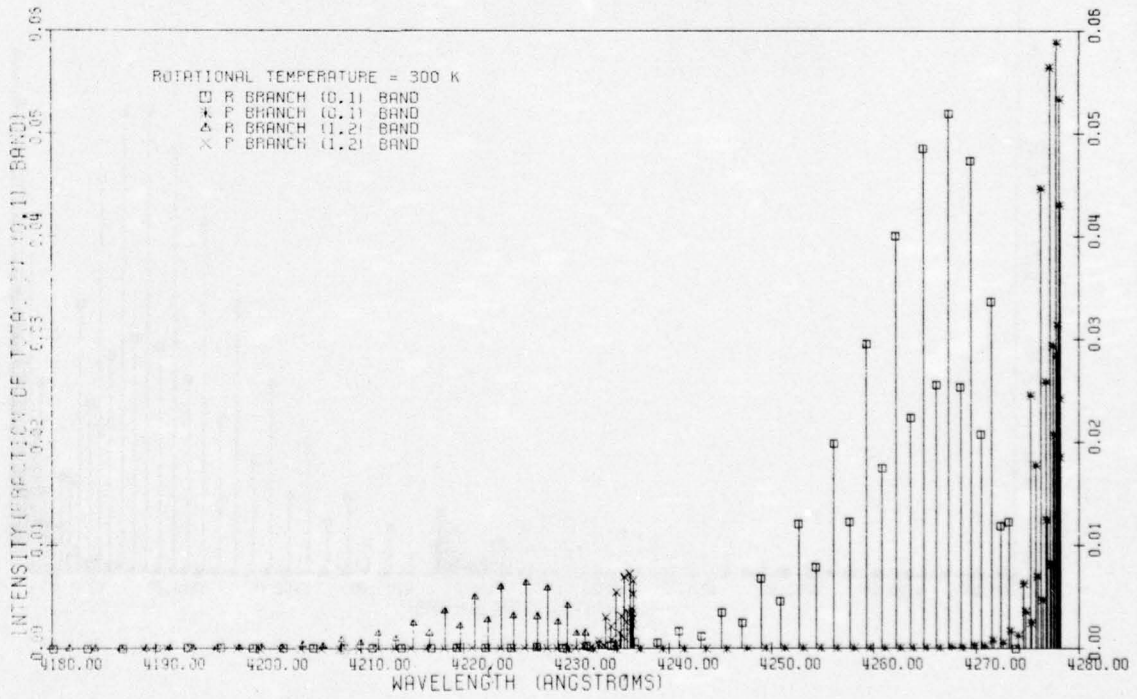


FIG. B-4 RELATIVE INTENSITIES IN THE ROTATIONAL LINES OF THE N2PLUS IN(0,1) AND (1,2) VIBRATIONAL BANDS (ROTATIONAL TEMPERATURE = 400 K)

K'	R BRANCH (0,1) BAND		P BRANCH (0,1) BAND		R BRANCH (1,2) BAND		P BRANCH (1,2) BAND	
	WAVELENGTH (A)	INTENSITY I K'R(0,1)	WAVELENGTH (A)	INTENSITY I K'P(0,1)	WAVELENGTH (A)	INTENSITY I K'R(1,2)	WAVELENGTH (A)	INTENSITY I K'P(1,2)
0	4273.936	0.000E+00	4274.631	4.717E-03	4232.507	0.000E+00	4233.181	5.804E-04
1	4273.179	9.314E-03	4275.264	1.859E-02	4231.771	1.146E-03	4233.794	2.287E-03
2	4272.360	9.059E-03	4275.834	1.354E-02	4230.974	1.114E-03	4234.346	1.666E-03
3	4271.479	2.606E-02	4276.342	3.459E-02	4230.116	3.206E-03	4234.836	4.256E-03
4	4270.535	1.642E-02	4276.788	2.041E-02	4229.197	2.021E-03	4235.265	2.512E-03
5	4269.530	3.828E-02	4277.171	4.561E-02	4228.217	4.710E-03	4235.632	5.612E-03
6	4268.463	2.110E-02	4277.492	2.442E-02	4227.176	2.597E-03	4235.938	3.005E-03
7	4267.335	4.462E-02	4277.750	5.050E-02	4226.074	5.490E-03	4236.182	6.215E-03
8	4266.144	2.278E-02	4277.946	2.534E-02	4224.911	2.802E-03	4236.364	3.119E-03
9	4264.893	4.514E-02	4278.079	4.954E-02	4223.688	5.553E-03	4236.485	6.096E-03
10	4263.579	2.177E-02	4278.149	2.362E-02	4222.404	2.679E-03	4236.544	2.907E-03
11	4262.205	4.101E-02	4278.157	4.407E-02	4221.059	5.045E-03	4236.541	5.424E-03
12	4260.769	1.888E-02	4278.103	2.012E-02	4219.655	2.322E-03	4236.477	2.476E-03
13	4259.273	3.404E-02	4277.986	3.602E-02	4218.190	4.187E-03	4236.351	4.433E-03
14	4257.715	1.563E-02	4277.806	1.581E-02	4216.665	1.849E-03	4236.163	1.945E-03
15	4256.097	2.606E-02	4277.564	2.724E-02	4215.080	3.206E-03	4235.914	3.353E-03
16	4254.418	1.108E-02	4277.259	1.152E-02	4213.436	1.363E-03	4235.603	1.418E-03
17	4252.678	1.851E-02	4276.892	1.916E-02	4211.731	2.278E-03	4235.231	2.358E-03
18	4250.878	7.598E-03	4276.463	7.830E-03	4209.968	9.347E-04	4234.797	9.637E-04
19	4249.018	1.225E-02	4275.971	1.258E-02	4208.145	1.507E-03	4234.302	1.548E-03
20	4247.098	4.860E-03	4275.416	4.969E-03	4206.262	5.979E-04	4233.745	6.116E-04
21	4245.118	7.581E-03	4274.800	7.724E-03	4204.321	9.326E-04	4233.127	9.507E-04
22	4243.079	2.950E-03	4274.121	2.953E-03	4202.321	3.577E-04	4232.447	3.634E-04
23	4240.980	4.350E-03	4273.380	4.443E-03	4200.262	5.400E-04	4231.706	5.469E-04
24	4238.821	1.630E-03	4272.576	1.645E-03	4198.144	2.005E-04	4230.904	2.025E-04
25	4236.604	2.383E-03	4271.711	2.398E-03	4195.969	2.931E-04	4230.041	2.952E-04
26	4234.327	8.574E-04	4270.784	8.604E-04	4193.735	1.054E-04	4229.117	1.059E-04
27	4231.992	1.214E-03	4269.795	1.215E-03	4191.443	1.494E-04	4228.131	1.496E-04
28	4229.598	4.235E-04	4268.743	4.227E-04	4189.093	5.209E-05	4227.085	5.204E-05
29	4227.146	5.816E-04	4267.631	5.791E-04	4186.686	7.154E-05	4225.978	7.129E-05
30	4224.635	1.966E-04	4266.456	1.953E-04	4184.221	2.418E-05	4224.810	2.404E-05
31	4222.067	2.618E-04	4265.220	2.595E-04	4181.699	3.220E-05	4223.581	3.194E-05
32	4219.441	8.585E-05	4263.923	8.489E-05	4179.121	1.055E-05	4222.292	1.045E-05
33	4216.757	1.108E-04	4262.564	1.094E-04	4176.485	1.363E-05	4220.943	1.347E-05
34	4214.016	3.527E-05	4261.144	3.473E-05	4173.793	4.338E-06	4219.533	4.275E-06
35	4211.218	4.420E-05	4259.663	4.343E-05	4171.045	5.436E-06	4218.063	5.347E-06
36	4208.363	1.364E-05	4258.121	1.337E-05	4168.240	1.677E-06	4216.533	1.646E-06
37	4205.452	1.659E-05	4256.519	1.623E-05	4165.390	2.040E-06	4214.944	1.998E-06
38	4202.484	4.965E-06	4254.855	4.853E-06	4162.484	6.111E-07	4213.294	5.975E-07
39	4199.461	5.865E-06	4253.131	5.718E-06	4159.493	7.213E-07	4211.585	7.039E-07
40	4196.381	1.705E-06	4251.347	1.659E-06	4156.467	2.097E-07	4209.816	2.042E-07
41	4193.246	1.953E-06	4249.502	1.897E-06	4153.386	2.402E-07	4207.988	2.335E-07
42	4190.055	5.513E-07	4247.598	5.344E-07	4150.250	6.780E-08	4206.100	6.580E-08
43	4186.810	6.131E-07	4245.633	5.934E-07	4147.060	7.541E-08	4204.154	7.305E-08
44	4183.509	1.679E-07	4243.609	1.622E-07	4143.816	2.066E-08	4202.149	1.998E-08
45	4180.154	1.814E-07	4241.525	1.749E-07	4140.518	2.230E-08	4200.085	2.153E-08
46	4176.745	4.825E-08	4239.382	4.645E-08	4137.166	5.934E-09	4197.963	5.719E-09
47	4173.282	5.059E-08	4237.180	4.862E-08	4133.761	6.221E-09	4195.782	5.986E-09
48	4169.765	1.306E-08	4234.918	1.253E-08	4130.303	1.606E-09	4193.543	1.543E-09
49	4166.195	1.330E-08	4232.598	1.274E-08	4126.793	1.635E-09	4191.246	1.568E-09
50	4162.571	3.336E-09	4230.219	3.190E-09	4123.230	4.102E-10	4188.892	3.928E-10

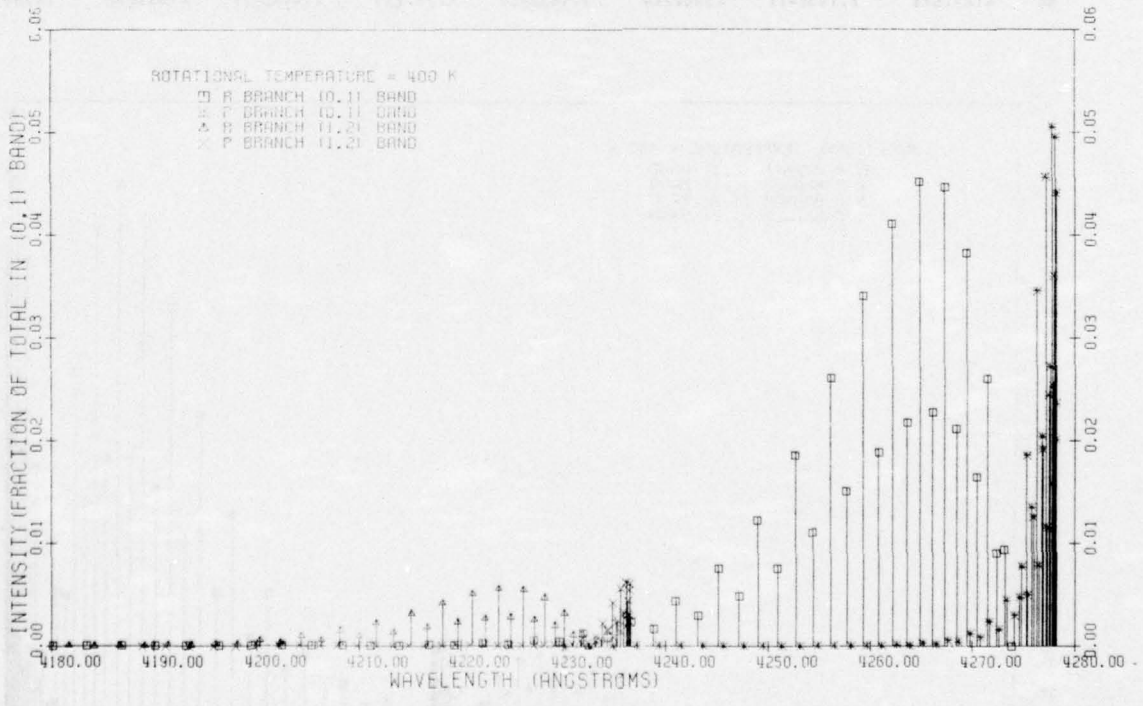


FIG. B-5 RELATIVE INTENSITIES IN THE ROTATIONAL LINES OF THE N2PLUS 1N(0,1) AND (1,2) VIBRATIONAL BANDS (RCTATIONAL TEMPERATURE = 500 K)

K'	R BRANCH (0,1) BAND		P BRANCH (0,1) BAND		R BRANCH (1,2) BAND		P BRANCH (1,2) BAND	
	WAVELENGTH (A)	INTENSITY I K'R(0,1)	WAVELENGTH (A)	INTENSITY I K'P(0,1)	WAVELENGTH (A)	INTENSITY I K'R(1,2)	WAVELENGTH (A)	INTENSITY I K'P(1,2)
0	4273.936	0.000E+00	4274.631	3.786E-03	4232.507	0.000E+00	4233.181	4.659E-04
1	4273.179	7.497E-03	4275.264	1.496E-02	4231.771	9.225E-04	4233.794	1.841E-03
2	4272.360	7.333E-03	4275.834	1.096E-02	4230.974	9.023E-04	4234.346	1.349E-03
3	4271.479	2.127E-02	4276.342	2.823E-02	4230.116	2.617E-03	4234.836	3.474E-03
4	4270.535	1.356E-02	4276.788	1.685E-02	4229.197	1.668E-03	4235.265	2.073E-03
5	4269.530	3.204E-02	4277.171	3.818E-02	4228.217	3.943E-03	4235.632	4.698E-03
6	4268.463	1.797E-02	4277.492	2.079E-02	4227.176	2.211E-03	4235.938	2.558E-03
7	4267.335	3.374E-02	4277.750	4.385E-02	4226.074	4.767E-03	4236.182	5.396E-03
8	4266.144	2.022E-02	4277.946	2.250E-02	4224.911	2.488E-03	4236.364	2.769E-03
9	4264.893	4.110E-02	4278.079	4.511E-02	4223.688	5.057E-03	4236.485	5.552E-03
10	4263.579	2.039E-02	4278.149	2.212E-02	4222.404	2.509E-03	4236.544	2.723E-03
11	4262.205	3.961E-02	4278.157	4.257E-02	4221.059	4.873E-03	4236.541	5.239E-03
12	4260.769	1.886E-02	4278.103	2.010E-02	4219.655	2.320E-03	4236.477	2.474E-03
13	4259.273	3.526E-02	4277.986	3.731E-02	4218.190	4.338E-03	4236.351	4.592E-03
14	4257.715	1.620E-02	4277.806	1.703E-02	4216.665	1.993E-03	4236.163	2.096E-03
15	4256.097	2.929E-02	4277.564	3.062E-02	4215.080	3.603E-03	4235.914	3.768E-03
16	4254.418	1.302E-02	4277.259	1.354E-02	4213.436	1.602E-03	4235.603	1.667E-03
17	4252.678	2.282E-02	4276.892	2.362E-02	4211.731	2.808E-03	4235.231	2.908E-03
18	4250.878	9.853E-03	4276.463	1.015E-02	4209.968	1.212E-03	4234.797	1.249E-03
19	4249.018	1.676E-02	4275.971	1.720E-02	4208.145	2.062E-03	4234.302	2.117E-03
20	4247.098	7.032E-03	4275.416	7.190E-03	4206.262	8.650E-04	4233.745	8.849E-04
21	4245.118	1.163E-02	4274.800	1.185E-02	4204.321	1.431E-03	4233.127	1.459E-03
22	4243.079	4.747E-03	4274.121	4.820E-03	4202.321	5.839E-04	4232.447	5.933E-04
23	4240.980	7.544E-03	4273.380	7.737E-03	4200.262	9.403E-04	4231.706	9.523E-04
24	4238.821	3.036E-03	4272.576	3.064E-03	4198.144	3.735E-04	4230.904	3.772E-04
25	4236.604	4.762E-03	4271.711	4.792E-03	4195.969	5.858E-04	4230.041	5.898E-04
26	4234.327	1.843E-03	4270.784	1.849E-03	4193.735	2.267E-04	4229.117	2.276E-04
27	4231.992	2.816E-03	4269.795	2.819E-03	4191.443	3.464E-04	4228.131	3.469E-04
28	4229.598	1.062E-03	4268.743	1.060E-03	4189.093	1.306E-04	4227.085	1.305E-04
29	4227.146	1.583E-03	4267.631	1.576E-03	4186.686	1.947E-04	4225.978	1.940E-04
30	4224.635	5.822E-04	4266.456	5.783E-04	4184.221	7.161E-05	4224.810	7.119E-05
31	4222.067	8.459E-04	4265.220	8.384E-04	4181.699	1.040E-04	4223.581	1.032E-04
32	4219.441	3.034E-04	4263.923	3.001E-04	4179.121	3.732E-05	4222.292	3.694E-05
33	4216.757	4.301E-04	4262.564	4.244E-04	4176.485	5.290E-05	4220.943	5.224E-05
34	4214.016	1.505E-04	4261.144	1.482E-04	4173.793	1.851E-05	4219.533	1.824E-05
35	4211.218	2.081E-04	4259.663	2.045E-04	4171.045	2.560E-05	4218.063	2.518E-05
36	4208.363	7.109E-05	4258.121	6.971E-05	4168.240	8.744E-06	4216.533	8.582E-06
37	4205.452	9.595E-05	4256.519	9.390E-05	4165.380	1.180E-05	4214.944	1.155E-05
38	4202.484	3.198E-05	4254.855	3.123E-05	4162.464	3.933E-06	4213.294	3.845E-06
39	4199.461	4.312E-05	4253.131	4.206E-05	4159.493	5.181E-06	4211.585	5.056E-06
40	4196.381	1.370E-05	4251.347	1.333E-05	4156.467	1.685E-06	4209.816	1.641E-06
41	4193.246	1.762E-05	4249.502	1.711E-05	4153.386	2.167E-06	4207.988	2.107E-06
42	4190.055	5.598E-06	4247.598	5.427E-06	4150.250	6.885E-07	4206.100	6.682E-07
43	4186.810	7.028E-06	4245.633	6.801E-06	4147.060	8.643E-07	4204.154	8.374E-07
44	4183.509	2.179E-06	4243.609	2.105E-06	4143.816	2.680E-07	4202.149	2.592E-07
45	4180.154	2.671E-06	4241.525	2.576E-06	4140.518	3.285E-07	4200.085	3.172E-07
46	4176.745	8.091E-07	4239.382	7.789E-07	4137.166	9.950E-08	4197.963	9.590E-08
47	4173.282	9.685E-07	4237.180	9.307E-07	4133.761	1.191E-07	4195.782	1.146E-07
48	4169.765	2.864F-07	4234.918	2.747E-07	4130.303	3.521E-08	4193.543	3.383E-08
49	4166.195	3.347E-07	4232.598	3.206E-07	4126.793	4.116E-08	4191.246	3.948E-08
50	4162.571	9.668E-08	4230.219	9.245E-08	4123.230	1.188E-08	4188.892	1.138E-08

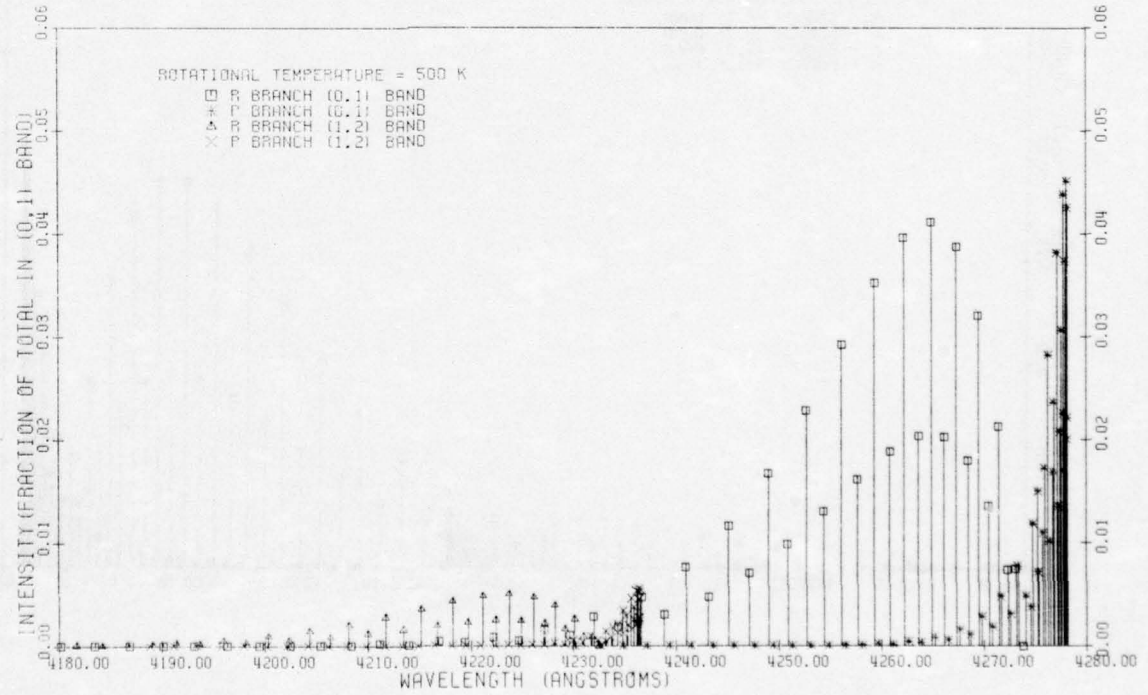


FIG. B-6 RELATIVE INTENSITIES IN THE ROTATIONAL LINES OF THE N2PLUS IN(0,1) AND (1,2) VIBRATIONAL BANDS (ROTATIONAL TEMPERATURE = 600 K)

K'	R BRANCH (0,1) EAND		P BRANCH (0,1) BAND		R BRANCH (1,2) BAND		P BRANCH (1,2) BAND	
	WAVELENGTH (A)	INTENSITY I K'R(0,1)	WAVELENGTH (A)	INTENSITY I K'P(0,1)	WAVELENGTH (A)	INTENSITY I K'R(1,2)	WAVELENGTH (A)	INTENSITY I K'P(1,2)
0	4273.936	0.000E+00	4274.631	3.162E-03	4232.507	0.000E+00	4233.181	3.891E-04
1	4273.179	6.273E-03	4275.264	1.252E-02	4231.771	7.719E-04	4233.794	1.540E-03
2	4272.360	6.159E-03	4275.834	9.209E-03	4230.974	7.579E-04	4234.346	1.133E-03
3	4271.479	1.797E-02	4276.342	2.385E-02	4230.116	2.211E-03	4234.836	2.935E-03
4	4270.535	1.154E-02	4276.788	1.434E-02	4229.197	1.420E-03	4235.265	1.764E-03
5	4269.530	2.753E-02	4277.171	3.280E-02	4228.217	3.387E-03	4235.632	4.036E-03
6	4268.463	1.561E-02	4277.492	1.806E-02	4227.176	1.921E-03	4235.938	2.222E-03
7	4267.335	3.411E-02	4277.750	3.860E-02	4226.074	4.196E-03	4236.182	4.750E-03
8	4266.144	1.807E-02	4277.946	2.011E-02	4224.911	2.224E-03	4236.364	2.475E-03
9	4264.893	3.736E-02	4278.079	4.100E-02	4223.688	4.596E-03	4236.485	5.046E-03
10	4263.579	1.888E-02	4278.149	2.049E-02	4222.404	2.323E-03	4236.544	2.522E-03
11	4262.205	3.745E-02	4278.157	4.025E-02	4221.059	4.607E-03	4236.541	4.953E-03
12	4260.769	1.823E-02	4278.103	1.944E-02	4219.655	2.243E-03	4236.477	2.392E-03
13	4259.273	3.494E-02	4277.986	3.698E-02	4218.190	4.299E-03	4236.351	4.551E-03
14	4257.715	1.648E-02	4277.806	1.733E-02	4216.665	2.027E-03	4236.163	2.133E-03
15	4256.097	3.054E-02	4277.564	3.204E-02	4215.080	3.770E-03	4235.914	3.943E-03
16	4254.418	1.404E-02	4277.259	1.461E-02	4213.436	1.728E-03	4235.603	1.798E-03
17	4252.678	2.541E-02	4276.892	2.630E-02	4211.731	3.126E-03	4235.231	3.237E-03
18	4250.878	1.134E-02	4276.463	1.169E-02	4209.968	1.395E-03	4234.797	1.439E-03
19	4249.018	2.001E-02	4275.971	2.053E-02	4208.145	2.461E-03	4234.302	2.527E-03
20	4247.098	8.714E-03	4275.416	8.910E-03	4206.262	1.072E-03	4233.745	1.096E-03
21	4245.118	1.499E-02	4274.800	1.528E-02	4204.321	1.845E-03	4233.127	1.880E-03
22	4243.079	6.378E-03	4274.121	6.476E-03	4202.321	7.846E-04	4232.447	7.971E-04
23	4240.980	1.072E-02	4273.380	1.085E-02	4200.262	1.319E-03	4231.706	1.336E-03
24	4238.821	4.457E-03	4272.576	4.497E-03	4198.144	5.482E-04	4230.904	5.536E-04
25	4236.604	7.326E-03	4271.711	7.371E-03	4195.969	9.011E-04	4230.041	9.073E-04
26	4234.327	2.977E-03	4270.784	2.987E-03	4193.735	3.662E-04	4229.117	3.677E-04
27	4231.992	4.787E-03	4269.795	4.790E-03	4191.443	5.888E-04	4228.131	5.897E-04
28	4229.598	1.903E-03	4268.743	1.900E-03	4189.093	2.341E-04	4227.085	2.338E-04
29	4227.146	2.994E-03	4267.631	2.982E-03	4186.686	3.683E-04	4225.978	3.670E-04
30	4224.635	1.169E-03	4266.456	1.157E-03	4184.221	1.433E-04	4224.810	1.425E-04
31	4222.067	1.794E-03	4265.220	1.779E-03	4181.699	2.207E-04	4223.581	2.189E-04
32	4219.441	6.838E-04	4263.923	6.762E-04	4179.121	8.411E-05	4222.292	8.324E-05
33	4216.757	1.031E-03	4262.564	1.017E-03	4176.485	1.268E-04	4220.943	1.252E-04
34	4214.016	3.848E-04	4261.144	3.788E-04	4173.793	4.732E-05	4219.533	4.664E-05
35	4211.218	5.693E-04	4259.663	5.584E-04	4171.045	6.990E-05	4218.063	6.875E-05
36	4208.363	2.077E-04	4258.121	2.036E-04	4168.240	2.554E-05	4216.533	2.507E-05
37	4205.452	3.095E-04	4256.519	2.941E-04	4165.380	3.696E-05	4214.944	3.620E-05
38	4202.484	1.076E-04	4254.855	1.051E-04	4162.464	1.323E-05	4213.294	1.293E-05
39	4199.461	1.525E-04	4253.131	1.487E-04	4159.493	1.876E-05	4211.585	1.830E-05
40	4196.381	5.351E-05	4251.347	5.207E-05	4156.467	6.581E-06	4209.816	6.410E-06
41	4193.246	7.433E-05	4249.502	7.219E-05	4153.386	9.142E-06	4207.988	8.888E-06
42	4190.055	2.555E-05	4247.598	2.477E-05	4150.250	3.142E-06	4206.100	3.050E-06
43	4186.810	3.479E-05	4245.633	3.366E-05	4147.060	4.278E-06	4204.154	4.144E-06
44	4183.509	1.172E-05	4243.609	1.132E-05	4143.816	1.441E-06	4202.149	1.394E-06
45	4180.154	1.563E-05	4241.525	1.508E-05	4140.518	1.923E-06	4200.085	1.856E-06
46	4176.745	5.164E-06	4239.382	4.971E-06	4137.166	6.351E-07	4197.963	6.121E-07
47	4173.282	6.754E-06	4237.180	6.491E-06	4133.761	8.306E-07	4195.782	7.992E-07
48	4169.765	2.186E-06	4234.918	2.097E-06	4130.303	2.688E-07	4193.543	2.582E-07
49	4166.195	2.803E-06	4232.598	2.684E-06	4126.793	3.446E-07	4191.246	3.305E-07
50	4162.571	8.894E-07	4230.219	8.506E-07	4123.230	1.093E-07	4188.892	1.047E-07

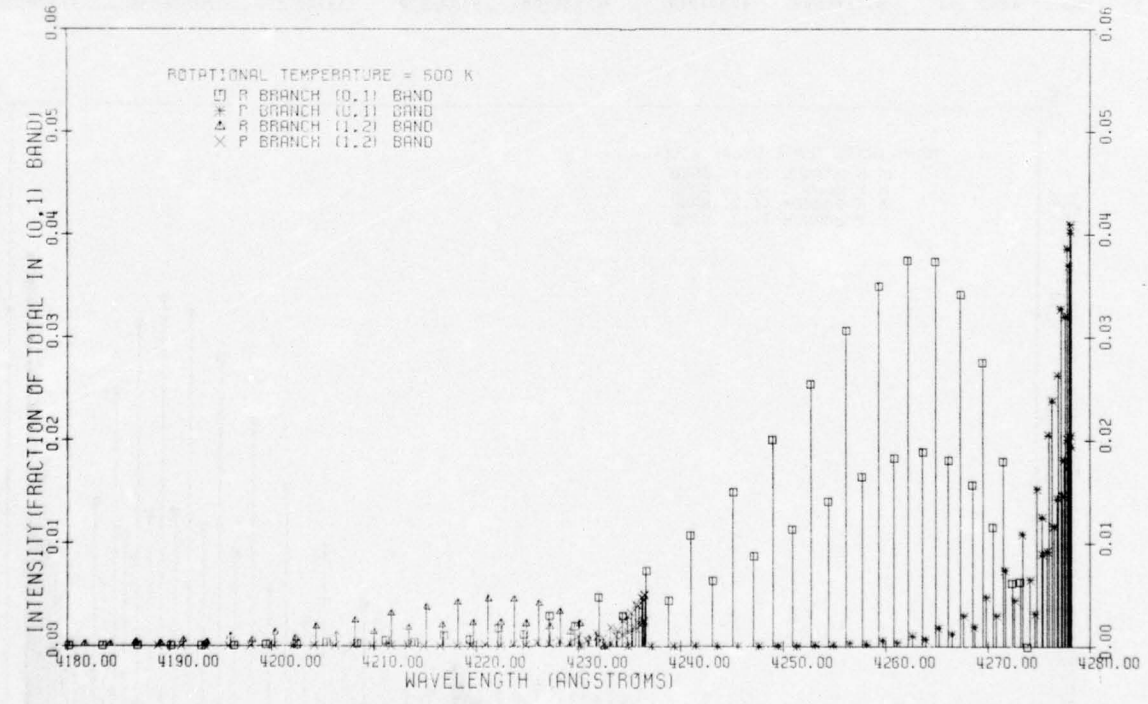


FIG. B-7 RELATIVE INTENSITIES IN THE ROTATIONAL LINES OF THE N2PLUS IN(0,1) AND (1,2) VIBRATIONAL BANDS (ROTATIONAL TEMPERATURE = 700 K)

K'	R BRANCH (0,1) BAND		P BRANCH (0,1) BAND		R BRANCH (1,2) BAND		P BRANCH (1,2) BAND	
	WAVELENGTH (A)	INTENSITY I K'R(0,1)	WAVELENGTH (A)	INTENSITY I K'P(0,1)	WAVELENGTH (A)	INTENSITY I K'R(1,2)	WAVELENGTH (A)	INTENSITY I K'P(1,2)
0	4273.936	0.00E+00	4274.631	2.715E-03	4232.507	0.000E+00	4233.181	3.341E-04
1	4273.179	5.393E-03	4275.264	1.076E-02	4231.771	6.636E-04	4233.794	1.324E-03
2	4272.360	5.309E-03	4275.834	7.938E-03	4230.974	6.533E-04	4234.346	9.768E-04
3	4271.479	1.555E-02	4276.342	2.064E-02	4230.116	1.913E-03	4234.836	2.540E-03
4	4270.535	1.004E-02	4276.788	1.248E-02	4229.197	1.235E-03	4235.265	1.535E-03
5	4269.530	2.411E-02	4277.171	2.873E-02	4228.217	2.967E-03	4235.632	3.536E-03
6	4268.463	1.378E-02	4277.492	1.595E-02	4227.176	1.696E-03	4235.938	1.963E-03
7	4267.335	3.040E-02	4277.750	3.441E-02	4226.074	3.741E-03	4236.182	4.235E-03
8	4266.144	1.628E-02	4277.946	1.812E-02	4224.911	2.004E-03	4236.364	2.230E-03
9	4264.893	3.407E-02	4278.079	3.740E-02	4223.688	4.192E-03	4236.485	4.602E-03
10	4263.579	1.746E-02	4278.149	1.894E-02	4222.404	2.148E-03	4236.544	2.331E-03
11	4262.205	3.514E-02	4278.157	3.776E-02	4221.059	4.323E-03	4236.541	4.647E-03
12	4260.769	1.739E-02	4278.103	1.853E-02	4219.655	2.139E-03	4236.477	2.281E-03
13	4259.273	3.331E-02	4277.986	3.588E-02	4218.190	4.172E-03	4236.351	4.416E-03
14	4257.715	1.630E-02	4277.806	1.713E-02	4216.665	2.005E-03	4236.163	2.109E-03
15	4256.097	3.052E-02	4277.564	3.233E-02	4215.080	3.804E-03	4235.914	3.979E-03
16	4254.418	1.448E-02	4277.255	1.506E-02	4213.436	1.781E-03	4235.603	1.854E-03
17	4252.678	2.681E-02	4276.892	2.775E-02	4211.731	3.298E-03	4235.231	3.415E-03
18	4250.878	1.226E-02	4276.463	1.263E-02	4209.968	1.508E-03	4234.797	1.555E-03
19	4249.018	2.218E-02	4275.971	2.277E-02	4208.145	2.729E-03	4234.302	2.802E-03
20	4247.098	9.926E-03	4275.416	1.014E-02	4206.262	1.221E-03	4233.745	1.249E-03
21	4245.118	1.757E-02	4274.800	1.790E-02	4204.321	2.161E-03	4233.127	2.203E-03
22	4243.079	7.659E-03	4274.121	7.817E-03	4202.321	9.469E-04	4232.447	9.621E-04
23	4240.980	1.335E-02	4273.380	1.351E-02	4200.262	1.642E-03	4231.706	1.663E-03
24	4238.821	5.731E-03	4272.576	5.783E-03	4198.144	7.049E-04	4230.904	7.118E-04
25	4236.604	9.743E-03	4271.711	9.803E-03	4195.969	1.198E-03	4230.041	1.206E-03
26	4234.327	4.100E-03	4270.784	4.114E-03	4193.735	5.044E-04	4229.117	5.065E-04
27	4231.992	6.837E-03	4269.795	6.843E-03	4191.443	8.410E-04	4228.131	8.423E-04
28	4229.598	2.824E-03	4268.743	2.818E-03	4189.093	3.472E-04	4227.085	3.469E-04
29	4227.146	4.614E-03	4267.631	4.599E-03	4186.686	5.681E-04	4225.978	5.661E-04
30	4224.635	1.871E-03	4266.456	1.859E-03	4184.221	2.302E-04	4224.810	2.288E-04
31	4222.067	3.005E-03	4265.220	2.978E-03	4181.699	3.696E-04	4223.581	3.666E-04
32	4219.441	1.195E-03	4263.923	1.182E-03	4179.121	1.470E-04	4222.292	1.455E-04
33	4216.757	1.885E-03	4262.564	1.859E-03	4176.485	2.318E-04	4220.943	2.289E-04
34	4214.016	7.363E-04	4261.144	7.249E-04	4173.793	9.055E-05	4219.533	8.924E-05
35	4211.218	1.140E-03	4259.663	1.120E-03	4171.045	1.402E-04	4218.063	1.379E-04
36	4208.363	4.373E-04	4258.121	4.288E-04	4168.240	5.379E-05	4216.533	5.279E-05
37	4205.452	6.651E-04	4256.519	6.509E-04	4165.380	8.181E-05	4214.944	8.013E-05
38	4202.484	2.506E-04	4254.855	2.448E-04	4162.464	3.083E-05	4213.294	3.014E-05
39	4199.461	3.745E-04	4253.131	3.651E-04	4159.493	4.606E-05	4211.585	4.495E-05
40	4196.381	1.386E-04	4251.347	1.349E-04	4156.467	1.705E-05	4209.816	1.661E-05
41	4193.246	2.015E-04	4249.502	1.977E-04	4153.386	2.503E-05	4207.988	2.434E-05
42	4190.055	7.406E-05	4247.598	7.180E-05	4150.250	9.108E-06	4206.100	8.840E-06
43	4186.810	1.068E-04	4245.633	1.033E-04	4147.060	1.313E-05	4204.154	1.272E-05
44	4183.509	3.819E-05	4243.609	3.690E-05	4143.816	4.697E-06	4202.149	4.543E-06
45	4180.154	5.415E-05	4241.525	5.222E-05	4140.518	6.659E-06	4200.085	6.429E-06
46	4176.745	1.902E-05	4239.382	1.831E-05	4137.166	2.340E-06	4197.963	2.255E-06
47	4173.282	2.651E-05	4237.180	2.548E-05	4133.761	3.260E-06	4195.782	3.137E-06
48	4169.765	9.157E-06	4234.918	8.785E-06	4130.303	1.126E-06	4193.543	1.081E-06
49	4166.195	1.254E-05	4232.598	1.201E-05	4126.793	1.542E-06	4191.246	1.479E-06
50	4162.571	4.257E-06	4230.219	4.071E-06	4123.230	5.235E-07	4188.892	5.013E-07

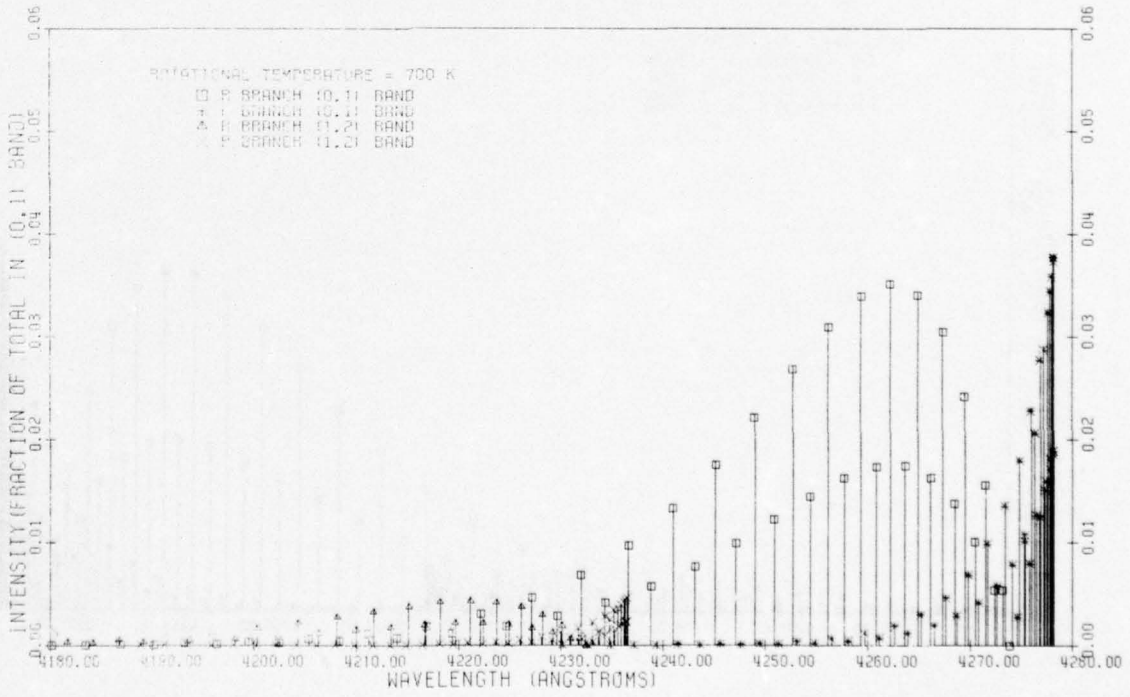
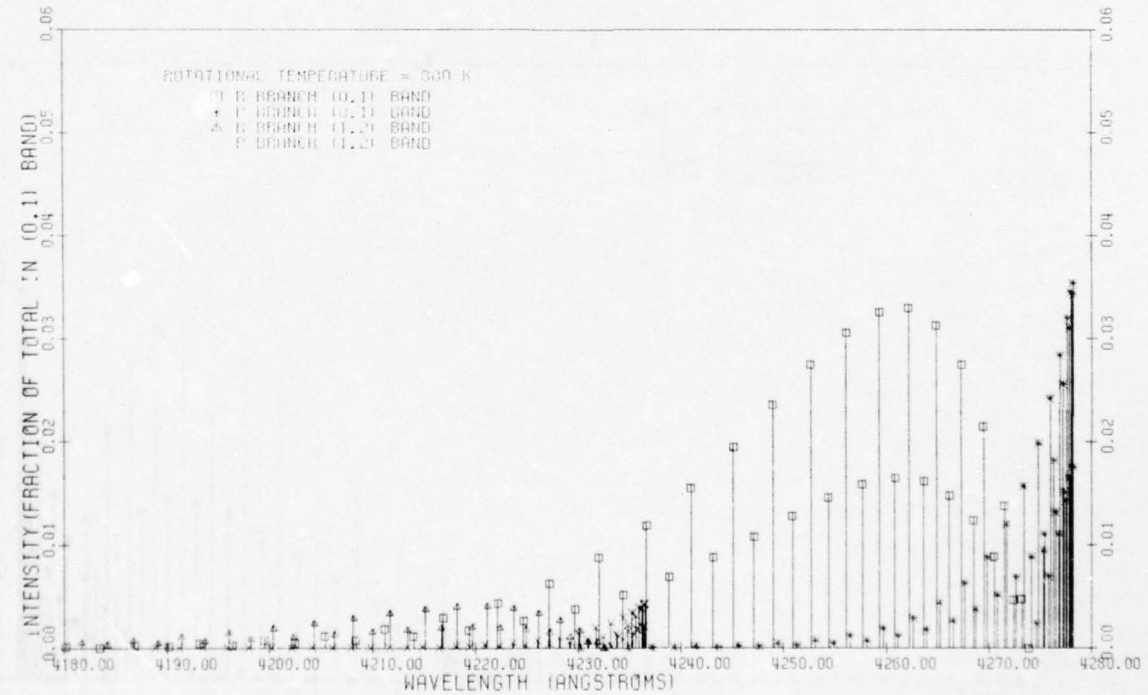


FIG. B-8 RELATIVE INTENSITIES IN THE ROTATIONAL LINES OF THE N2PLUS IN(0,1) AND (1,2) VIBRATIONAL BANDS (ROTATIONAL TEMPERATURE = 800 K)

K'	R BRANCH (0,1) BAND		P BRANCH (0,1) BAND		R BRANCH (1,2) BAND		P BRANCH (1,2) BAND	
	WAVELENGTH (A)	INTENSITY I K'R(0,1)	WAVELENGTH (A)	INTENSITY I K'P(0,1)	WAVELENGTH (A)	INTENSITY I K'R(1,2)	WAVELENGTH (A)	INTENSITY I K'P(1,2)
0	4273.936	0.000E+00	4274.631	2.378E-03	4232.507	0.000E+00	4233.181	2.926E-04
1	4273.179	4.729E-03	4275.264	9.441E-03	4231.771	5.819E-04	4233.794	1.161E-03
2	4272.360	4.665E-03	4275.834	6.975E-03	4230.974	5.740E-04	4234.346	8.583E-04
3	4271.479	1.370E-02	4276.342	1.819E-02	4230.116	1.686E-03	4234.836	2.239E-03
4	4270.535	8.887E-03	4276.788	1.104E-02	4229.197	1.093E-03	4235.265	1.359E-03
5	4269.530	2.145E-02	4277.171	2.556E-02	4228.217	2.639E-03	4235.632	3.145E-03
6	4268.463	1.213E-02	4277.492	1.427E-02	4227.176	1.518E-03	4235.938	1.756E-03
7	4267.335	2.740E-02	4277.750	3.101E-02	4226.074	3.371E-03	4236.182	3.816E-03
8	4266.144	1.480E-02	4277.946	1.646E-02	4224.911	1.820E-03	4236.364	2.026E-03
9	4264.893	3.124E-02	4278.079	3.429E-02	4223.688	3.844E-03	4236.485	4.220E-03
10	4263.579	1.617E-02	4278.149	1.754E-02	4222.404	1.989E-03	4236.544	2.159E-03
11	4262.205	3.291E-02	4278.157	3.537E-02	4221.059	4.049E-03	4236.541	4.352E-03
12	4260.769	1.648E-02	4278.103	1.757E-02	4219.655	2.028E-03	4236.477	2.162E-03
13	4259.273	3.257E-02	4277.986	3.447E-02	4218.190	4.007E-03	4236.351	4.242E-03
14	4257.715	1.588E-02	4277.806	1.669E-02	4216.665	1.953E-03	4236.163	2.055E-03
15	4256.097	3.059E-02	4277.564	3.198E-02	4215.080	3.763E-03	4235.914	3.936E-03
16	4254.418	1.456E-02	4277.259	1.514E-02	4213.436	1.791E-03	4235.603	1.863E-03
17	4252.678	2.742E-02	4276.892	2.838E-02	4211.731	3.373E-03	4235.231	3.493E-03
18	4250.878	1.277E-02	4276.463	1.316E-02	4209.968	1.571E-03	4234.797	1.620E-03
19	4249.018	2.356E-02	4275.971	2.418E-02	4208.145	2.898E-03	4234.302	2.976E-03
20	4247.098	1.075E-02	4275.416	1.099E-02	4206.262	1.323E-03	4233.745	1.353E-03
21	4245.118	1.945E-02	4274.800	1.981E-02	4204.321	2.392E-03	4233.127	2.439E-03
22	4243.079	8.712E-03	4274.121	8.847E-03	4202.321	1.071E-03	4232.447	1.088E-03
23	4240.980	1.546E-02	4273.380	1.565E-02	4200.262	1.902E-03	4231.706	1.926E-03
24	4238.821	6.802E-03	4272.576	6.864E-03	4198.144	8.367E-04	4230.904	8.449E-04
25	4236.604	1.186E-02	4271.711	1.193E-02	4195.969	1.458E-03	4230.041	1.469E-03
26	4234.327	5.125E-03	4270.784	5.142E-03	4193.735	6.304E-04	4229.117	6.330E-04
27	4231.992	8.782E-03	4269.795	8.789E-03	4191.443	1.080E-03	4228.131	1.081E-03
28	4229.598	3.730E-03	4268.743	3.724E-03	4189.093	4.588E-04	4227.085	4.583E-04
29	4227.146	6.285E-03	4267.631	6.258E-03	4186.686	7.730E-04	4225.978	7.704E-04
30	4224.635	2.625E-03	4266.456	2.608E-03	4184.221	3.229E-04	4224.810	3.210E-04
31	4222.067	4.350E-03	4265.220	4.311E-03	4181.699	5.351E-04	4223.581	5.307E-04
32	4219.441	1.787E-03	4263.923	1.767E-03	4179.121	2.198E-04	4222.292	2.176E-04
33	4216.757	2.914E-03	4262.564	2.875E-03	4176.485	3.584E-04	4220.943	3.539E-04
34	4214.016	1.179E-03	4261.144	1.160E-03	4173.793	1.449E-04	4219.533	1.428E-04
35	4211.218	1.890E-03	4259.663	1.857E-03	4171.045	2.324E-04	4218.063	2.286E-04
36	4208.363	7.520E-04	4258.121	7.374E-04	4168.240	9.249E-05	4216.533	9.078E-05
37	4205.452	1.187E-03	4256.519	1.162E-03	4165.380	1.460E-04	4214.944	1.430E-04
38	4202.484	4.650E-04	4254.855	4.542E-04	4162.464	5.719E-05	4213.294	5.592E-05
39	4199.461	7.228E-04	4253.131	7.046E-04	4159.493	8.890E-05	4211.585	8.675E-05
40	4196.381	2.787E-04	4251.347	2.711E-04	4156.467	3.427E-05	4209.816	3.338E-05
41	4193.246	4.265E-04	4249.502	4.142E-04	4153.386	5.245E-05	4207.988	5.099E-05
42	4190.055	1.619E-04	4247.598	1.569E-04	4150.250	1.991E-05	4206.100	1.932E-05
43	4186.810	2.439E-04	4245.633	2.361E-04	4147.060	3.000E-05	4204.154	2.906E-05
44	4183.509	9.120E-05	4243.609	8.810E-05	4143.816	1.121E-05	4202.149	1.084E-05
45	4180.154	1.353E-04	4241.525	1.305E-04	4140.518	1.664E-05	4200.085	1.606E-05
46	4176.745	4.982E-05	4239.382	4.796E-05	4137.166	6.126E-06	4197.963	5.905E-06
47	4173.282	7.280E-05	4237.180	6.997E-05	4133.761	8.953E-06	4195.782	8.615E-06
48	4169.765	2.639E-05	4234.918	2.532E-05	4130.303	3.246E-06	4193.543	3.118E-06
49	4166.195	3.799E-05	4232.598	3.639E-05	4126.793	4.672E-06	4191.246	4.481E-06
50	4162.571	1.356E-05	4230.219	1.297E-05	4123.230	1.668E-06	4188.892	1.597E-06



APPENDIX C: SOURCES OF ERRORS FOR EBFP DENSITY AND TEMPERATURE MEASUREMENTS

A variety of factors are involved which determine the precision and accuracy of the measurements made using the EBFP; not all of these can be quantified but an attempt has been made to give numerical assessments where possible.

(1) Electron Beam Accelerating Voltage

The excitation cross section varies approximately as $E_e^{-1} \ell n\, E_e$, where E_e, the beam accelerating voltage is above a few hundred eV. The relative change in the optical radiation intensity is therefore nearly proportional to dE_e/E_e. Thus to a first approximation, changes in the accelerating potential will directly affect the measured density.

The 'worst case' line and load regulation conditions for the DC·DC converter result in ± 2.5% variations in the final beam voltage. In flight, it is estimated that the voltage fluctuations do not exceed ± 1.5%.

(2) Beam Current

This parameter should ideally be measured at the probe region; this is feasible if intermittent measurements are made using a flag at that position. If the beam current is monitored at the gun exit and back stop locations, then for altitudes above about 100 km the current at these stations will differ by less than 2%. At lower altitudes it becomes increasingly difficult to specify the actual current passing through the observation region, especially in situations where local density enhancements exist due to shock conditions.

(3) Gas Density Measurements

Curves similar to those in Fig. 38 are obtained using the static gas calibration procedure. The ordinate values on these curves require to be merely precise and repeatable for valid interpretation of the density in the probe region. It has been observed during calibrations that the accumulative effect of all error sources reduces the repeatability for an EBFP reading at a particular gas pressure to about ± 10%. Repeated measurement and data smoothing reduce the uncertainty in the final calibration curve to about ± 5%.

The accurate measurement of the gas pressure in the probe region during calibration depends on the following factors.

(a) Pressure Sensing Devices

The accuracy of the pressure measurement depends on the accuracy of the pressure sensing gauge and a knowledge of pressure gradients, if they exist, within the calibration chamber. An effort is made during calibrations to minimize the latter effect.

An MKS Baratron capacitance manometer was used for the pressure range above 1 mtorr. This instrument has a quoted accuracy of ± 1% at 1 mtorr and has been found to have a few percent accuracy at 0.1 mtorr. A Balzers IMR3 triode type ionization gauge was calibrated against the Baratron for the pressure range 10^{-5} to 10^{-2} torr for N_2, He, A, O_2, CO_2 and air and the best fitting linear

curves were then extrapolated extending the IMR3 calibration to lower pressures. The IMR3 has a repeatability of ± 1% over the range 10^{-2} to 10^{-8} torr. Introduction of the test gas was made via a controlled leak valve situated directly over the diffusion pump cold trap in the case of the 170 ℓ/s pump and approximately 2 metres from the EBFP using the 10,000 ℓ/s pump (pumping was continuous during all phases of the calibration). The pressure gauges were positioned approximately 15 cm from the EBFP probe region; the IMR3 gauge was not operated during the EBFP measurements in order to avoid light leakages from the gauge into the EBFP optics.

(b) Gas Purity in the Probe Region

Research grade gases were employed for all calibration tests and EBFP measurements were recorded only when the static gas pressure exceeded 10 times the base pressure (obtained with the instrument in the vacuum chamber). Perhaps the biggest source of gas contamination present during calibration at low pressures originated from the electron gun and magnetic lens assembly. Evidence that contamination existed is indicated by the linearity change with pumping speed shown in Fig. 38.

A transient pumping test simulating the rocket flight pressure profile would permit a direct comparison to be made between the calibrations obtained using the procedures outlined in Sec. 5 and the density monitored by the EBFP during rapid pumpdown. Unfortunately, pumping facilities for this test are not readily available.

4. Rotational and Vibrational Temperature Measurements

(a) Gas Temperature During Calibration

The temperature of the test gas was in all cases assumed to be that of the vacuum vessel, the temperature of the latter was monitored to ± 1 K. Actual operating times for the EBFP were short during the static gas calibrations, providing ample time for the apparatus to reach thermal equilibrium with the vacuum chamber.

(b) Spectral Response Functions Determined by Optical Calibrations

It has been pointed out in Sec. 4.3 that the static gas calibration procedure cannot be applied in calibrating the EBFP for reactive gases such as atomic oxygen. Similar restraints apply when ascertaining the sensitivity of EBFP channels assigned for rotational and vibrational temperature measurements. If the optical procedure described in Sec. 4.3 is carried out then an error of approximately ± 5% is involved in the determination of an individual spectral response function and this increases to ± 10% when a ratio is taken between the signals from two channels.

(c) Interference Filters

The biggest single source of error associated with temperature measurements made with the EBFP can be attributed to the interference filters. Stable mounting procedures prevent accidental tilt of the filters during launch, eliminating wavelength shifts due to mechanical movement. The optical calibration procedure employed permits the relative spectral sensitivity of

an EBFP channel to be specified to ± 2% for values down to 1% of the peak sensitivity. The accumulated wavelength error is estimated at ± 0.1 Å. The filter transmission is also a function of temperature, the peak wavelength shift, depending somewhat on the filter construction, being typically 0.1 Å/K for narrow band filters. The effect of filter wavelength shifts on the intensity ratio vs temperature curve has been examined numerically and some results are presented in Fig. C-1. For a wavelength shift of ± 0.2 Å (typical payload temperature variation) the error in temperature introduced in the EBFP-RTA calibration curve (for Ω = 1.1 sr) varies from ± 5 K at 250 K to ± 15 K at 800 K.

(d) Reflected Molecules

This effect has been discussed in Sec. 2.3 for the case of rotational temperature measurements. Typically, the light contribution from reflected molecules affects the theoretically predicted calibration curve as shown in Fig. 6. The extent of this effect on the intensity ratio in the two channels varies from no effect at 300 K, to -10% at 800 K ambient temperature. The errors introduced in the intensity ratio due to the uncertainties in the solid angle Ω, the speed ratio S and the angle of attack α are seen in Fig. 6.

5. Photometric Linearity and Sensitivity

Nonlinearities in the photometer system are taken into account using the static gas calibration procedure. The compensation of any subsequent change in the sensitivity of the optical system is made using the calibration lamp. A discussion on the accuracy and temperature dependence of the photomultiplier amplifier and logging unit is contained in Appendix D of this report.

6. Summary on Errors

From the foregoing discussion it may be concluded that a reduced flight record could be assigned the following errors:

Concentration Measurement Errors with EBFP (at ~ 90 km Altitude)

Beam Voltage (in flight)	± 1.5%
Beam Current (in flight)	± 1%
Sensitivity Corrections (in flight)	± 2%
Calibration Pressure	± 1%
Calibration Accuracy (smoothed)	± 5%*

Temperature Measurement Errors with EBFP-RTA (at ~ 110 km Altitude)

Sensitivity Corrections (in flight)	± 4%
Interference Filter Changes	± 2%
Reflected Molecules (refer to 4(d) above)	
Spectral Response Functions Ratio from Optical Calibration	± 10%

*For atomic oxygen an additional error bar of about +25% - 10% must be added as described in Ref. 5.

The above table will apply for EBFP systems that employ facilities for simultaneously monitoring the optical emissions required for the filter ratios.

Many of the errors described can be reduced using better regulation on power supplies, improved monitoring circuits and temperature control for the interference filters; the uncertainties that remain are then those affecting almost all upper atmospheric instruments.

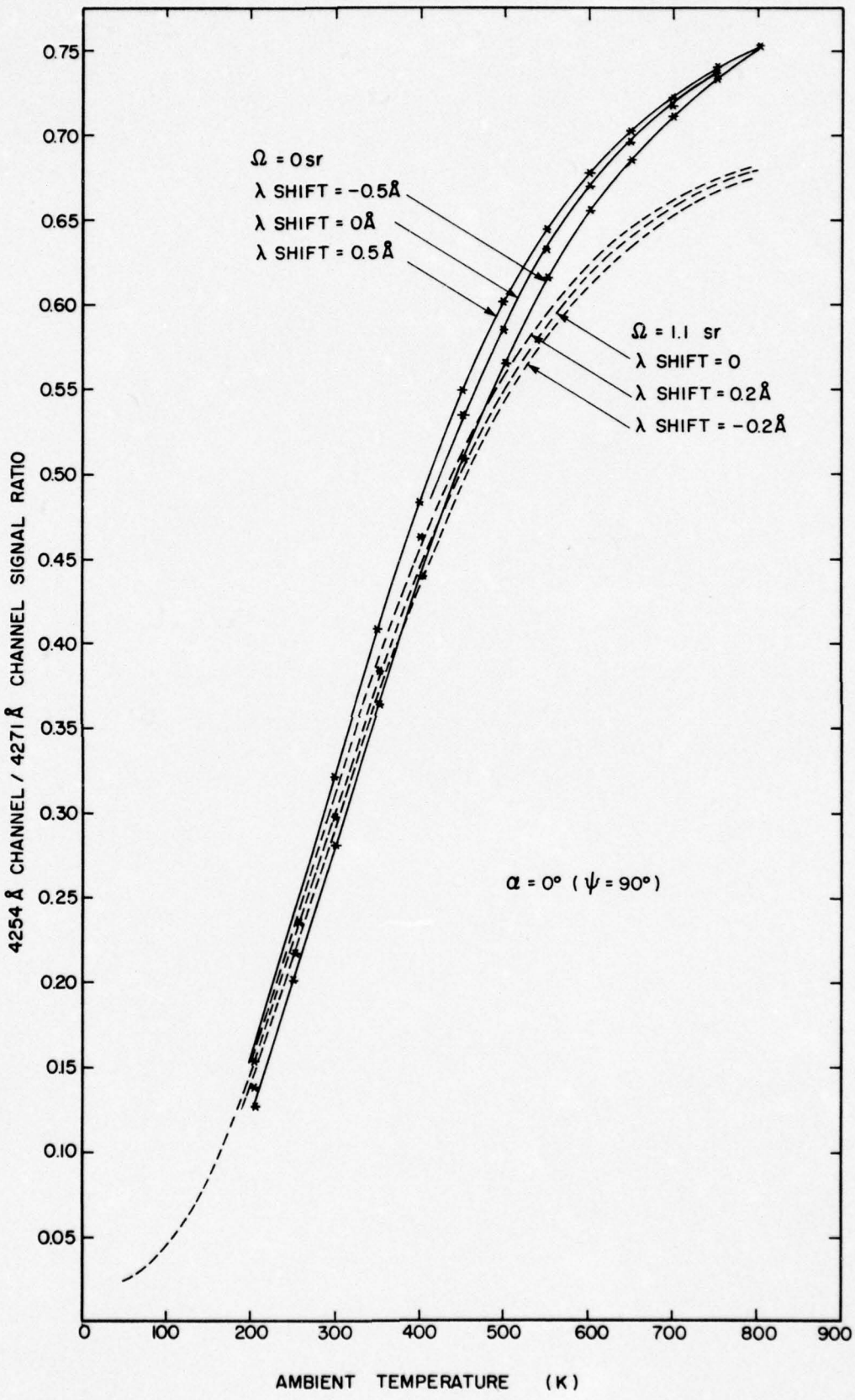


FIG. C-1 EFFECTS OF INTERFERENCE FILTER WAVELENGTH SHIFT ON EBFP-RTA CALIBRATION

APPENDIX D: ELECTRONIC SUBSYSTEMS FOR THE EBFP

Various electronic subsystems are involved when the EBFP is integrated into a rocket payload; not all of these are germane to this report and the descriptions that follow apply to those electronic devices required specifically for operation of the EBFP. System schematics for the continuous and modulated EBFP versions shown in Figs. D-1 and D-2, respectively, indicate the operational functions of the various electronic control elements. The first four items in the following descriptions are common to both configurations.

1. Electron Gun Cathode Emission Regulator

The electron beam current is accurately monitored at the stations shown in Figs. D-1 and D-2 thus obviating the need for any accurate emission control on the electron gun. Indeed, because of the large variations of the collected beam current due to electron scattering shown in Fig. 3 it is impractical to keep the emission constant by feedback from the beam current monitors. The controller described here maintains the high voltage current supplied to the electron gun at a fairly constant level, thus reducing emission current variations due to fluctuations in the cathode filament battery voltage and aging effects in the filament itself.

The emission regulator circuit is shown in Fig. D-3; all elements inside the dashed line are biased at -2500V and must be protected for high voltage breakdown under vacuum conditions as described in Sec. 3.2. Because the regulator and the filament battery float at -2500V activation of the circuit is performed through an optical isolator. Light produced by 28 volt lamps A1, A2, falling on the photocell PC1 decreases its resistance to 50 ohms causing the transistor Q1 to activate relay K1. Diodes D2, D3 and D4 are now forward biased through R4 by the regulator battery to produce a reference of 2.7 volts. This reference voltage provides base drive to Q2 through R5, R6, D5 and D6, turning on the output Darlington Q3, Q4 and supplying heating current to the filament.

Regulation is accomplished by feeding the emission current through reference resistor R5. This voltage drop which subtracts from the reference voltage controls the base drive to Q2. Besides serving as a reference, diodes D2, D3 and D4 in conjunction with D5, D6 and D7 protect the regulator transistors in the event of gun arcing at high pressures. During an arc, the resistance between the filament and the gun anode decreases to an extremely low value. The regulator now no longer floats but sees 2500 volts from the junction of R5 and R6 to ground. Under these conditions diodes D2 through D6 assume the reverse blocking mode forcing the H.T. converter energy to be dissipated in R4 and R5. Any spikes appearing at the base of Q2 due to the capacity of D5 and D6 are limited by D7 to protect the base emitter junction of Q2. Q5 and R7 limit the regulator output current to 12 amps as a filament protection measure.

Photo cell PC2 and a 6-volt lamp A3 constitute a filament power monitor. Under normal operating conditions the filament drops approximately 3 volts. Lamp A3 which is in parallel with the filament illuminates photo cell PC2 and the resistance of the latter serves as a filament current monitor.

PRECEDING PAGE BLANK-NOT FILMED

2. Photomultiplier H.T. Supply

The EMI 9781 photomultiplier tubes have typical gains of 10^7 and 10^4 with applied voltages of 900V and 350V, respectively. In the high gain configuration it can be seen from Fig. 21 that the anode current for the N_2 4270Å channel may vary from 10^{-4} to 10^{-11}A over the altitude range from 75 to 250 km.

A dynode current of 1 mA at 900V has been selected to minimize heating of the tube; this current is inadequate to permit linear operation of the tube over the maximum dynamic range of photocurrents encountered during a rocket flight. Linear photocurrent operation is maintained by automatic range switching of the photomultiplier H.T. voltage from 900V to 350V if the anode current exceeds 10^{-7}A.

The photomultiplier H.T. supply consists of a Venus DC-DC converter model K15, powered by a precision regulator. The DC transformation gain of the K15 is approximately 40 db thus the precision regulator formed by A1, Q1 and the associated components shown in Fig. D-4 must provide 9 volts to the K15 input. The L.C. filter formed by the 150 μH inductor and the 4.7 μF capacitor reduce switching spikes on the input power lines to less than 20 mA. Output ripple is less than 0.1% and the output voltage changes 1.2% from 0°C to 50°C. Line regulation is 0.1% for an input voltage change from 24 to 30 volts. Range switching of the output voltage is achieved by using the range signal line; when operating at a fixed 900V level the range signal line is connected to V_{in}.

3. Focus Coil and Calibration Lamp Regulators

The focus coil and calibration lamp regulators are current sources differing only in output and precision. It is evident from Eq. 3.4 that the effective focal length of the magnetic lens is not strongly dependent on the focus coil current, and a few percent current stability is adequate. The calibration lamp regulation is far more critical, 0.1% regulation is required at a lamp current of 170 mA to achieve 1% stability in the photomultiplier output.

Figure D-5 shows the circuit common to both regulators. Preregulator Q1 provides a constant current to the base of the output Darlington Q2, Q3 and the collector of the reference amplifier Q4. The resulting voltage drop of the output current IQ3 across R1 is compared to the reference voltage of Q4 which provides the feedback to the preregulator Q1. The regulated output current is given by $[V_{ref}Q4/R1]$; V_{ref} is nominally 6.8 volts.

For the calibration lamp regulator, R1 is a precision wire-wound 40Ω resistor with a temperature coefficient of 30 ppm/°C. A wire-wound resistor with standard temperature specifications is used for the focus coil regulator.

The output current of the calibration lamp regulator varies 0.3% from 0° to 50°C, an acceptable value since the payload temperature is maintained to ± 5°C within this range.

4. Logarithmic Conversion of the EBFP Photocurrents

Because of the large dynamic range of photomultiplier currents (10^{-4} to 10^{-11}A) encountered in a typical rocket flight, some form of signal compression is required to enable data transmission to take place with minimum loss of accuracy. Range switching of the linear form of the input signal or direct logging of the signal are useful methods for data compression, although only the latter has been applied to the EBFP.

Temperature compensated logarithmic transducers are available from commercial sources which provide logged (base 10) outputs to 1% accuracy for input currents ranging from 1 mA to 1 nA. These devices in the transdiode mode retain their true logarithmic characteristics down to input levels of 10^{-12}A and thermostatic control of the logging element has been used in some versions of the EBFP to ensure repeatability at low current levels. The basic transdiode log circuit is shown in Fig. D-6a. The output voltage is the emitter base voltage V_{EB} of Q1. At 27°C this output is represented by

$$V_{out} \approx \left[0.06 \log_{10} \frac{I_{in}}{\alpha I_{ES}} \right]$$

where I_{ES} is the emitter saturation current for the common base mode and 0.06 is the log scaler of 60 mV per decade. The term I_{ES} for selected transistors is typically 10^{-13}A. The voltage current relationship for the base emitter junction of Q1 is logarithmic from 10^{-12} to 10^{-3}A and since the collector current $I_C = \alpha I_E$ in the common base mode, the input current I_{in} is essentially equal to the emitter base current of Q1. Resistor R_E is necessary to avoid loading of amplifier A_1 at high input currents.

The transistor Q_1 acts as a variable feedback resistor with a resistance related to the input current I_{in} by the expression

$$R_{Q1} = \frac{1}{40\ I_{in}}$$

and the time constant τ for the logging circuit is then given by

$$\tau \simeq R_{Q1} \cdot C_F$$

Thus with an input current of 10^{-9}A and a value of 10 pF for the feedback capacitor C_F (about the smallest practicable value permissible for amplifier stability), the maximum operating frequency is approximately $1/(2\pi\tau)$ or 635 Hz.

There are two different temperature effects for the log circuit of Fig. D-6a. The first is the term I_{ES}, which doubles every 10°C and the second is the log scaler, 60 mV/decade at 27°C, which changes linearly with temperature at .3%/°C. A very simple and effective method of reducing these errors is to place the log transistor Q1 in an oven at an arbitrary temperature above ambient. The thermostat should have a low hysteresis to ensure as near a constant temperature as possible. The disadvantages of this system is the time required to reach operational temperature and the bulk introduced by the heater.

Another method of removing the temperature dependent terms is to employ the compensation technique illustrated in Fig. D-6b. Here the error term I_{ES} is reduced to a fixed offset by the generation of a log ratio between I_{in} and a reference current I_{ref}. A close match of Q1 and Q2 is required for this technique. The log scaler error of .3%/°C is removed by voltage divider RTC-RG whose temperature coefficient is equal and opposite to that of the log scaler. The matched transistors Q1 and Q2 together with the voltage divider RTC-RG are available in packaged log modules.

Caution must be exercised in interpreting the logged outputs of rapidly decreasing signals at low current levels since the slewing rate is always determined by the circuit bandwidth at the final current level. The unfiltered statistical current fluctuations associated with low photon count rates (10^4/s corresponds to about 10^{-9}A anode signal) for the EBFP have frequency components greater than the signal bandwidth of a logging amplifier operating at that current level. Thus at low current levels the output signals from the log amplifier will, in general, be too high unless the photomultiplier output is prefiltered to reduce the frequency requirements of the logging unit.

Maximum frequency response for the logging amplifier is usually retained for rocket flights and statistical variations will be present in the telemetry record at the low current levels. It should be noted that arithmetic averaging of a logged signal produces the geometric mean of the true input signal; if uncorrected this introduces an error of 5.3%.

5. Signal Handling for the DC Beam EBFP

The purpose of the EBFP signal handling electronics is to present the photomultiplier current of 10^{-5} to 10^{-10}A on a 0 to +5 volt scale. The circuit shown in Fig. D-7 consists of two operational amplifiers and a Philbrick log module connected as a standard log ratio circuit, followed by a unity gain inverter. The reference current into amplifier A2 is adjusted by the 200Ω potentiometer to equal the maximum current to be measured, i.e., 10^{-5}A. The log module scaling factor is 1 volt per decade, so the circuit output voltage varies from 0 volts to 10^{-5}A to +5 volts at 10^{-10}A.

To ensure adequate time response at the lowest current of interest, i.e., 10^{-10}A, the feedback capacitance on amplifier A1 was reduced to 10 pF. The log element resistance at 10^{-10}A is $1/(40I) = 250 \times 10^6\Omega$; assuming 7 time constants for 1% accuracy, the time required to slew down to 10^{-10}A is approximately 17.5 ms.

Temperature performance of the circuit is illustrated in Fig. D-8. The bias current of amplifier A1 is the primary source of error at low currents. The bias current is 10^{-12}A at 25°C, so at 50°C this bias current would be approximately 6×10^{-12}A, resulting in an error of 6% when the circuit measures an input current of 10^{-10}A.

6. Filter Disc Drive Circuit for DC Beam EBFP

The filter disc drive circuit shown in Fig. D-9 provides power to the motor which turns the filter selection disc shown in Fig. D-1. The circuit is a conventional adjustable regulator using an operational amplifier

A1 as the error amplifier. Filter Network L_1 C_2 reduces the motor spikes to < 20 mA on the 28 volt power line. The available current from the regulator is limited at 1.2A by transistor Q1, and potentiometer R1 provides for adjustment of the motor speed.

7. DC Beam Current Monitor

Electrons striking the backstop shown in Fig. D-1 are returned to the rocket ground potential via a 500Ω resistor as indicated in Fig. D-10. The voltage drop across this resistor is then monitored by the inverting amplifier A1. The output is scaled to give 0.5V per mA of beam current and is limited to -0.6V and +5.6V for telemetry purposes.

8. Electron Beam Modulating System

The electron beam in the AC Beam version of the EBFP, Fig. D-2, is modulated to provide synchronous detection capabilities for the optical signals and to enable current measurements on the beam to be made before the electrons reach the observation region. Two magnetic deflection coils (Fig. D-2) are driven in parallel with a 250 Hz square wave with a total current of 0.6A; ferrite cores are used resulting in a flux density of ~ 10^{-2} webers/m^2 at the cathode. The modulated beam has a current rise time of ~ 250 μs and a fall time of ~ 50 μs at pressures up to 1 equiv. mtorr in air.

The details of the coil switching circuit are given in Fig. D-11. The operational amplifier A1 connected as an astable multi-vibrator provides a voltage square wave at a frequency of 250 Hz. The current source A is gated on during negative excursions of the voltage square wave, providing current to the deflection coils, current source B being gated on during positive excursions of the voltage square wave, or 180° out of phase with respect to current source A. This reduces the transients on the current source power line to a time period equal to the sum of the rise and fall times of the two current sources, resulting in a smaller line filter L1C2, while maintaining power line ripple at less than 20 mA. Power is supplied to the current sources by a gate signal which turns on Q1, Q2 via Q3.

9. Current Monitors for the Modulated Electron Beam

The beam current in the modulated electron beam system is monitored at the two locations indicated in Fig. D-2. A voltage proportional to the backstop current is transmitted through the telemetry system using a bandwidth adequate to follow the 250 Hz signal. An amplifying circuit similar to that used for the DC beam and shown in Fig. D-10 is employed for this purpose.

The electron beam current is also monitored after leaving the gun, as indicated in Fig. D-2. For this measurement the electron beam serves as the primary of a transformer which has its secondary windings on a ferrite toroid through which the beam passes at the gun exit orifice. The ferrite toroid winding is designated L in the circuit diagram, Fig. D-12, and provides an output voltage of ~ 400 μV peak to peak into a 10Ω load for a peak beam current of 10 mA. Amplifiers A1 and A2 provide 80 dB of amplification to the coil signal, and the 1kΩ resistor and 0.1 μF capacitor at the output of A2 constitute a filter to reduce amplifier noise. The amplified signal is then full wave rectified and filtered by the precision rectifier A3, A4.

10. Signal Processing Techniques for the Modulated Electron Beam System

Synchronous detection can be employed to reduce the effect of spurious light signals when using a modulated electron beam. The statistical limitations present when using this method have been discussed in Sec. 4.4.

The circuit diagrams outlining the procedure for handling the photomultiplier anode currents are shown in Figs. D-13 and D-14. In Fig. D-13 the input signal is first divided into its AC and DC components, the DC signal is then amplified by A_1 primarily for use when the calibration lamp is in operation. The DC output also serves to provide a measure of the background illumination level under normal operating conditions. The output from the AC follower A_2 in Fig. D-13 is used for the synchronous detection circuitry shown in Fig. D-14. For explanation purposes this latter circuit has been separated into five sections, each of which is described below.

(a) Pre-filter

The pre-filter formed by A_1 in Fig. D-14 increases the rejection capabilities of the synchronous detector by attenuating low frequency variations which have passed through the AC coupled follower. All frequencies under 10 Hz are attenuated 40 db/decade by A1, a multiple feedback high pass filter; A2 isolates the filter from the synchronous detector and also provides a gain of two to the signal.

(b) Sync. Phase Shift Circuit

The sync. phase shift circuit ensures that the sync. signal and the modulated signal are exactly in phase at the detector switches Q_1 and Q_2. The sync. signal, derived from the astable multi-vibrator of the beam coil deflection circuit, is conditioned to $\pm$ 5 volts by limiter A7. Amplifier A8 delays the zero crossings of the square wave from A7 by increasing the rise and fall times. The output of A9, a zero crossing detector, is therefore a square wave shifted in phase with respect to the sync. input.

(c) Synchronous Detector

The synchronous detector provides full wave rectification for the modulated signal which is in phase with the sync. signal from amplifier A9. A 180° phase shift is required between the two correctly modulated signals presented to the mos/fet switches Q1 and Q2 and this is accomplished using the appropriate outputs on A3 and A4. Switching of the mos/fets by the sync. network, composed of A7, A8 and A9, results in positive rectification of correctly phased signals. An integrating filter, consisting of the 8.2 μF capacitor and the 10kΩ resistor which precede A5 and A6, is employed to average the out of phase components and prevent large signal excursions at the inputs of A5 and A6.

A measure of the background rejection capabilities at the output of the 82 ms integration network may be seen by referring to Fig. D-15 which shows the attenuation curve for a sine-wave source. The curve scales with the integrating time constant, i.e., a ten times increase of the integration

time will produce a constant 20 db increase in attenuation over the complete frequency range except in the immediate vicinity of the fundamental and odd harmonics.

(d) Logarithmic Output Circuit

The output of the synchronous detector circuit is logged at 1 volt per decade for signal compression purposes by amplifiers A5 and A6 of Fig. D-14 in conjunction with a temperature compensated Teledyne Philbrick log module 4357. Since the synchronous detector output is a voltage varying from 1 mV to 10V corresponding to photomultiplier tube anode currents of 10^{-10} to 10^{-6}A, improved time response from the log output circuit becomes practical. This is accomplished by designing for a minimum summing point current into amplifier A5 of 1×10^{-8}A referred to the photomultiplier tube anode current of 10^{-10}A, resulting in a time constant of 0.125 ms (compared with the synchronous detector output of 82 ms). The input offset voltage of amplifier A5 produces an error of 2.5% at 50°C at a P.M. tube input current of 10^{-10}A.

(e) Range Switching Level Detector

The dynamic range of input signals which can be handled is increased by automatic switching of the photomultiplier H.T. voltage as described earlier in this section; this provides an additional gain factor of 10^3, thus expanding the total signal handling capability to cover from 10^{-3} to 10^{-10}A. The log output which is used as the range switch sensing point is integrated by amplifier A10 in Fig. D-14 to ensure that no switching occurs on transients. Amplifier A11 is connected as a Schmitt trigger with reference levels of 1 or 4.1 volts, corresponding to 10^{-7} and 10^{-10}A, respectively. Amplifier A11 changes its output state whenever the P.M. modulated signal exceeds 1.1×10^{-7}A or decreases below 9×10^{-11}A. The output signal from the level detector controls the photomultiplier H.T. supply.

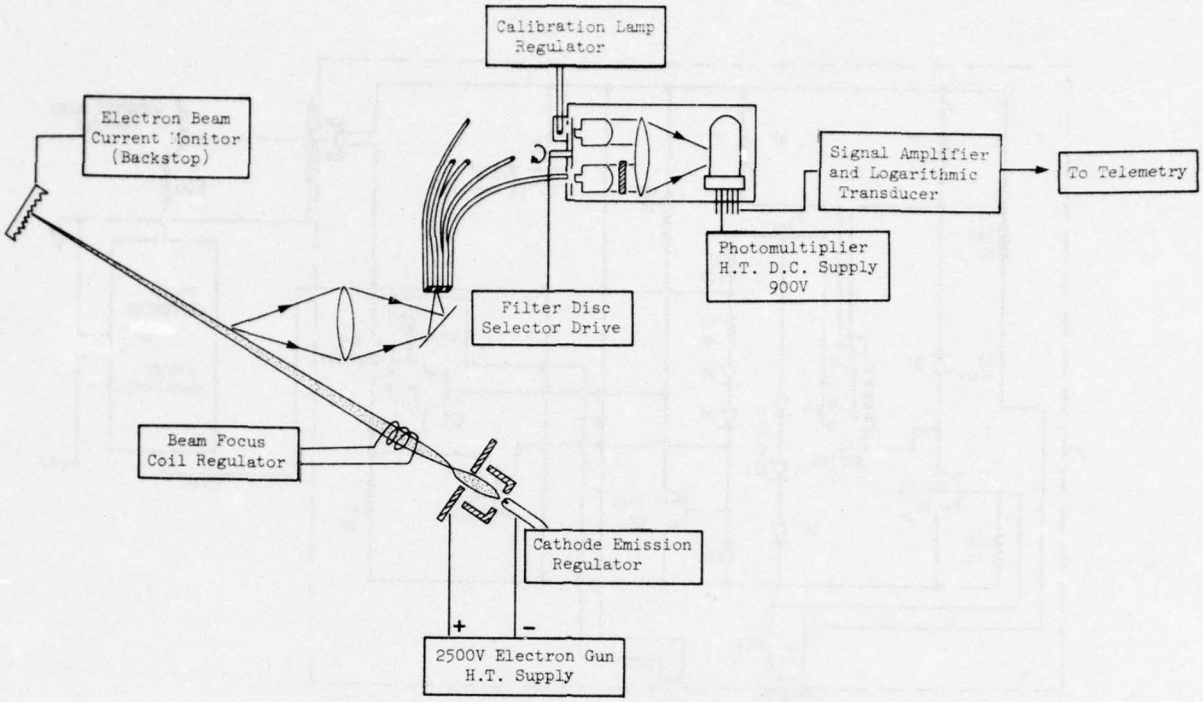


FIG. D-1 D.C. ELECTRON BEAM SYSTEM

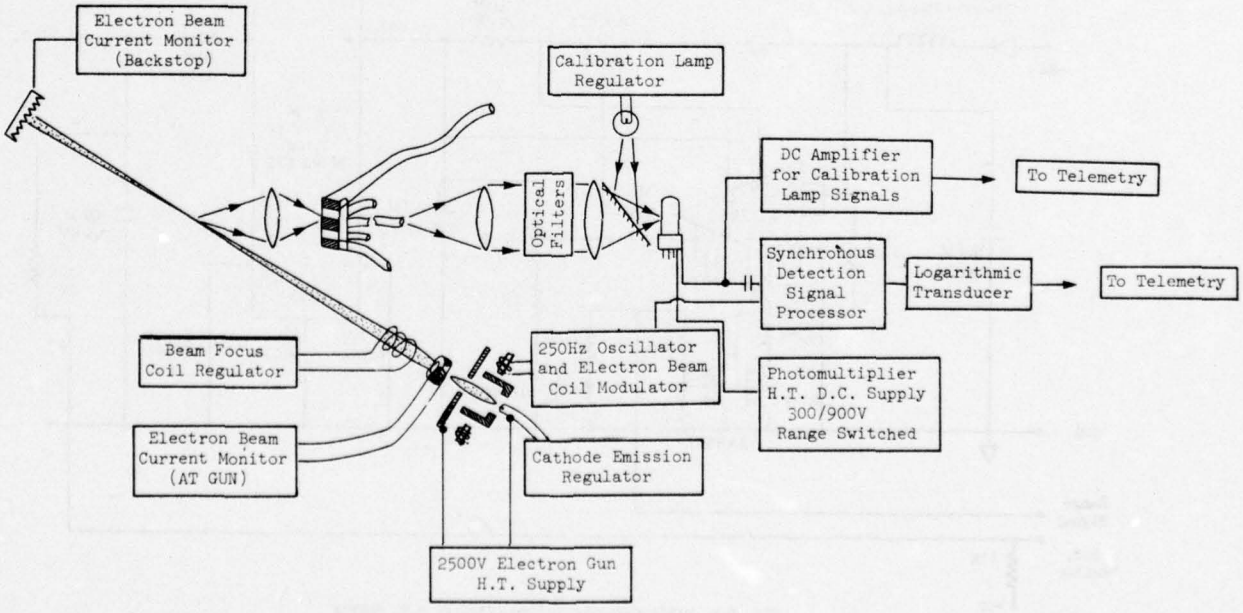


FIG. D-2 MODULATED ELECTRON BEAM SYSTEM

PRECEDING PAGE BLANK-NOT FILMED

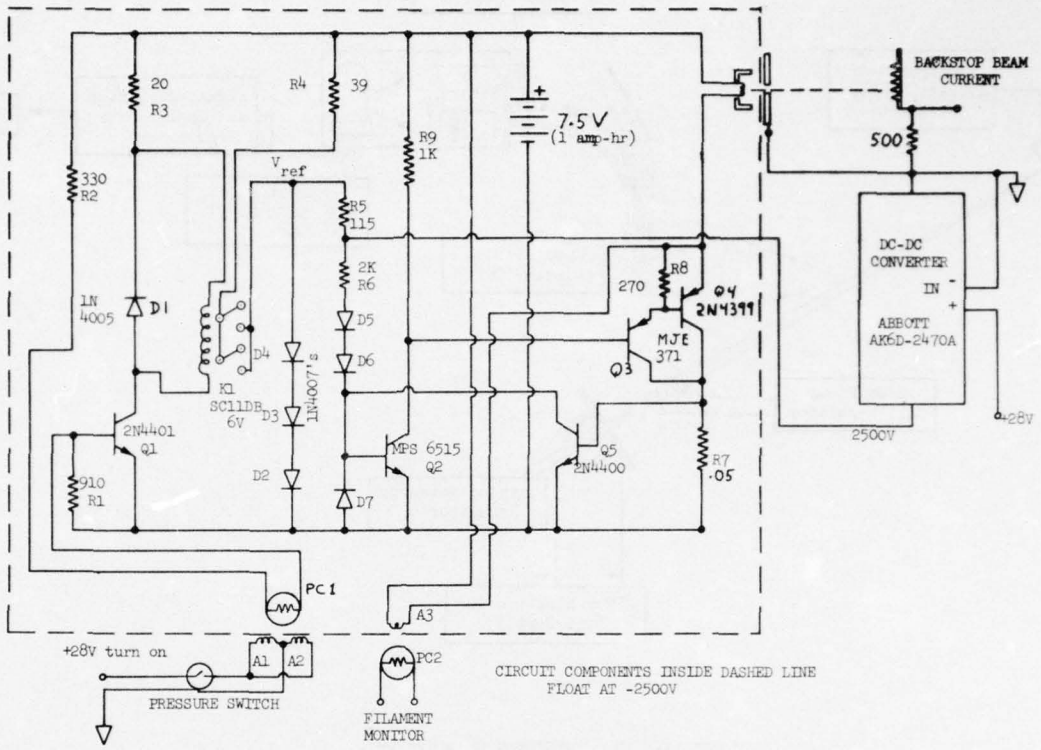


FIG. D-3 ELECTRON GUN CATHODE EMISSION REGULATOR

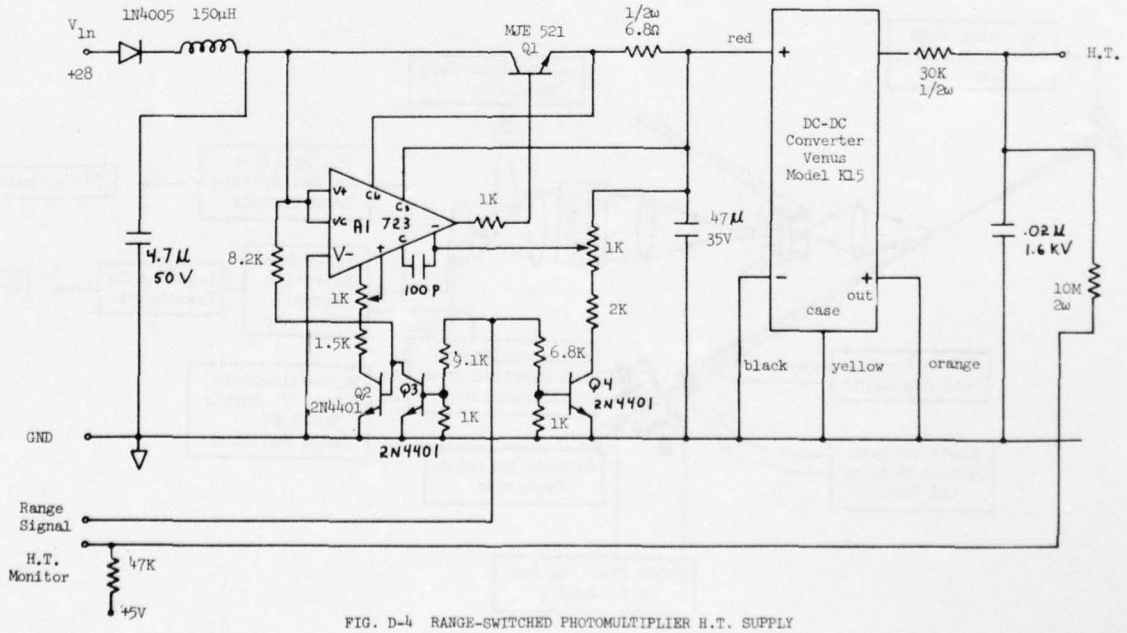


FIG. D-4 RANGE-SWITCHED PHOTOMULTIPLIER H.T. SUPPLY

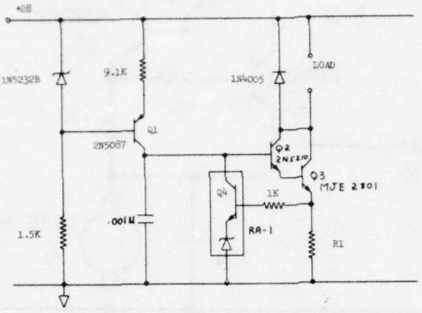


FIG. D-5 CURRENT REGULATOR FOR CALIBRATION LAMP AND ELECTRON GUN FOCUS COIL

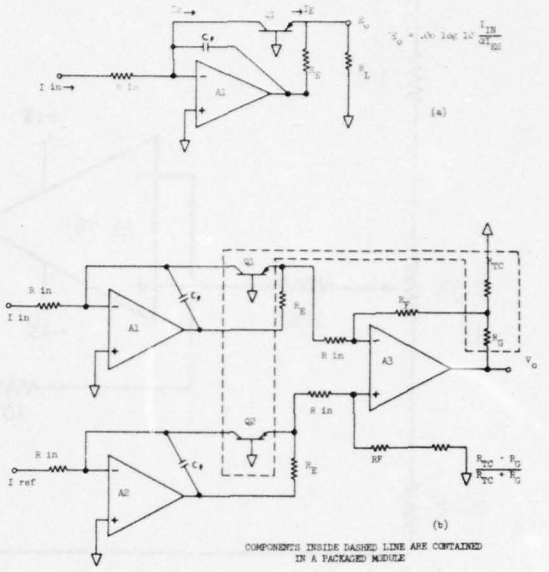


FIG. D-6 (a) LOGARITHMIC CIRCUIT (TRANSDIODE CONFIGURATION) (b) TEMPERATURE COMPENSATED LOGARITHMIC TRANSDUCER

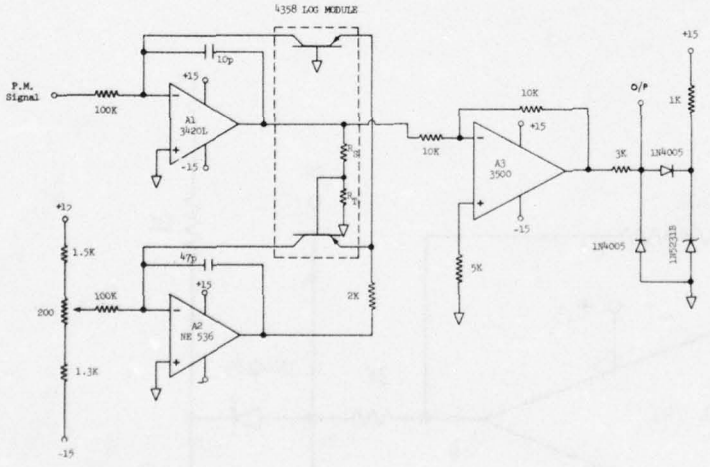


FIG. D-7 SIGNAL HANDLING FOR DC BEAM EBFP

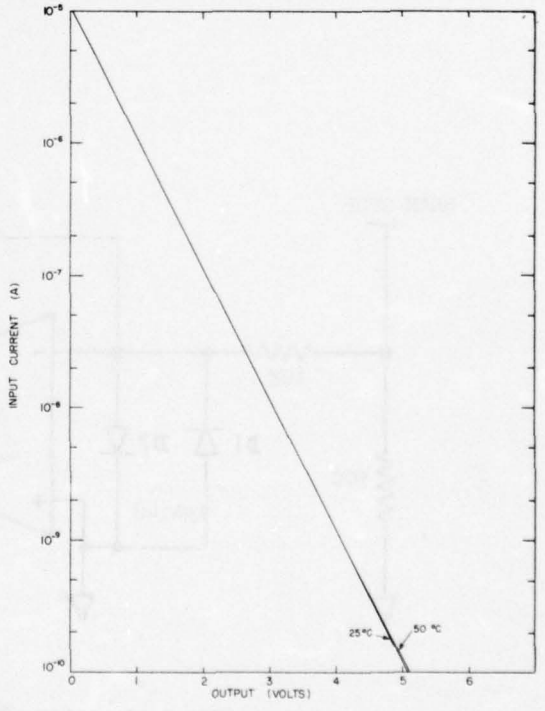


FIG. D-8 CALIBRATION OF LOGARITHMIC CONVERTER FOR D.C. BEAM EBFP PHOTOCURRENTS

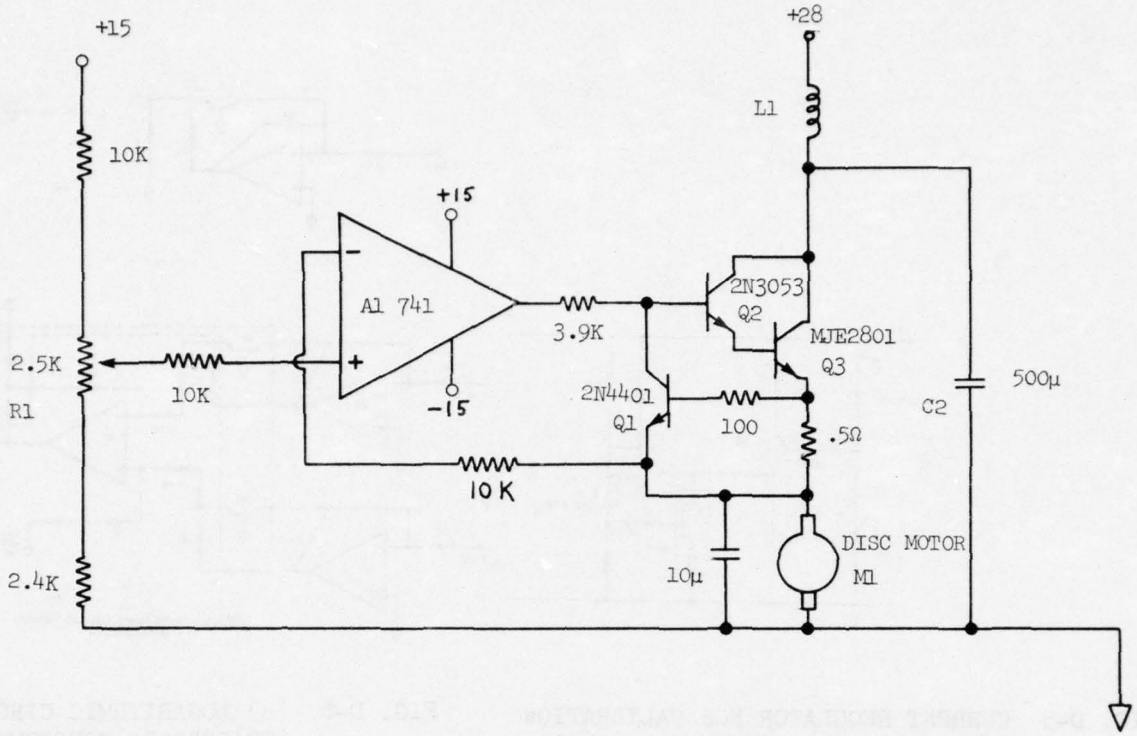


FIG. D-9 FILTER DISC MOTOR DRIVE

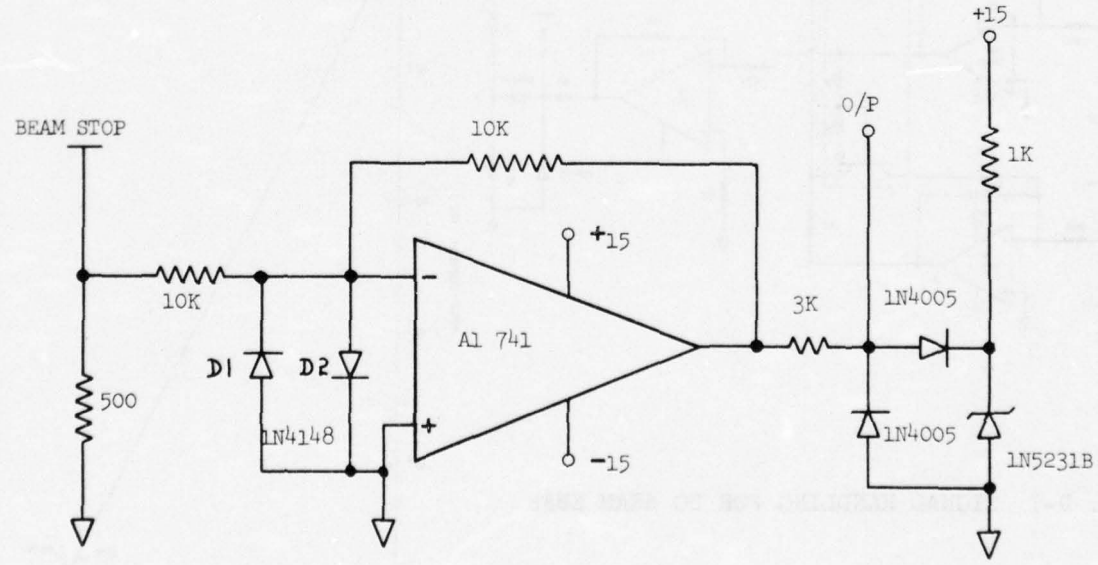


FIG. D-10 ELECTRON BEAM CURRENT MONITOR (BACKSTOP)

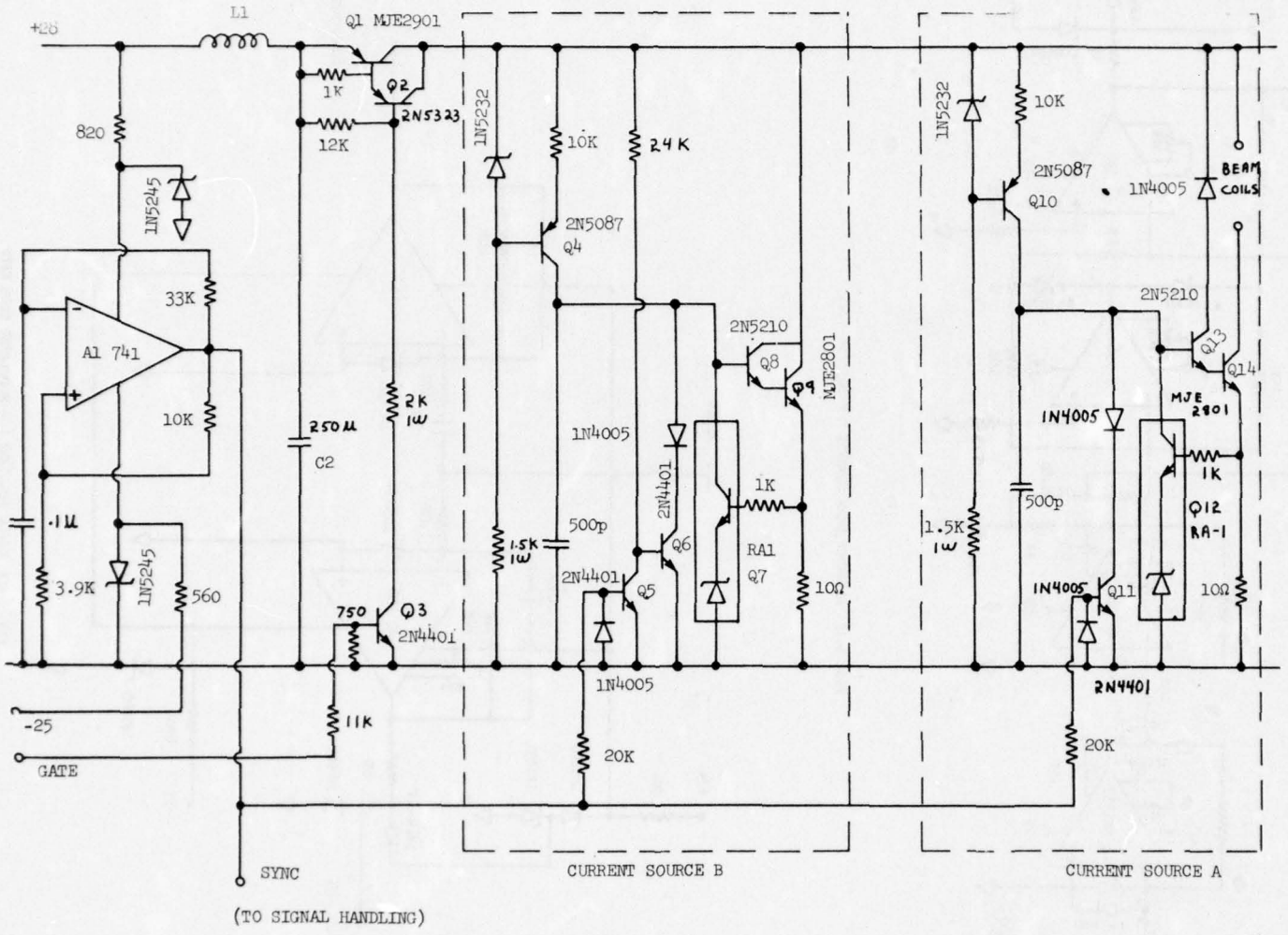


FIG. D-11 COIL DRIVE FOR ELECTRON BEAM MODULATOR

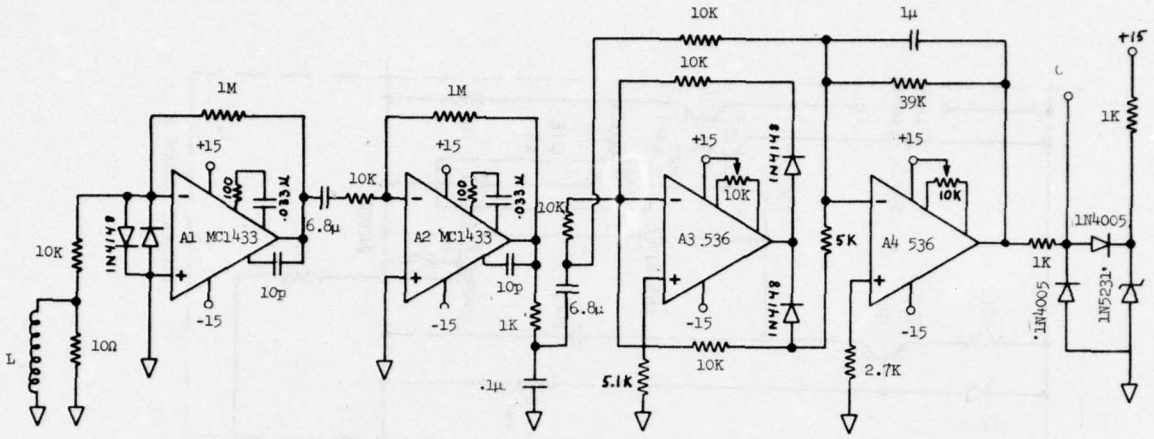


FIG. D-12 ELECTRON BEAM CURRENT MONITOR (AT GUN)

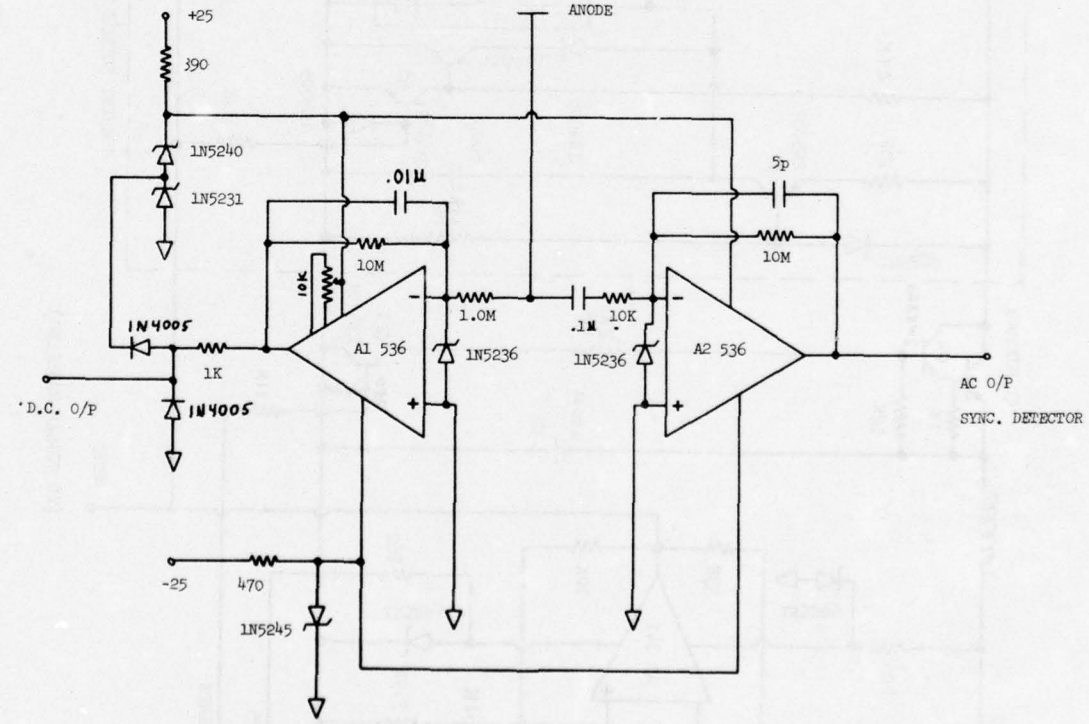


FIG. D-13 AC/DC FOLLOWER FOR MODULATED BEAM EBFF

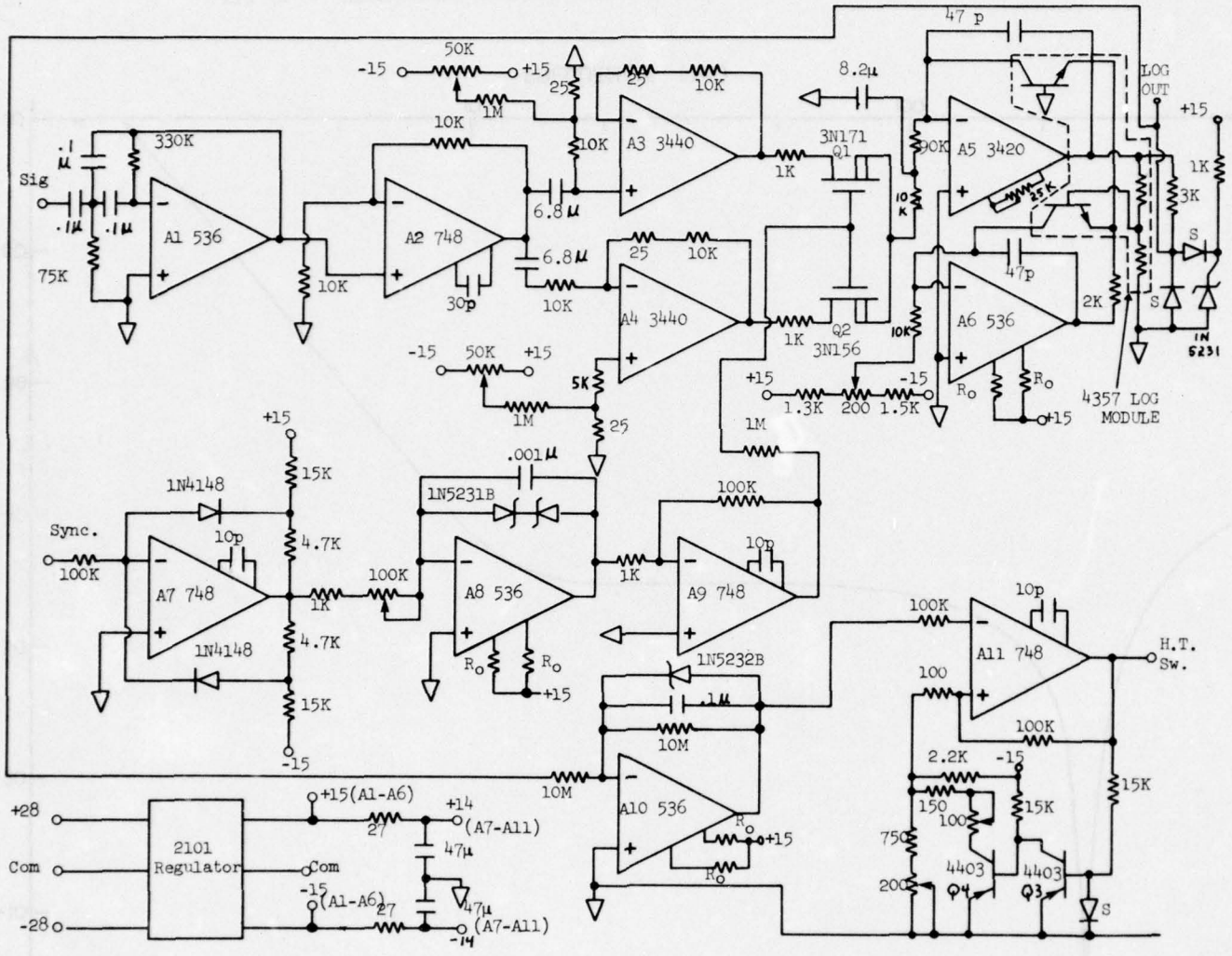


FIG. D-14 SIGNAL HANDLING FOR A.C. COMPONENT OF MODULATED BEAM EBFP (SYNCHRONOUS DETECTION)

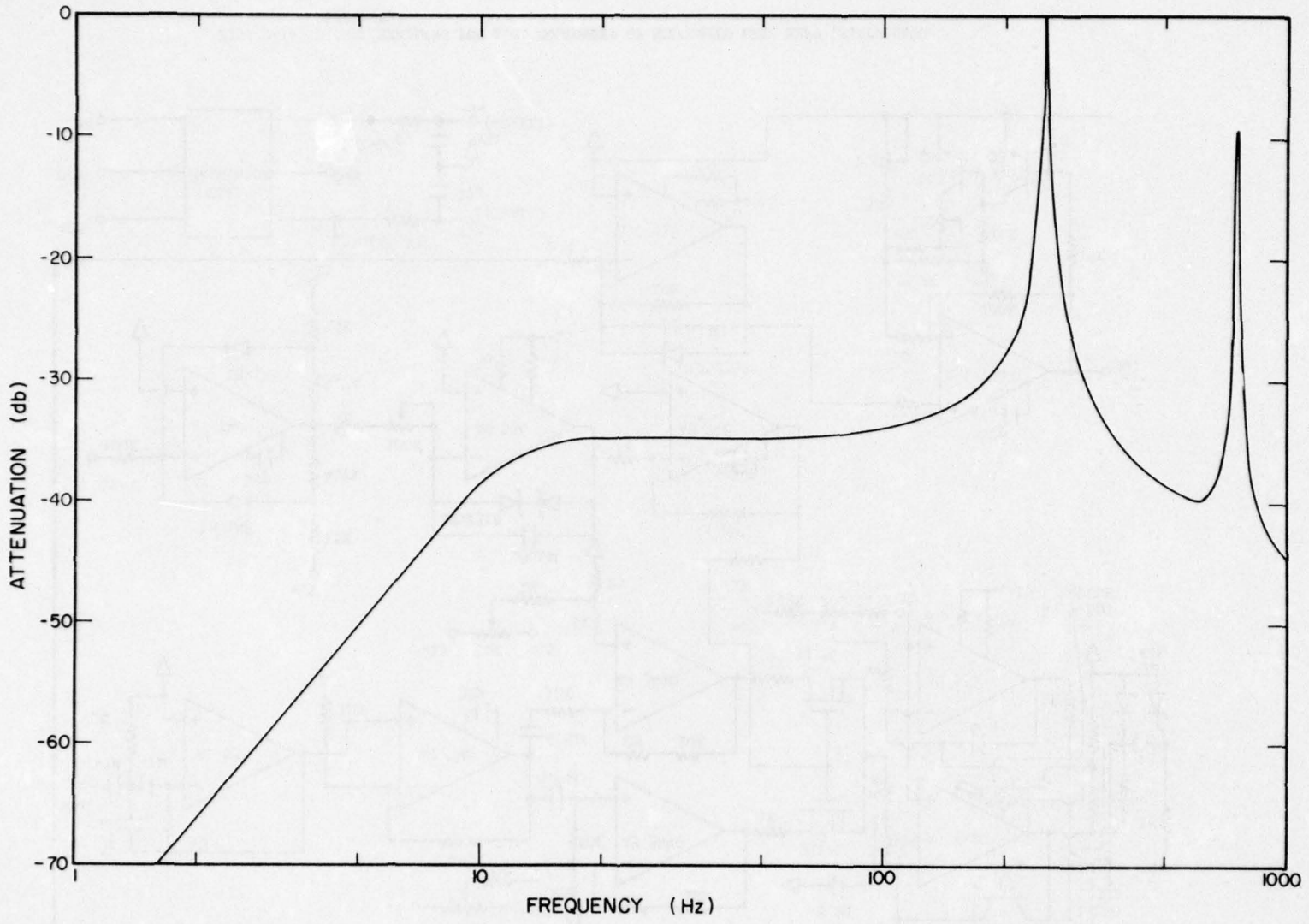


FIG. D-15 SYNCHRONOUS DETECTOR BACKGROUND REJECTION CAPABILITY (82 ms POST FILTER TIME CONSTANT)

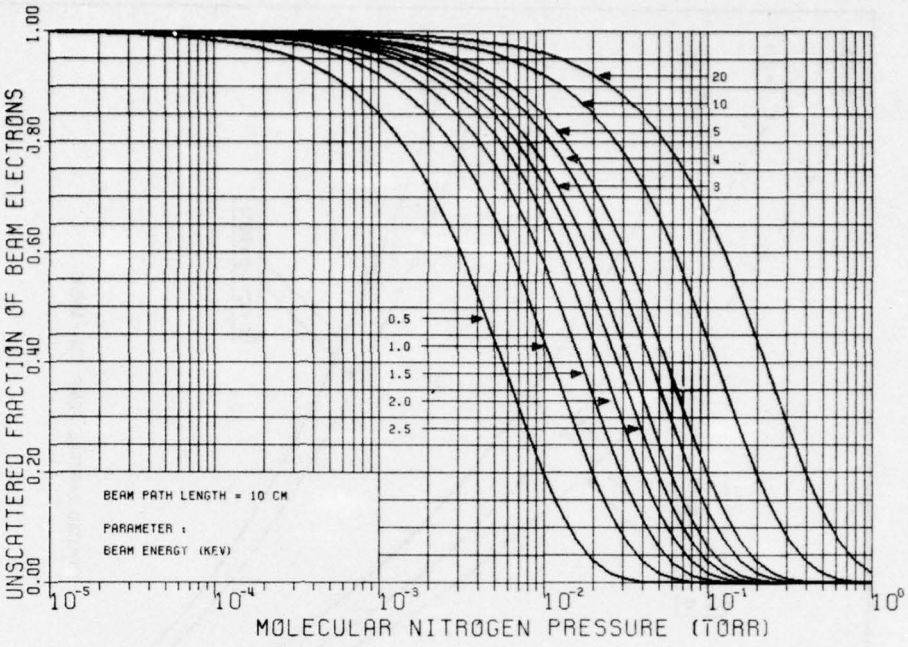


FIG. 1 ELECTRON BEAM ATTENUATION IN NITROGEN

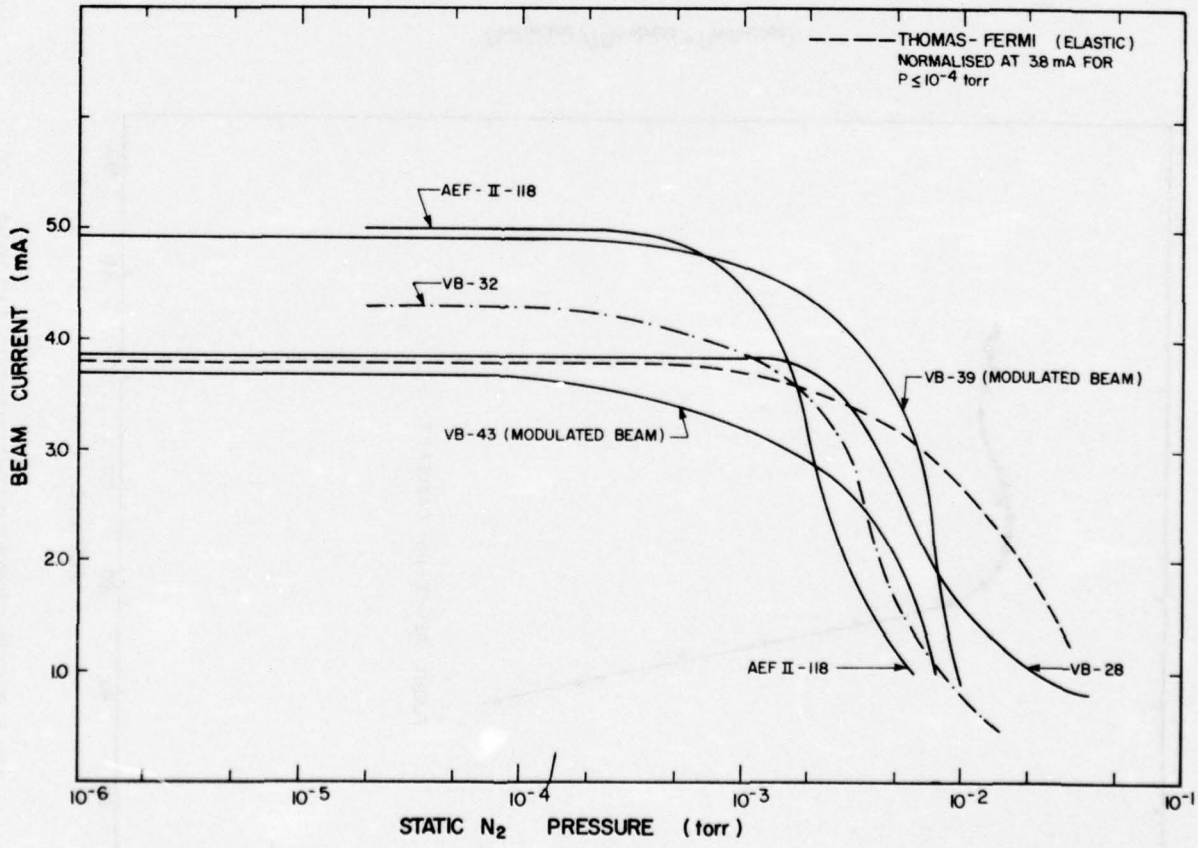


FIG. 2 BEAM ATTENUATION FOR LABORATORY CALIBRATION OF AEF-II-118, VB-32, VB-28, VB-39 and VB-43 EBFP

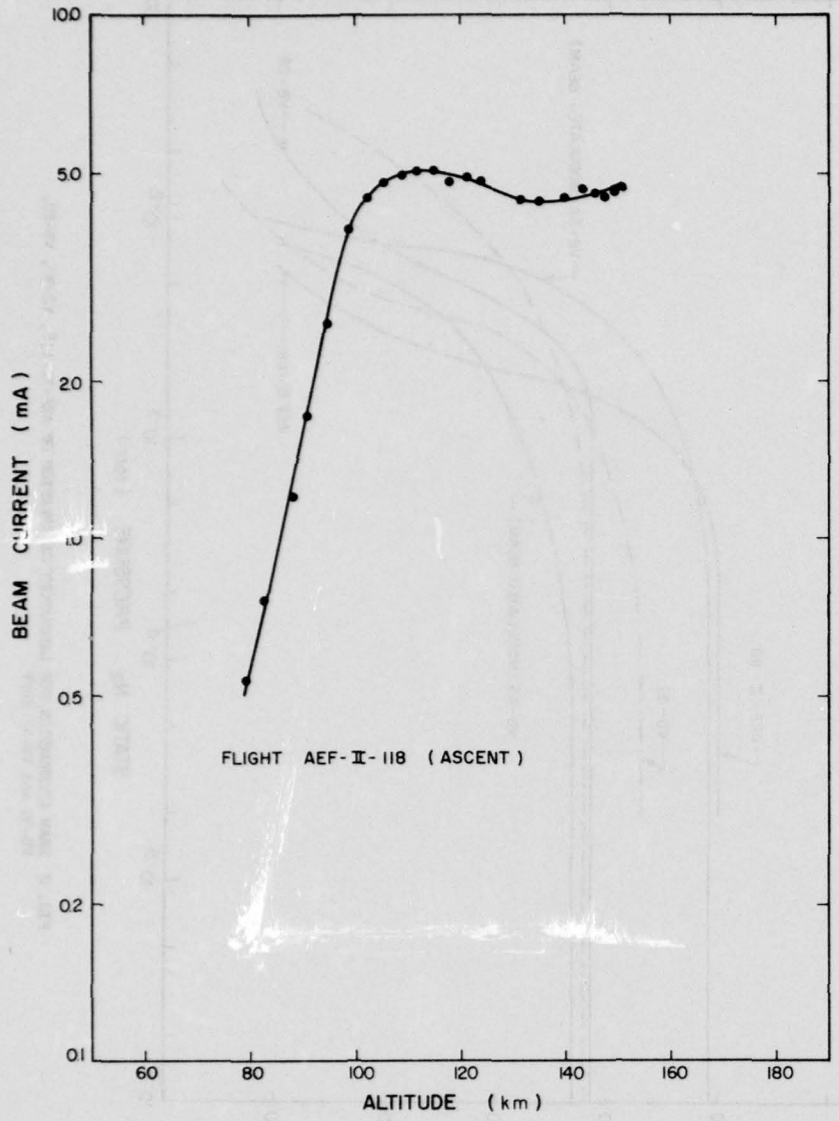


FIG. 3 COLLECTED ELECTRON BEAM CURRENT DURING FLIGHT AEF-II-118

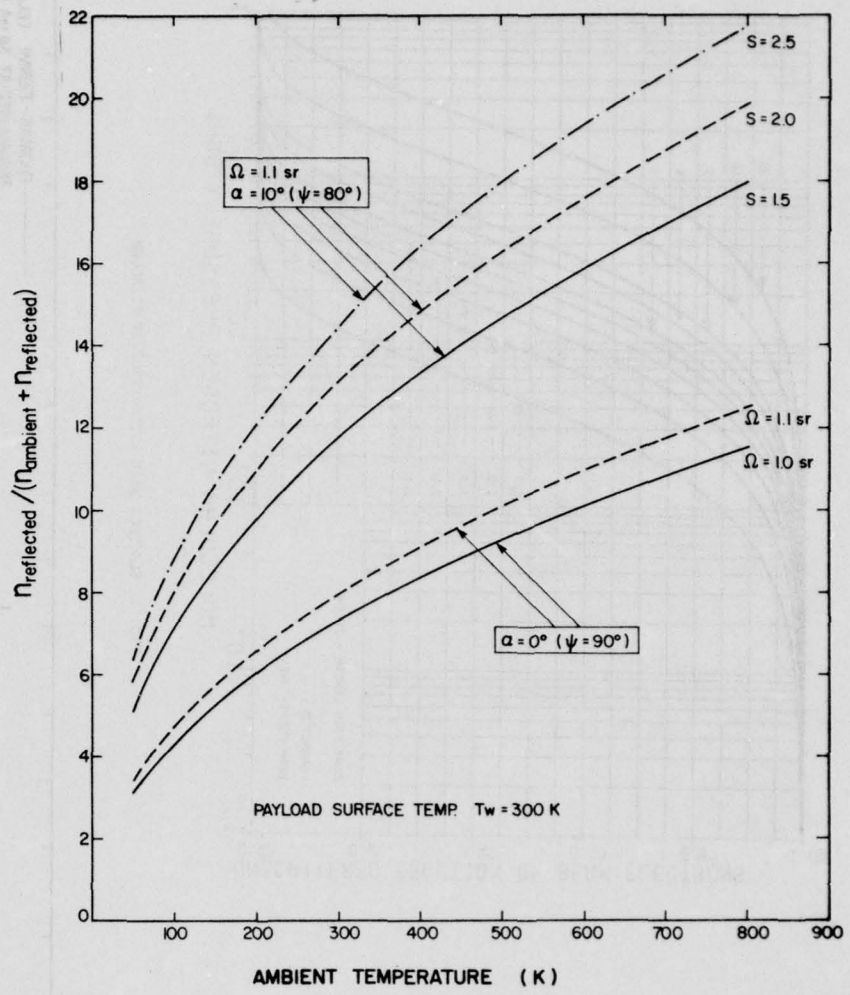


FIG. 4 CALCULATED PARTIAL DENSITY OF REFLECTED MOLECULES FOR EBFP-RTA

FIG. 5 (A) RELATIVE SPECTRAL RESPONSE FUNCTIONS FOR EBFP-RTA FILTER 1 (LAMBDA SHIFT= 0.0 ANGSTROM)

K*	R BRANCH (0,1) BAND		P BRANCH (0,1) BAND		R BRANCH (1,2) BAND		P BRANCH (1,2) BAND	
	WAVELENGTH (A)	REL TOU F1R01	WAVELENGTH (A)	REL TOU F1P01	WAVELENGTH (A)	REL TOU F1R12	WAVELENGTH (A)	REL TOU F1P12
0	4273.936	4.043E-03	4274.631	4.039E-03	4232.507	6.672E-03	4233.181	7.964E-03
1	4273.179	5.724E-03	4275.264	3.618E-03	4231.771	5.286E-03	4233.794	9.136E-03
2	4272.360	7.550E-03	4275.834	3.583E-03	4230.974	4.523E-03	4234.346	1.066E-02
3	4271.479	9.441E-03	4276.342	3.580E-03	4230.116	3.698E-03	4234.836	1.163E-02
4	4270.535	1.132E-02	4276.788	3.577E-03	4229.197	2.812E-03	4235.265	1.286E-02
5	4269.530	1.316E-02	4277.171	3.243E-03	4228.217	2.350E-03	4235.632	1.423E-02
6	4268.463	1.573E-02	4277.492	3.126E-03	4227.176	1.340E-03	4235.938	1.566E-02
7	4267.335	2.073E-02	4277.750	3.125E-03	4226.074	2.675E-04	4236.182	1.705E-02
8	4266.144	2.966E-02	4277.946	2.994E-03	4224.911	0.000E+00	4236.364	1.797E-02
9	4264.893	4.252E-02	4278.079	2.874E-03	4223.688	0.000E+00	4236.485	1.843E-02
10	4263.579	6.174E-02	4278.149	2.811E-03	4222.404	0.000E+00	4236.544	1.866E-02
11	4262.205	9.255E-02	4278.157	2.803E-03	4221.059	0.000E+00	4236.541	1.865E-02
12	4260.769	1.558E-01	4278.103	2.852E-03	4219.655	0.000E+00	4236.477	1.840E-02
13	4259.273	2.573E-01	4277.986	2.957E-03	4218.190	0.000E+00	4236.351	1.792E-02
14	4257.715	4.624E-01	4277.806	3.119E-03	4216.665	0.000E+00	4236.163	1.695E-02
15	4256.097	7.325E-01	4277.564	3.126E-03	4215.080	0.000E+00	4235.914	1.552E-02
16	4254.418	9.962E-01	4277.259	3.163E-03	4213.436	0.000E+00	4235.603	1.412E-02
17	4252.678	1.098E+00	4276.892	3.494E-03	4211.731	0.000E+00	4235.231	1.276E-02
18	4250.878	1.030E+00	4276.463	3.579E-03	4209.968	0.000E+00	4234.797	1.152E-02
19	4249.018	8.261E-01	4275.971	3.582E-03	4208.145	0.000E+00	4234.302	1.058E-02
20	4247.098	5.172E-01	4275.416	3.585E-03	4206.262	0.000E+00	4233.745	9.042E-03
21	4245.118	2.653E-01	4274.800	4.037E-03	4204.321	0.000E+00	4233.127	7.859E-03
22	4243.079	1.215E-01	4274.121	4.042E-03	4202.321	0.000E+00	4232.447	6.557E-03
23	4240.980	6.128E-02	4273.380	5.180E-03	4200.262	0.000E+00	4231.706	5.224E-03
24	4238.821	3.311E-02	4272.576	7.157E-03	4198.144	0.000E+00	4230.904	4.455E-03
25	4236.604	1.888E-02	4271.711	8.808E-03	4195.969	0.000E+00	4230.041	3.626E-03
26	4234.327	1.063E-02	4270.784	1.086E-02	4193.735	0.000E+00	4229.117	2.734E-03
27	4231.992	5.643E-03	4269.795	1.267E-02	4191.443	0.000E+00	4228.131	2.267E-03
28	4229.598	3.199E-03	4268.743	1.470E-02	4189.093	0.000E+00	4227.085	1.252E-03
29	4227.146	1.311E-03	4267.631	1.938E-02	4186.686	0.000E+00	4225.978	1.739E-04
30	4224.635	0.000E+00	4266.456	2.723E-02	4184.221	0.000E+00	4224.810	0.000E+00
31	4222.067	0.000E+00	4265.220	3.801E-02	4181.699	0.000E+00	4223.581	0.000E+00
32	4219.441	0.000E+00	4263.923	5.623E-02	4179.121	0.000E+00	4222.292	0.000E+00
33	4216.757	0.000E+00	4262.564	8.279E-02	4176.485	0.000E+00	4220.943	0.000E+00
34	4214.016	0.000E+00	4261.144	1.378E-01	4173.793	0.000E+00	4219.533	0.000E+00
35	4211.218	0.000E+00	4259.663	2.266E-01	4171.045	0.000E+00	4218.063	0.000E+00
36	4208.363	0.000E+00	4258.121	3.938E-01	4168.240	0.000E+00	4216.533	0.000E+00
37	4205.452	0.000E+00	4256.519	6.554E-01	4165.380	0.000E+00	4214.944	0.000E+00
38	4202.484	0.000E+00	4254.855	9.453E-01	4162.464	0.000E+00	4213.294	0.000E+00
39	4199.461	0.000E+00	4253.131	1.090E+00	4159.493	0.000E+00	4211.585	0.000E+00
40	4196.381	0.000E+00	4251.347	1.065E+00	4156.467	0.000E+00	4209.816	0.000E+00
41	4193.246	0.000E+00	4249.502	8.920E-01	4153.386	0.000E+00	4207.988	0.000E+00
42	4190.055	0.000E+00	4247.598	5.981E-01	4150.250	0.000E+00	4206.100	0.000E+00
43	4186.810	0.000E+00	4245.633	3.121E-01	4147.060	0.000E+00	4204.154	0.000E+00
44	4183.509	0.000E+00	4243.609	1.475E-01	4143.816	0.000E+00	4202.149	0.000E+00
45	4180.154	0.000E+00	4241.525	7.283E-02	4140.518	0.000E+00	4200.085	0.000E+00
46	4176.745	0.000E+00	4239.382	3.788E-02	4137.166	0.000E+00	4197.963	0.000E+00
47	4173.282	0.000E+00	4237.180	2.143E-02	4133.761	0.000E+00	4195.782	0.000E+00
48	4169.765	0.000E+00	4234.918	1.187E-02	4130.303	0.000E+00	4193.543	0.000E+00
49	4166.195	0.000E+00	4232.598	6.847E-03	4126.793	0.000E+00	4191.246	0.000E+00
50	4162.571	0.000E+00	4230.219	3.797E-03	4123.230	0.000E+00	4188.892	0.000E+00

FIG. 5 (B) RELATIVE SPECTRAL RESPONSE FUNCTIONS FOR EBFP-RTA FILTER 2 (LAMBDA SHIFT= 0.0 ANGSTROM)

K*	R BRANCH (0,1) BAND		P BRANCH (0,1) BAND		R BRANCH (1,2) BAND		P BRANCH (1,2) BAND	
	WAVELENGTH (A)	REL TOU F2R01	WAVELENGTH (A)	REL TOU F2P01	WAVELENGTH (A)	REL TOU F2R12	WAVELENGTH (A)	REL TOU F2P12
0	4273.936	3.512E-01	4274.631	2.522E-01	4232.507	0.000E+00	4233.181	0.000E+00
1	4273.179	4.816E-01	4275.264	1.778E-01	4231.771	0.000E+00	4233.794	0.000E+00
2	4272.360	6.505E-01	4275.834	1.420E-01	4230.974	0.000E+00	4234.346	0.000E+00
3	4271.479	8.287E-01	4276.342	1.079E-01	4230.116	0.000E+00	4234.836	0.000E+00
4	4270.535	9.523E-01	4276.788	9.212E-02	4229.197	0.000E+00	4235.265	0.000E+00
5	4269.530	9.947E-01	4277.171	7.535E-02	4228.217	0.000E+00	4235.632	0.000E+00
6	4268.463	9.319E-01	4277.492	6.537E-02	4227.176	0.000E+00	4235.938	0.000E+00
7	4267.335	7.717E-01	4277.750	5.957E-02	4226.074	0.000E+00	4236.182	0.000E+00
8	4266.144	5.506E-01	4277.946	5.492E-02	4224.911	0.000E+00	4236.364	0.000E+00
9	4264.893	3.425E-01	4278.079	5.171E-02	4223.688	0.000E+00	4236.485	0.000E+00
10	4263.579	1.797E-01	4278.149	5.030E-02	4222.404	0.000E+00	4236.544	0.000E+00
11	4262.205	9.195E-02	4278.157	4.981E-02	4221.059	0.000E+00	4236.541	0.000E+00
12	4260.769	4.855E-02	4278.103	5.113E-02	4219.655	0.000E+00	4236.477	0.000E+00
13	4259.273	2.853E-02	4277.986	5.395E-02	4218.190	0.000E+00	4236.351	0.000E+00
14	4257.715	1.8[illegible]E-02	4277.806	5.829E-02	4216.665	0.000E+00	4236.163	0.000E+00
15	4256.097	1.238E-02	4277.564	6.374E-02	4215.080	0.000E+00	4235.914	0.000E+00
16	4254.418	9.153E-03	4277.259	7.145E-02	4213.436	0.000E+00	4235.603	0.000E+00
17	4252.678	6.617E-03	4276.892	8.762E-02	4211.731	0.000E+00	4235.231	0.000E+00
18	4250.878	4.190E-03	4276.463	1.036E-01	4209.968	0.000E+00	4234.797	0.000E+00
19	4249.018	3.158E-03	4275.971	1.324E-01	4208.145	0.000E+00	4234.302	0.000E+00
20	4247.098	2.716E-03	4275.416	1.667E-01	4206.262	0.000E+00	4233.745	0.000E+00
21	4245.118	2.271E-03	4274.800	2.336E-01	4204.321	0.000E+00	4233.127	0.000E+00
22	4243.079	1.622E-03	4274.121	3.195E-01	4202.321	0.000E+00	4232.447	0.000E+00
23	4240.980	0.000E+00	4273.380	4.389E-01	4200.262	0.000E+00	4231.706	0.000E+00
24	4238.821	0.000E+00	4272.576	6.144E-01	4198.144	0.000E+00	4230.904	0.000E+00
25	4236.604	0.000E+00	4271.711	8.001E-01	4195.969	0.000E+00	4230.041	0.000E+00
26	4234.327	0.000E+00	4270.784	9.286E-01	4193.735	0.000E+00	4229.117	0.000E+00
27	4231.992	0.000E+00	4269.795	9.995E-01	4191.443	0.000E+00	4228.131	0.000E+00
28	4229.598	0.000E+00	4268.743	9.610E-01	4189.093	0.000E+00	4227.085	0.000E+00
29	4227.146	0.000E+00	4267.631	8.205E-01	4186.686	0.000E+00	4225.978	0.000E+00
30	4224.635	0.000E+00	4266.456	6.100E-01	4184.221	0.000E+00	4224.810	0.000E+00
31	4222.067	0.000E+00	4265.220	3.964E-01	4181.699	0.000E+00	4223.581	0.000E+00
32	4219.441	0.000E+00	4263.923	2.137E-01	4179.121	0.000E+00	4222.292	0.000E+00
33	4216.757	0.000E+00	4262.564	1.085E-01	4176.485	0.000E+00	4220.943	0.000E+00
34	4214.016	0.000E+00	4261.144	5.667E-02	4173.793	0.000E+00	4219.533	0.000E+00
35	4211.218	0.000E+00	4259.663	3.267E-02	4171.045	0.000E+00	4218.063	0.000E+00
36	4208.363	0.000E+00	4258.121	2.008E-02	4168.240	0.000E+00	4216.533	0.000E+00
37	4205.452	0.000E+00	4256.519	1.369E-02	4165.380	0.000E+00	4214.944	0.000E+00
38	4202.484	0.000E+00	4254.855	9.928E-03	4162.464	0.000E+00	4213.294	0.000E+00
39	4199.461	0.000E+00	4253.131	7.018E-03	4159.493	0.000E+00	4211.585	0.000E+00
40	4196.381	0.000E+00	4251.347	5.029E-03	4156.467	0.000E+00	4209.816	0.000E+00
41	4193.246	0.000E+00	4249.502	3.156E-03	4153.386	0.000E+00	4207.988	0.000E+00
42	4190.055	0.000E+00	4247.598	2.714E-03	4150.250	0.000E+00	4206.100	0.000E+00
43	4186.810	0.000E+00	4245.633	2.572E-03	4147.060	0.000E+00	4204.154	0.000E+00
44	4183.509	0.000E+00	4243.609	2.103E-03	4143.816	0.000E+00	4202.149	0.000E+00
45	4180.154	0.000E+00	4241.525	2.062E-04	4140.518	0.000E+00	4200.085	0.000E+00
46	4176.745	0.000E+00	4239.382	0.000E+00	4137.166	0.000E+00	4197.963	0.000E+00
47	4173.282	0.000E+00	4237.180	0.000E+00	4133.761	0.000E+00	4195.782	0.000E+00
48	4169.765	0.000E+00	4234.918	0.000E+00	4130.303	0.000E+00	4193.543	0.000E+00
49	4166.195	0.000E+00	4232.598	0.000E+00	4126.793	0.000E+00	4191.246	0.000E+00
50	4162.571	0.000E+00	4230.219	0.000E+00	4123.230	0.000E+00	4188.892	0.000E+00

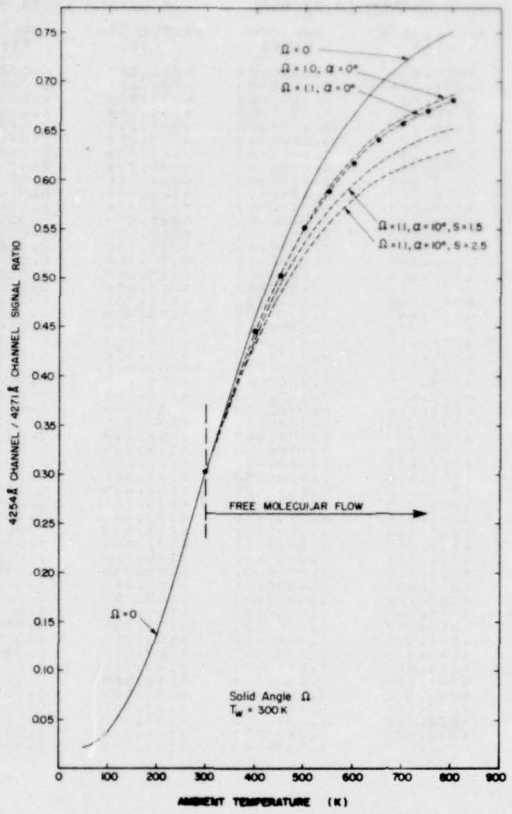


FIG. 6 THEORETICAL CALIBRATION OF EBFP-RTA ON AEF-II-118

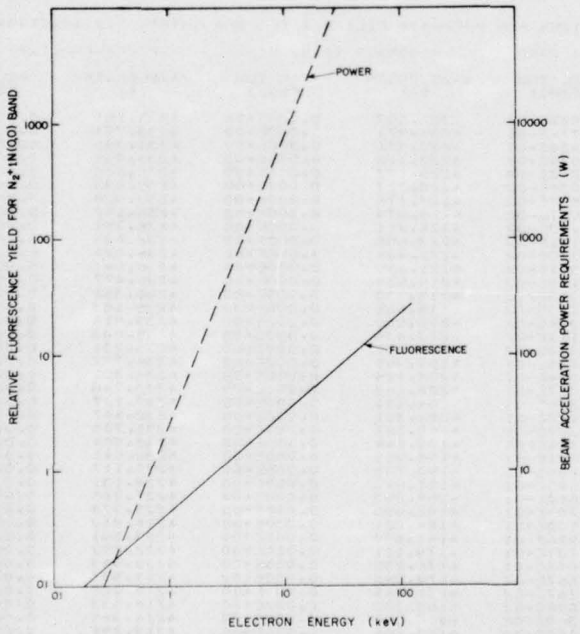


FIG. 7 FLUORESCENCE YIELD AND GUN POWER

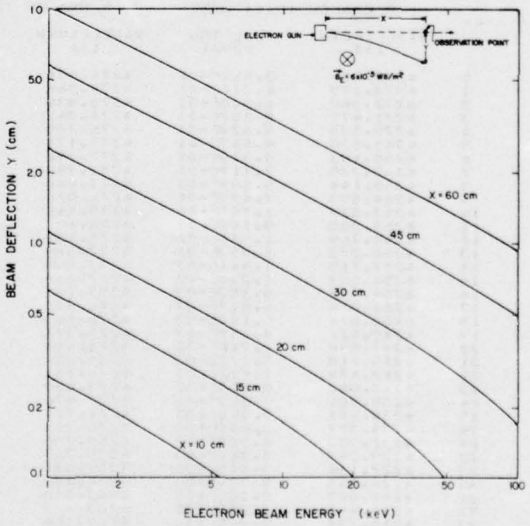


FIG. 8 ELECTRON BEAM DEFLECTION IN EARTH'S MAGNETIC FIELD

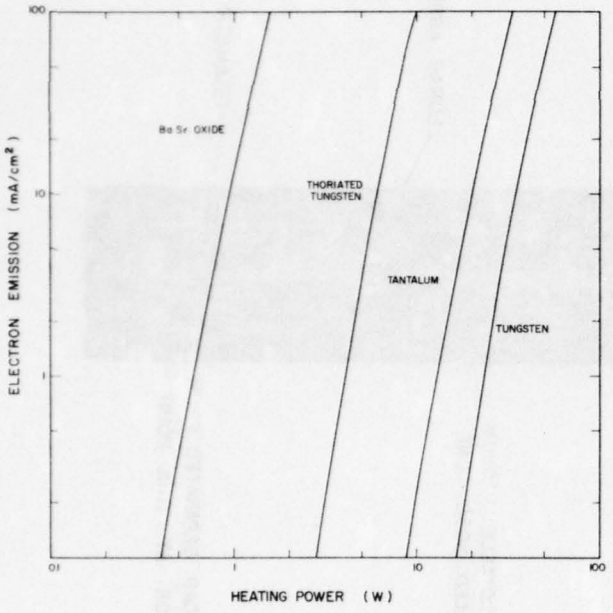


FIG. 9 EMISSION CURRENT DENSITY OF CATHODE MATERIALS

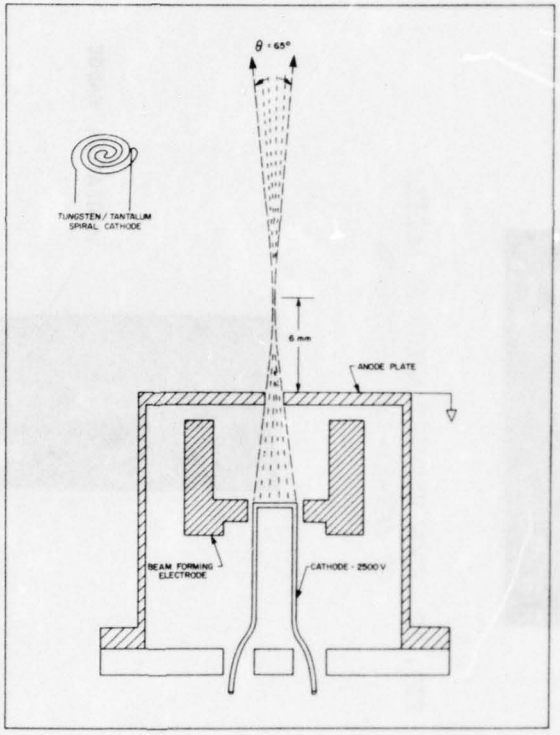


FIG. 10 MODIFIED ELECTRON BEAM WELDING GUN FOR FLIGHT

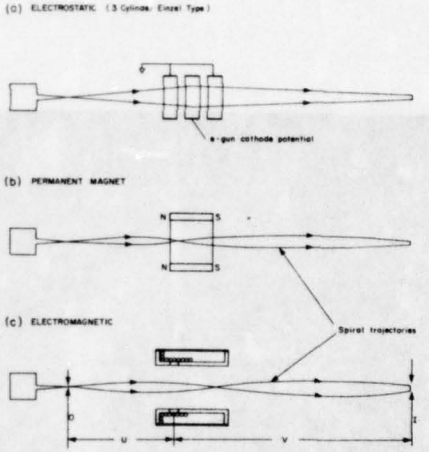


FIG. 11 ELECTRON BEAM FOCUSSING METHODS

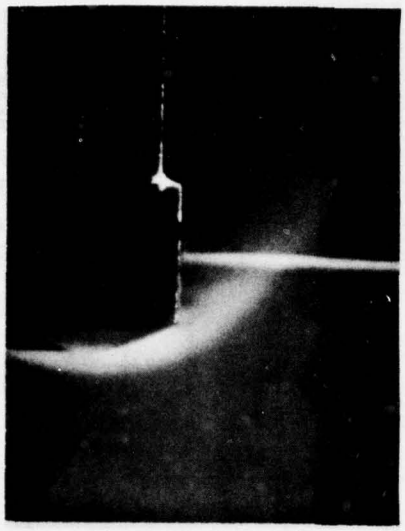


FIG. 12 FLOW VISUALIZATION ON MODEL
OF AEF-II-118 APPARATUS

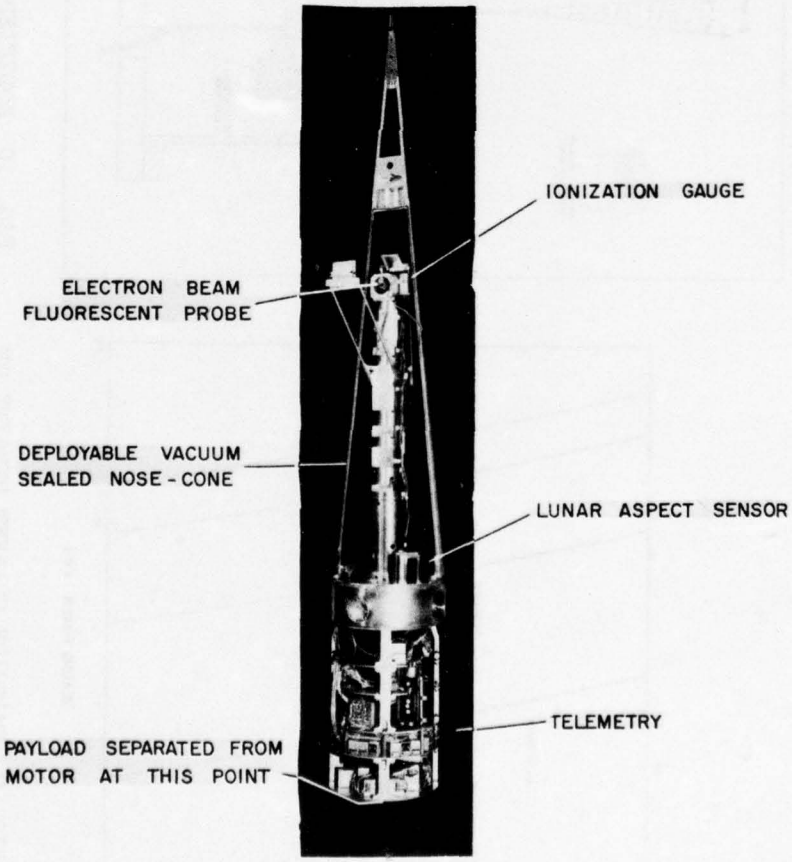


FIG. 13 AEF-II-118 FLIGHT PAYLOAD

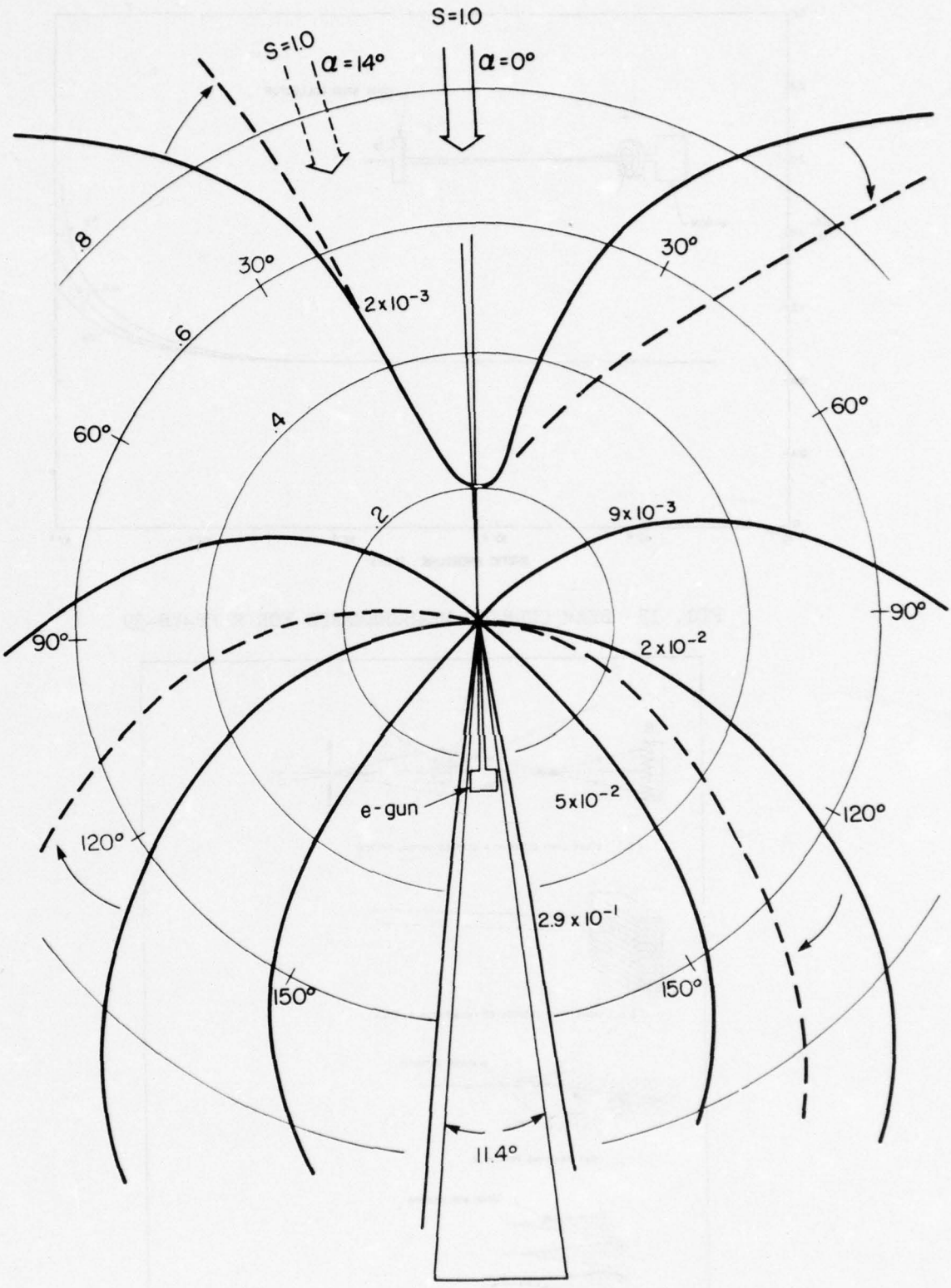


FIG. 14 NORMALIZED CURVES OF CONSTANT REFLECTED NUMBER DENSITY FOR ANGLES OF ATTACK OF 14° AND 0°

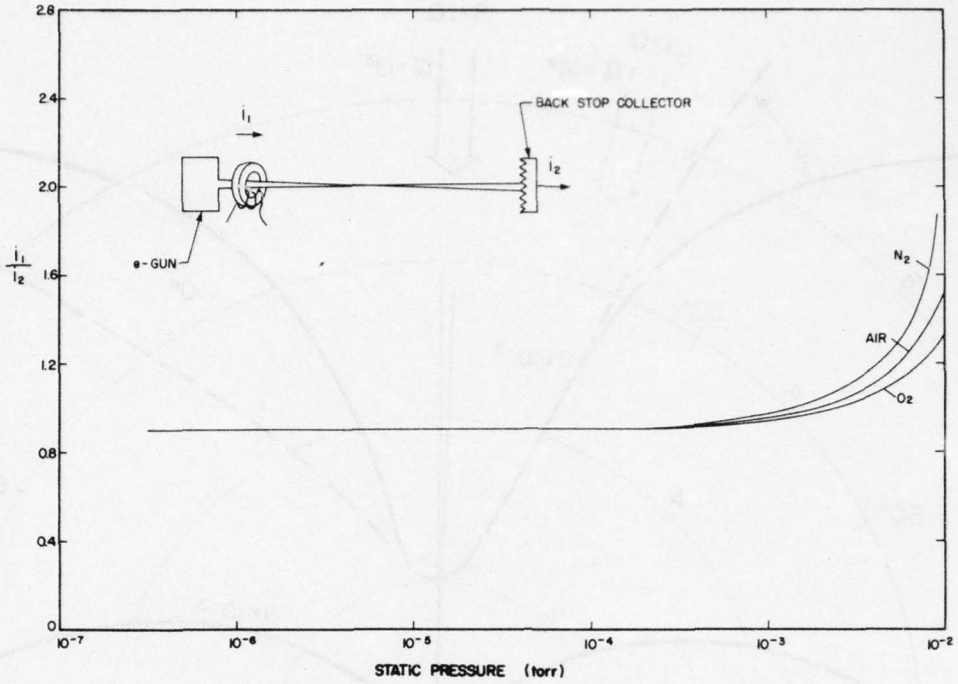


FIG. 15 BEAM CURRENT MEASUREMENTS FOR EBFP-VB-39

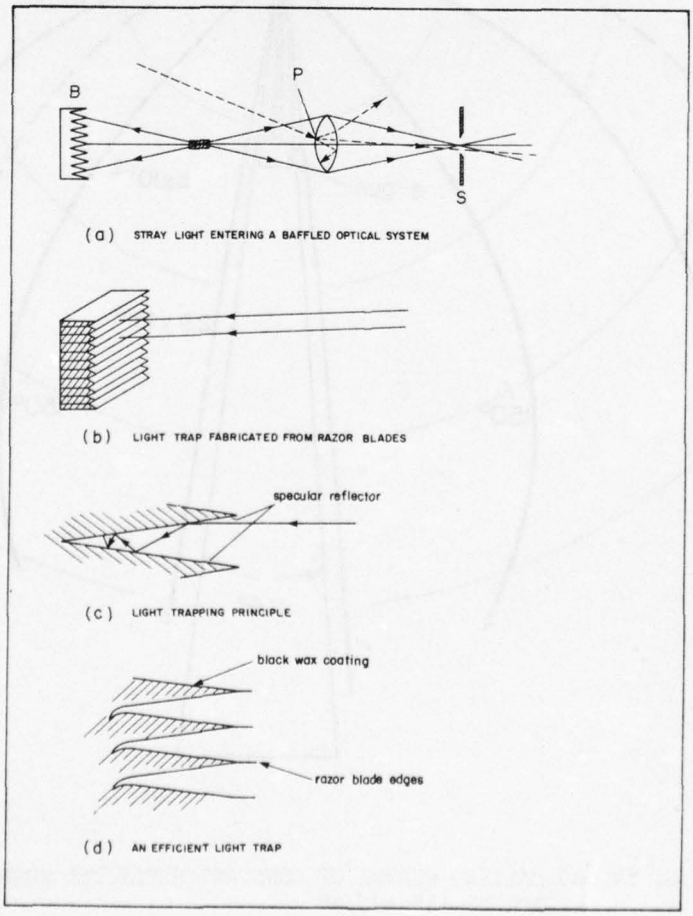
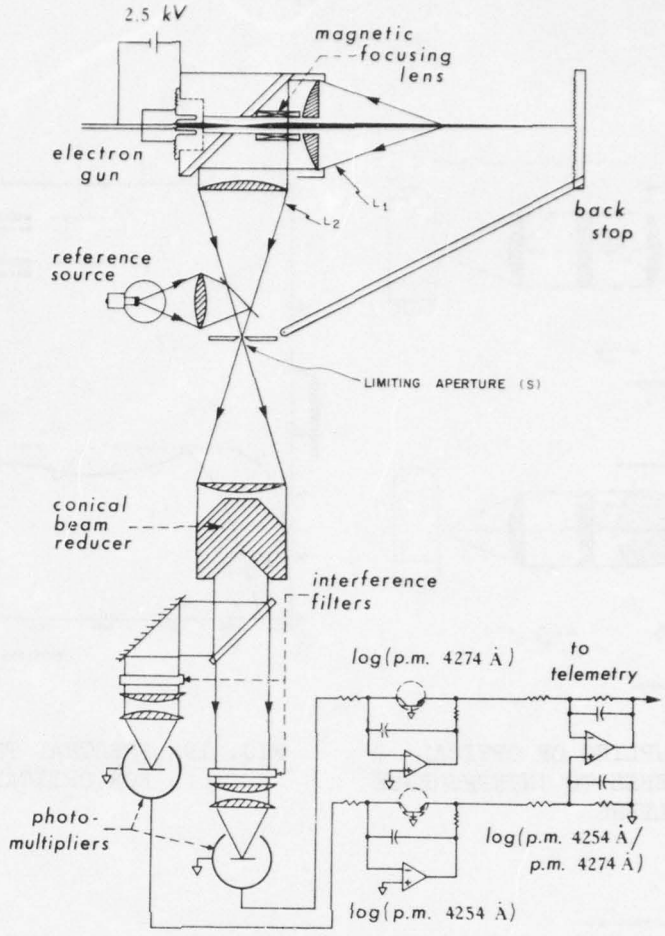


FIG. 16 STRAY LIGHT REJECTION AND LIGHT TRAPPING PROCEDURES FOR EBFP



(a) DIRECT VIEWING,

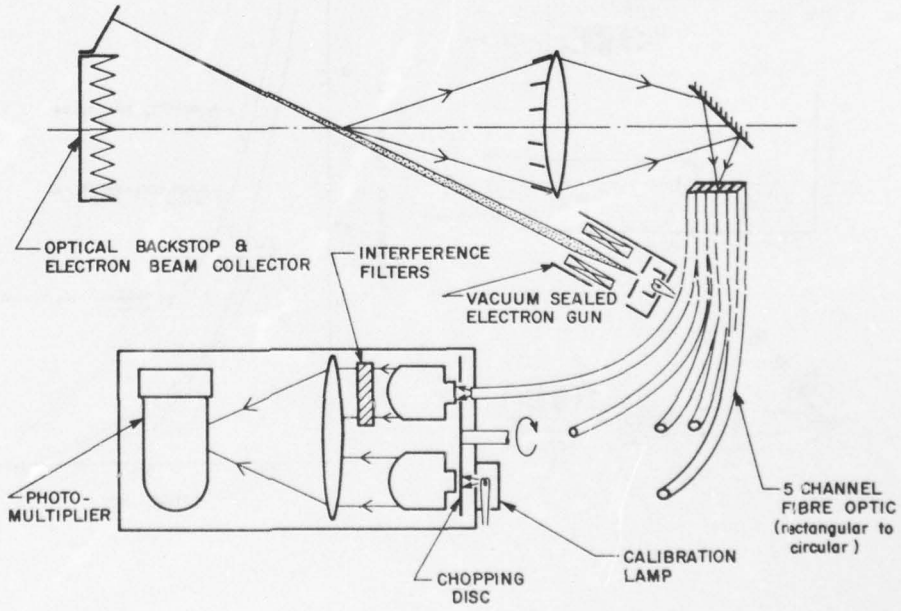


FIG. 17 FLUORESCENCE VIEWING TECHNIQUES: (a) DIRECT VIEWING, (b) FIBRE OPTICS

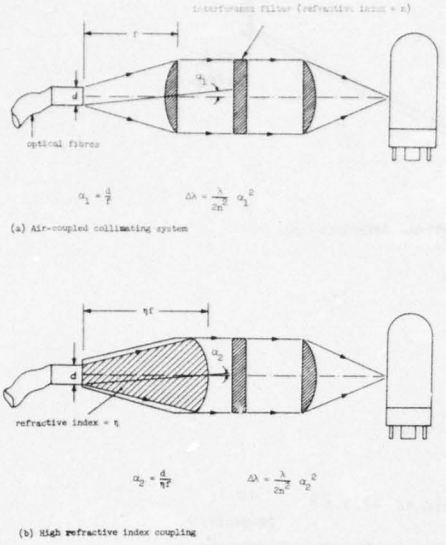


FIG. 18 COUPLING OF OPTICAL FIBRES TO INTERFERENCE FILTERS

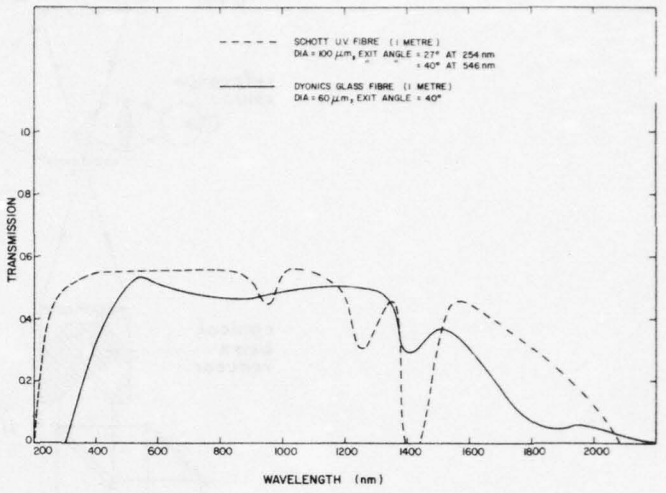


FIG. 19 SPECTRAL TRANSMISSION CURVES FOR OPTICAL FIBRES

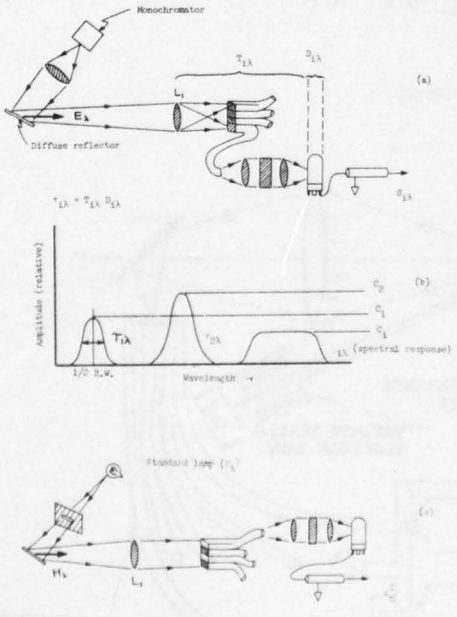


FIG. 20 DETERMINATION OF SPECTRAL RESPONSE FUNCTIONS FOR EBFP

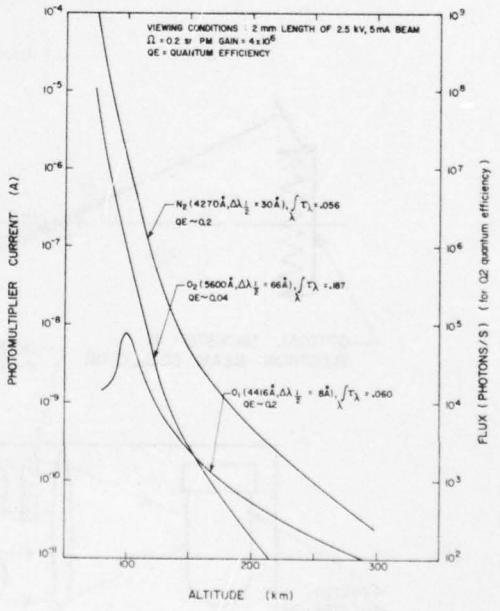


FIG. 21 EXPECTED PHOTOMULTIPLIER SIGNALS FOR FIBRE OPTIC SYSTEM

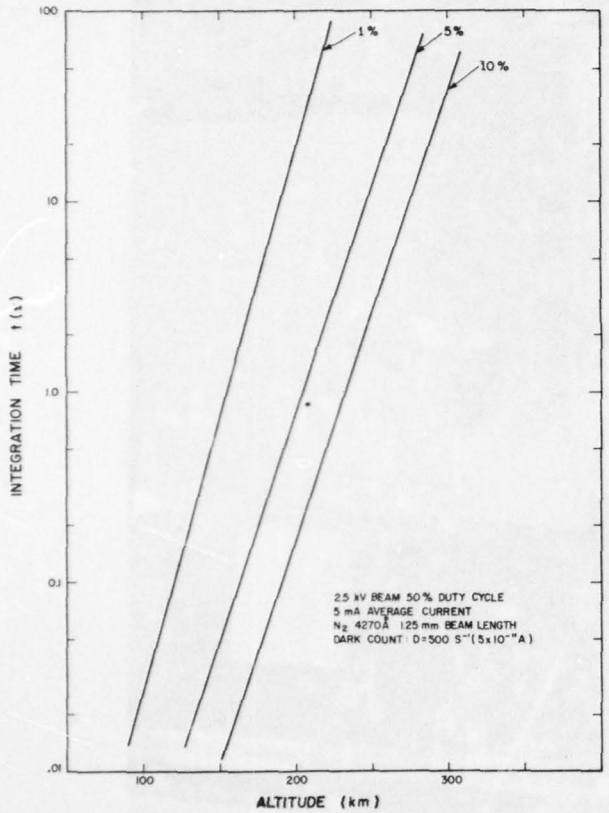


FIG. 22 INTEGRATION TIMES FOR SYNCHRONOUS DETECTION SYSTEM

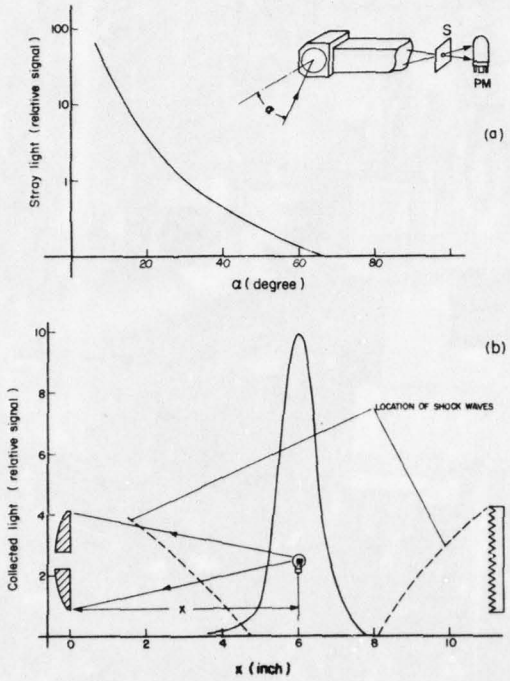


FIG. 23 STRAY LIGHT REJECTION AND OPTICAL COLLECTION FOR DIRECT VIEWING SYSTEM (a) ANGULAR DEPENDENCE, (b) AXIAL COLLECTION EFFECIENCY

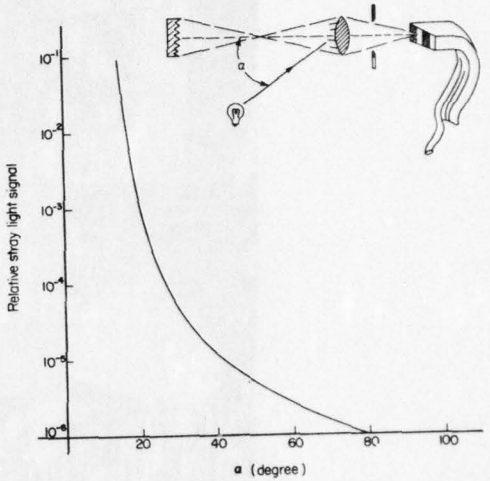


FIG. 24 STRAY LIGHT REJECTION FOR FIBRE OPTIC SYSTEM

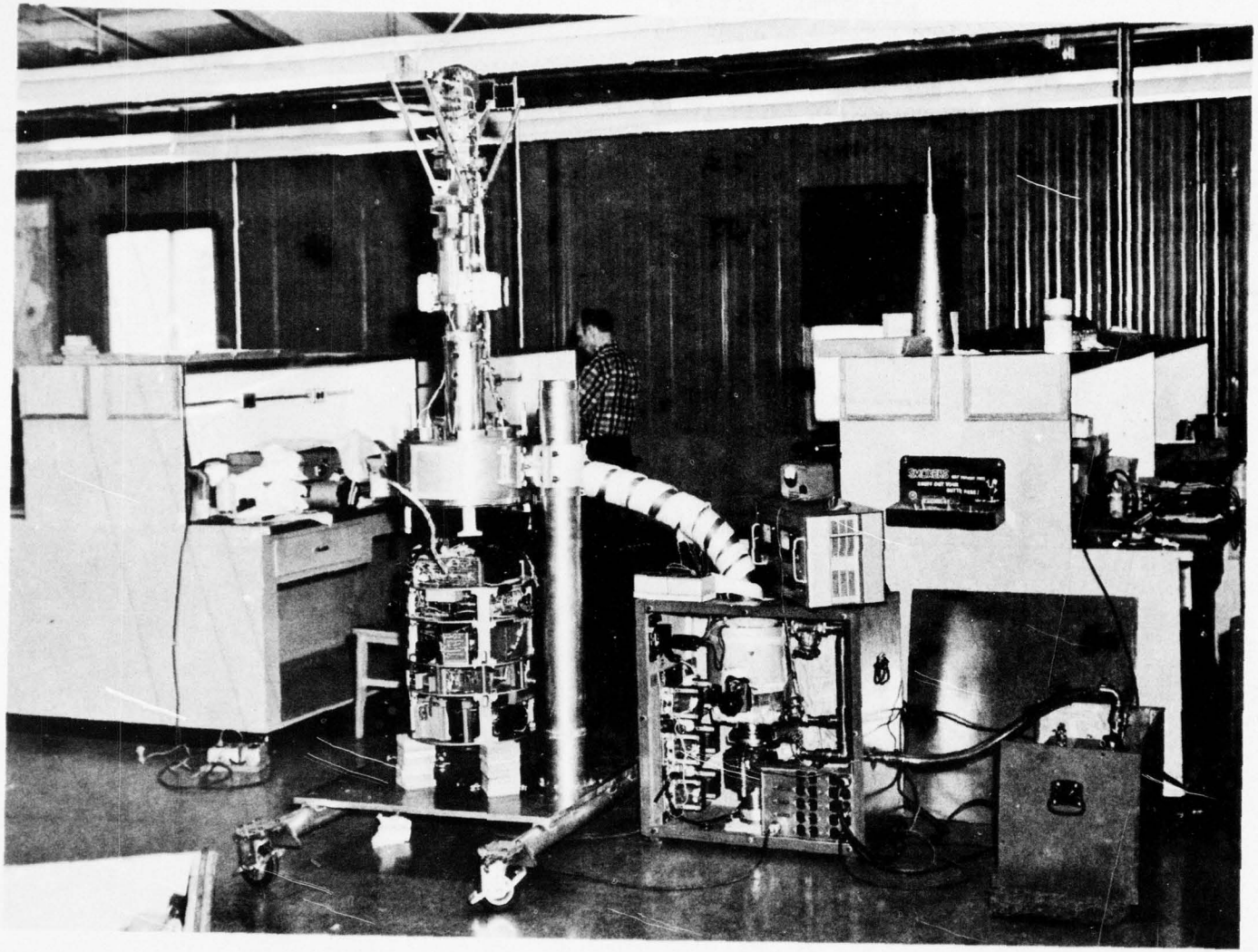


FIG. 25 PORTABLE VACUUM SYSTEM USED ON AEP-II-118

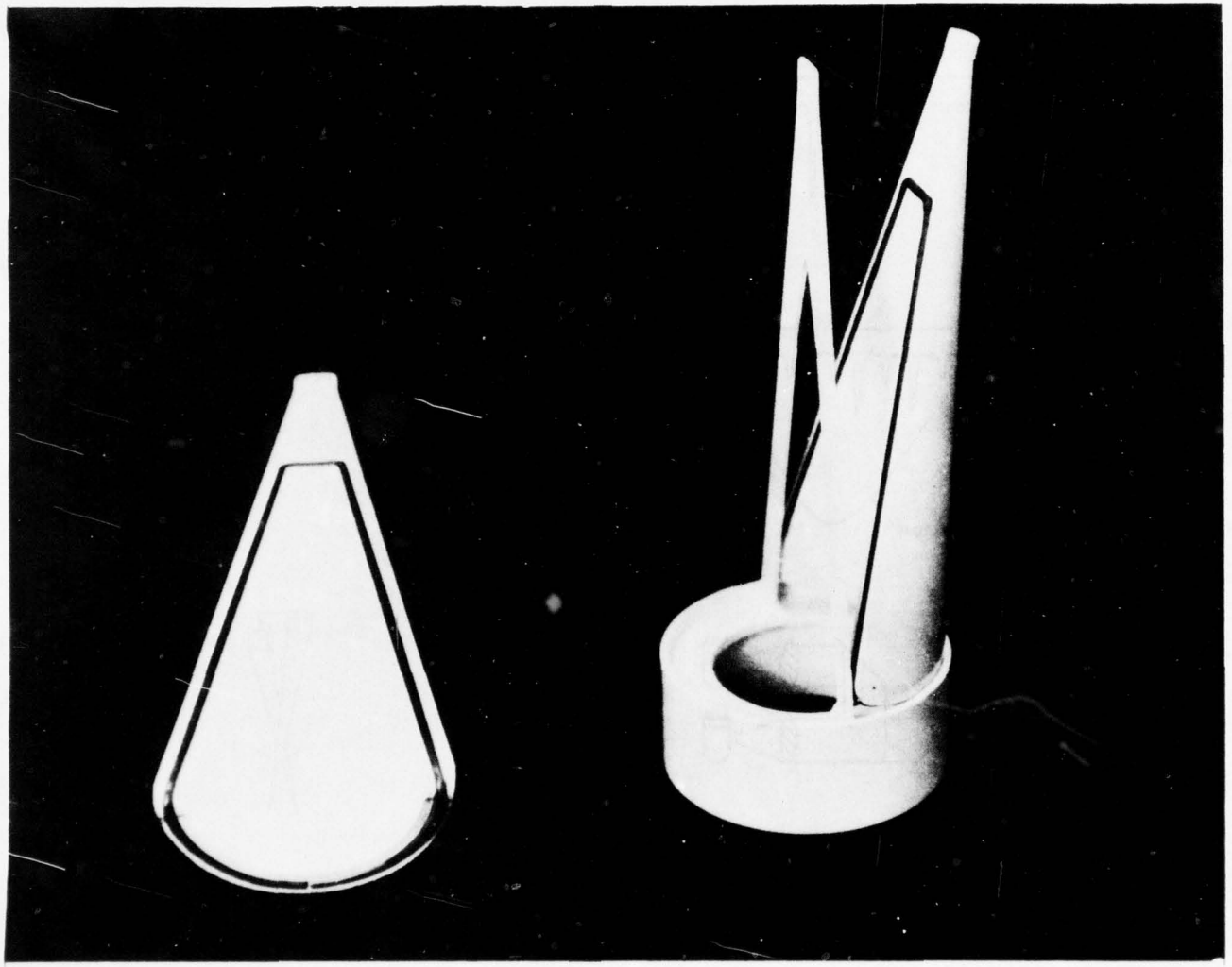


FIG. 26 NOSE CONE VACUUM SEALING FOR AEF-II-118

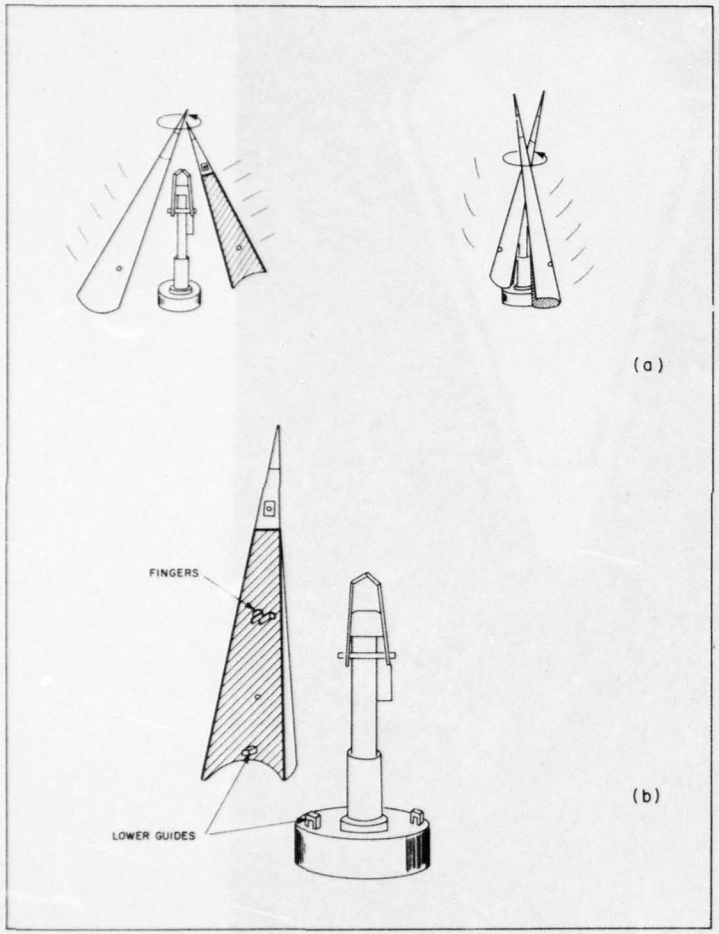


FIG. 27 NOSE CONE DEPLOYMENT RESTRAINTS FOR AEF-II-118

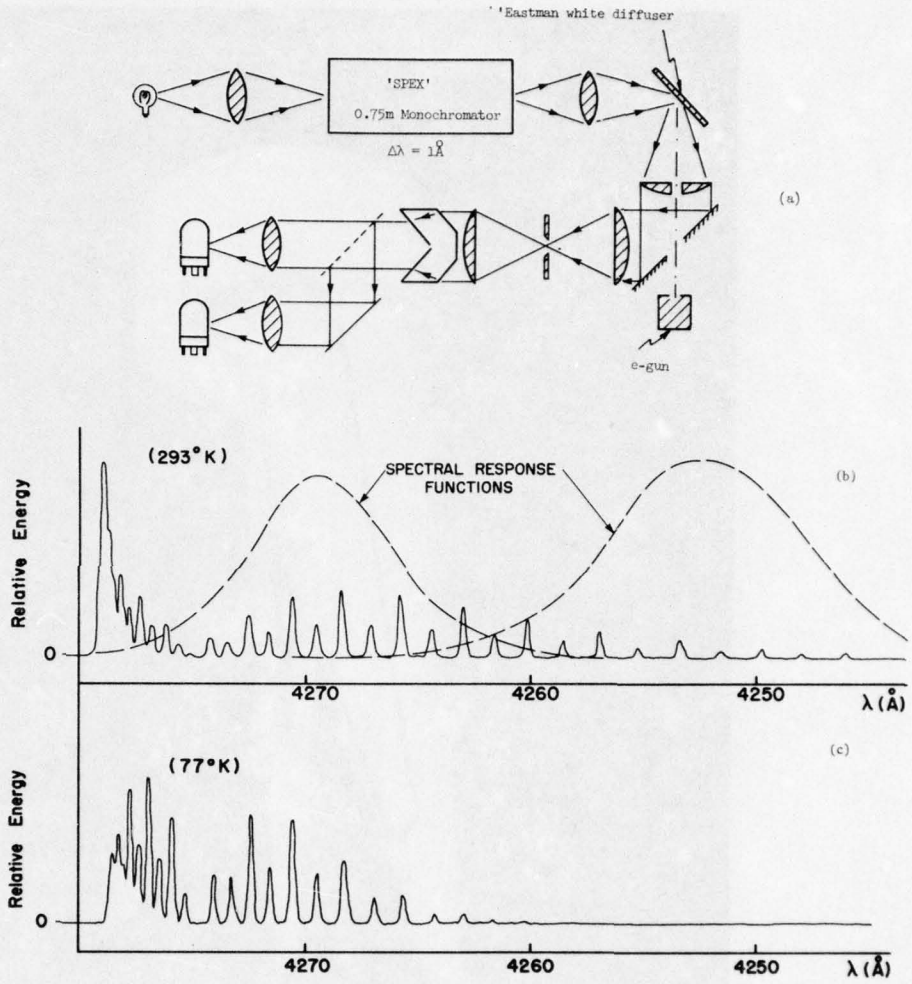


FIG. 28 SPECTRAL CALIBRATION OF EBFP-RTA

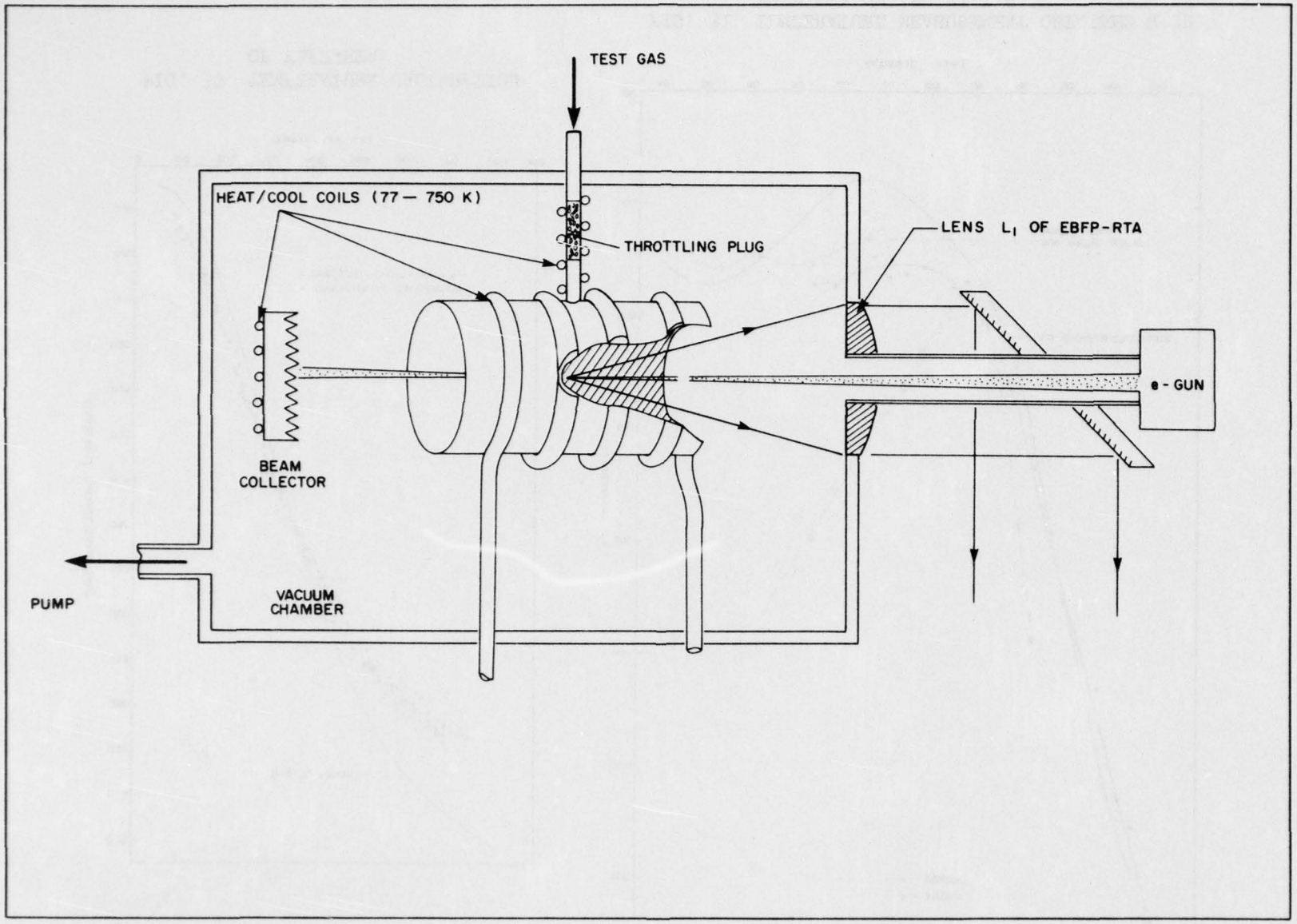


FIG. 29 APPARATUS FOR TEMPERATURE CALIBRATION OF EBFP-RTA

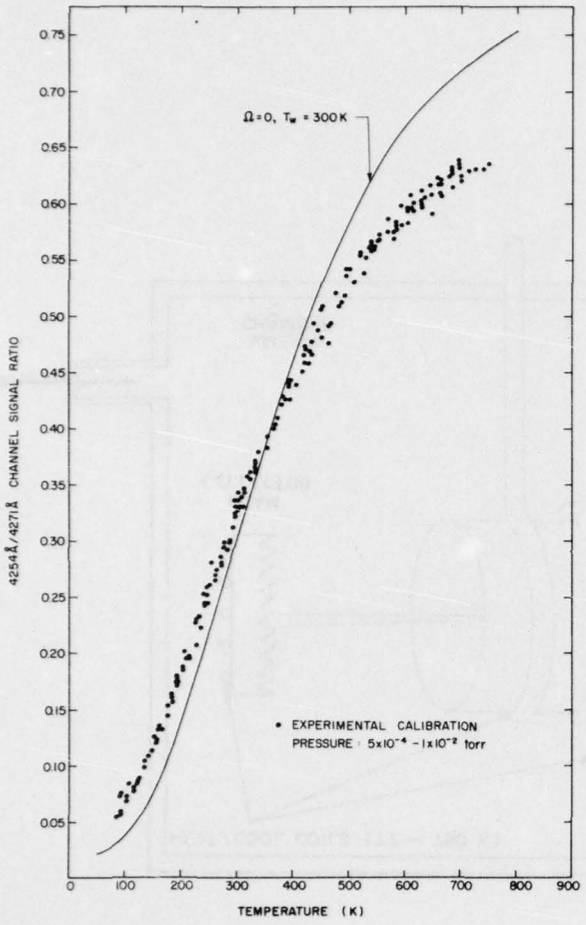


FIG. 30 TEMPERATURE CALIBRATION OF EBFP-RTA

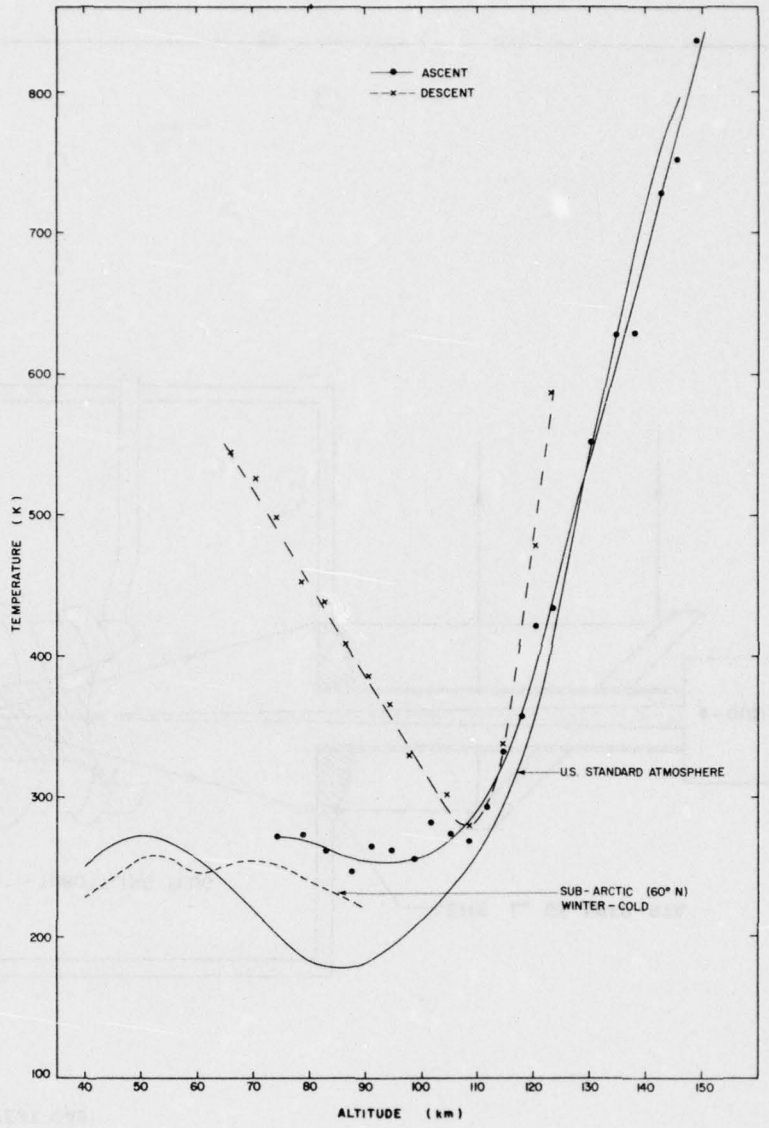


FIG. 31 TEMPERATURE MEASUREMENT OBTAINED WITH EBFP-RTA ON AEF-II-118

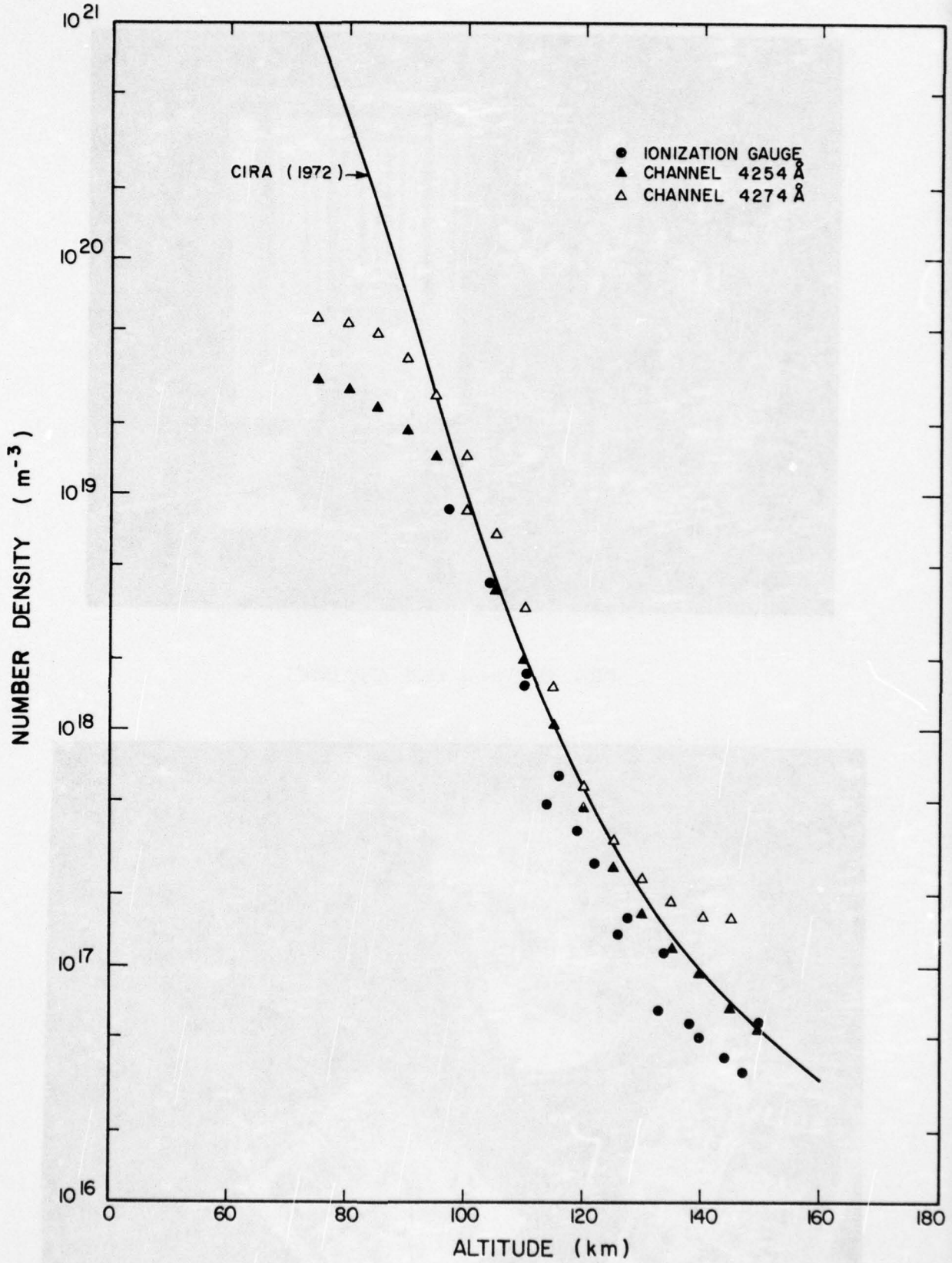


FIG. 32 DENSITY MEASUREMENTS OBTAINED WITH EBFP-RTA ON AEF-II-118

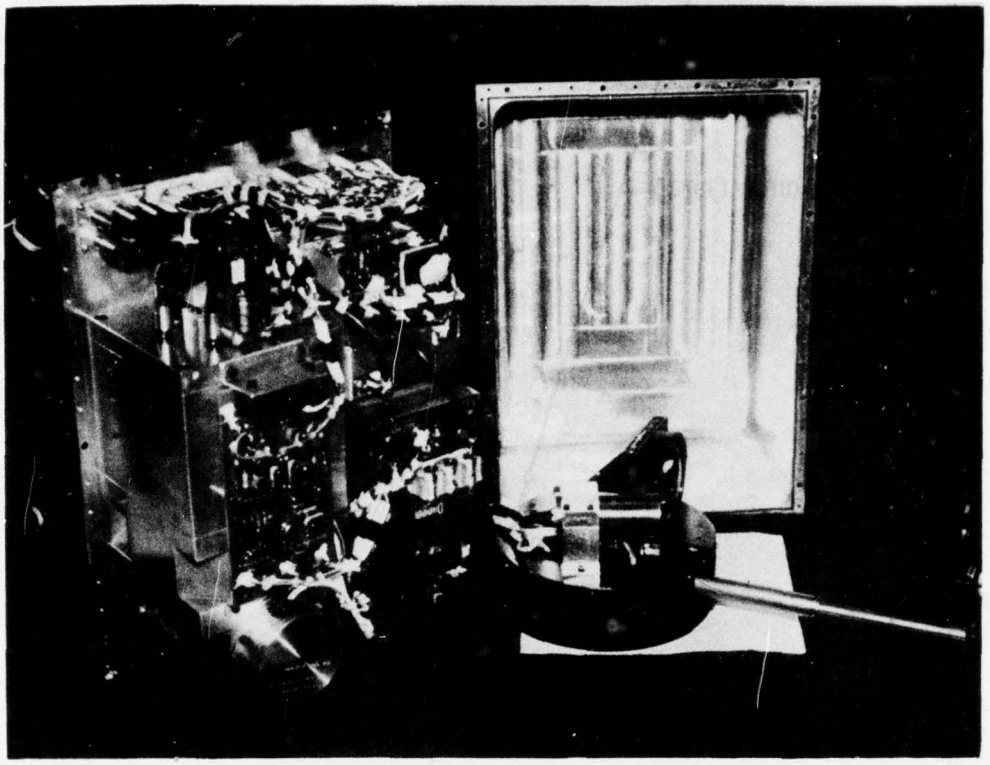


FIG. 33 VB-32 EBFP APPARATUS

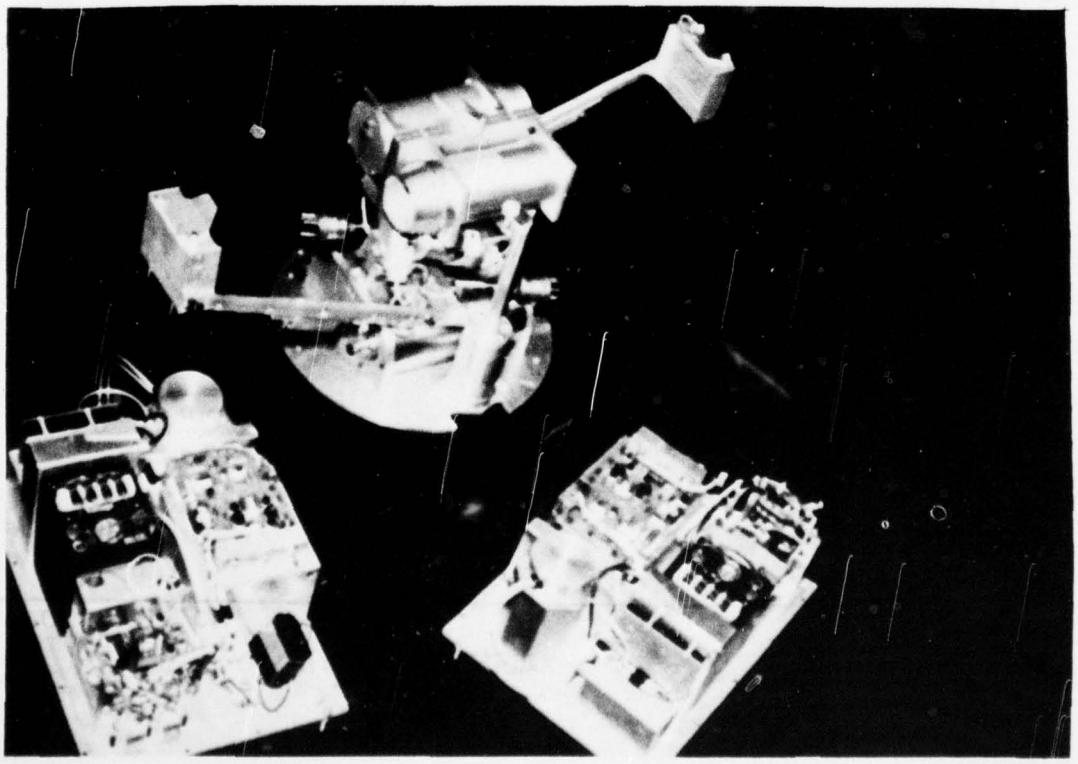


FIG. 34 VB-28 EBFP APPARATUS

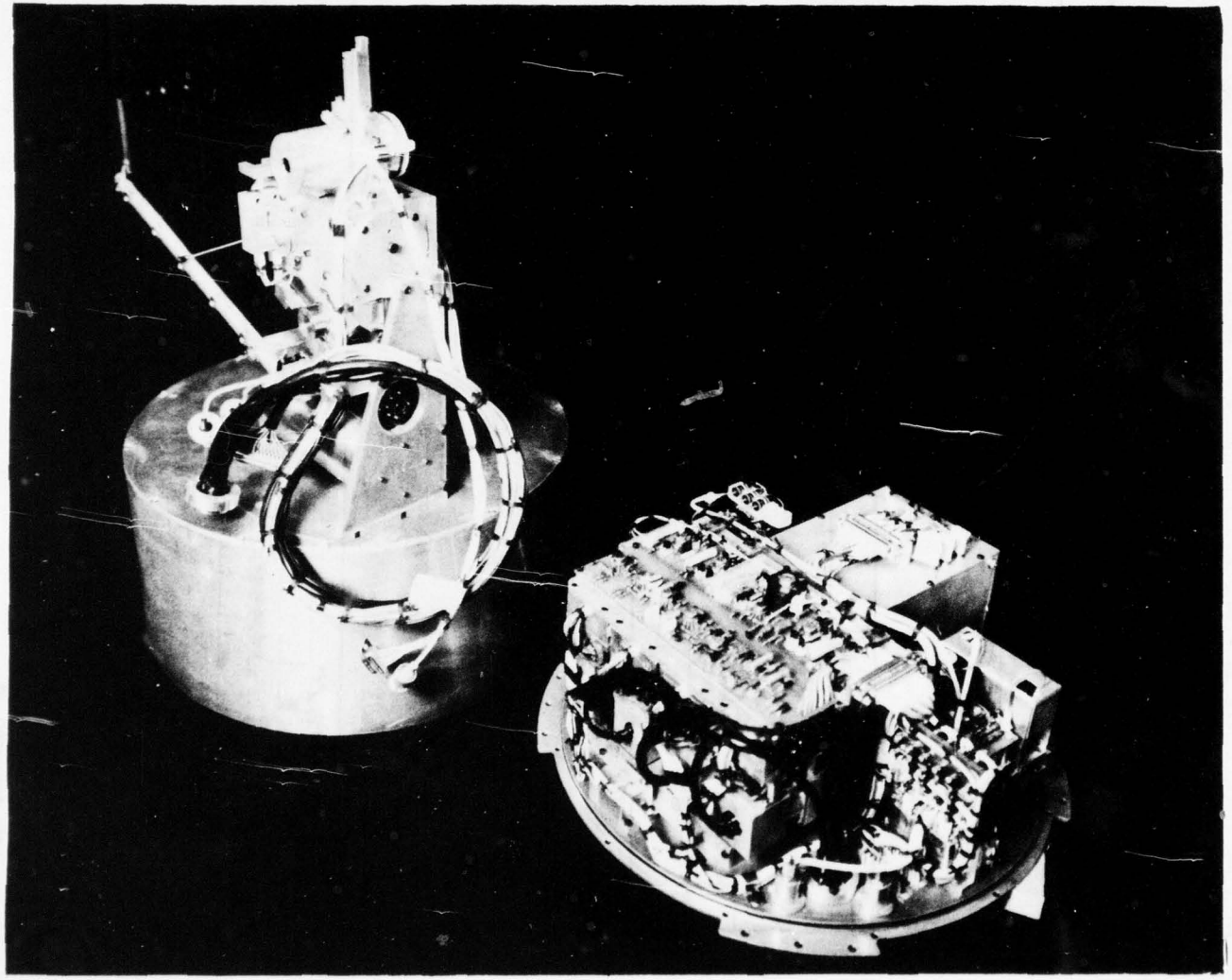


FIG. 35 VB-39 EBFP APPARATUS

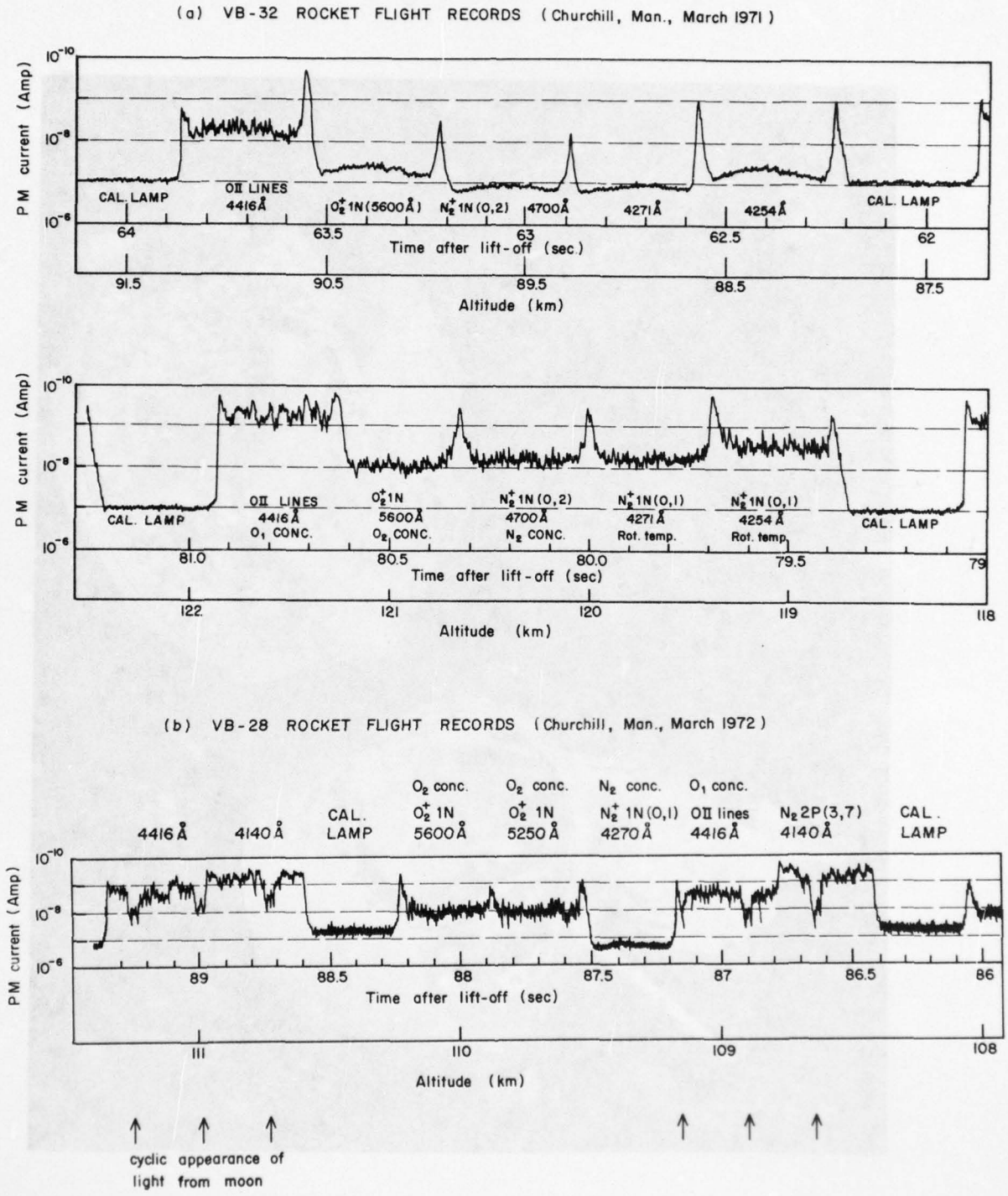


FIG. 36 FLIGHT RECORDS OF TIME SHARING EBFP

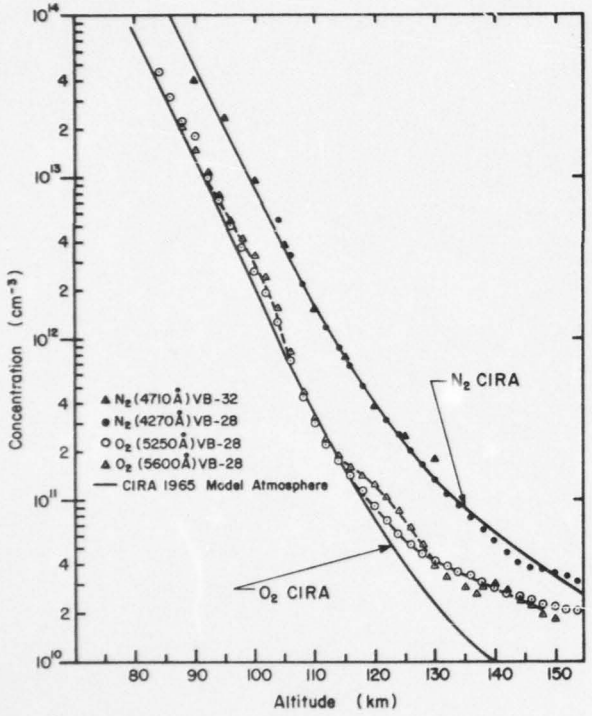


FIG. 37 CONCENTRATION MEASUREMENTS WITH FIBRE OPTIC EBFP

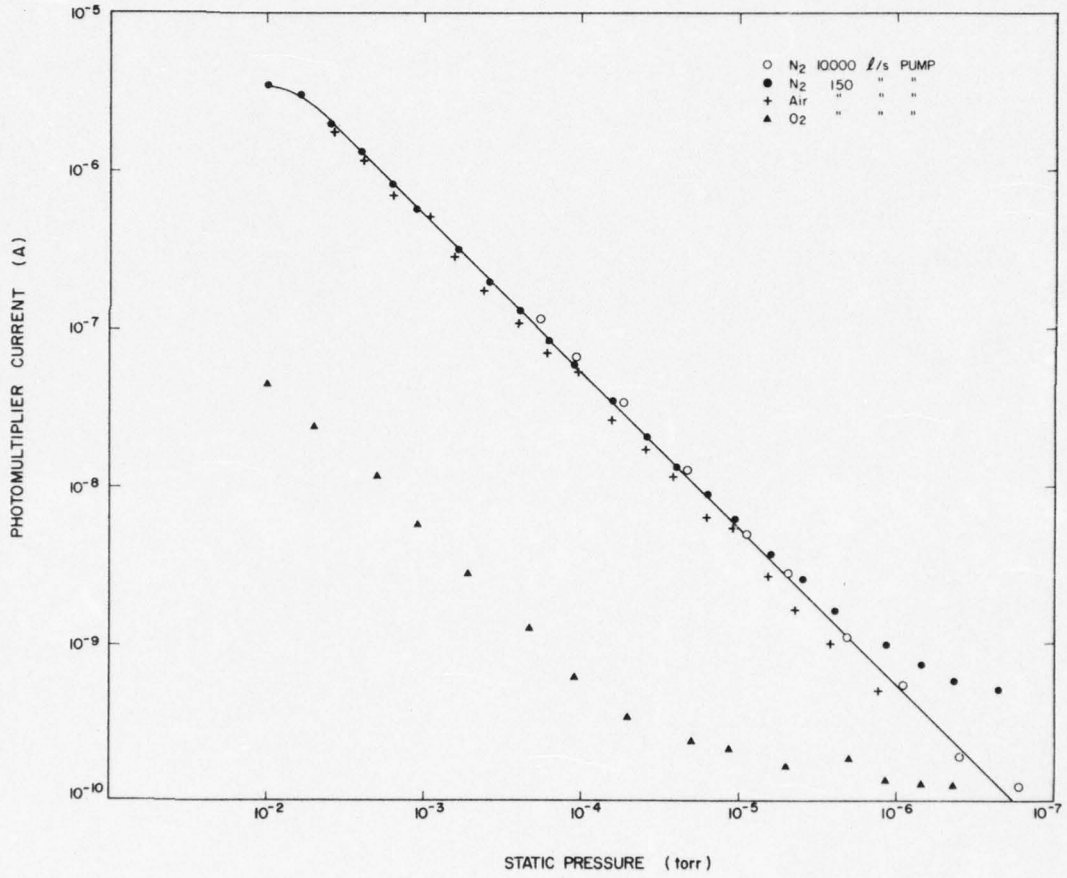


FIG. 38 GAS CALIBRATION OF VB-39 EBFP 4270Å CHANNEL USED FOR N_2 CONCENTRATION MEASUREMENTS

UTIAS REPORT NO. 197

Institute for Aerospace Studies, University of Toronto

DIAGNOSTICS WITH ROCKETBORNE ELECTRON BEAM FLUORESCENCE PROBES

deLeeuw, J. H., Davies, W.E.R., Haasz, A. A., Unger, J. I., 56 pages, 61 figures

1. Electron beam, 2. Fluorescence, 3. Excitation of N_2, O_2 and O_1, 4. Upper atmosphere, 5. Rotational and vibrational temperature, 6. Species concentration

I. deLeeuw, J. H., Davies, W.E.R., Haasz, A. A., Unger, J. I. II. UTIAS Report No. 197

An Electron Beam Fluorescence Probe (EBFP) has been developed for rocket flight applications in the 65-200 km altitude range. The EBFP is a non-perturbing probe which is capable of measuring vibrational and rotational temperatures as well as neutral gas species concentrations remote from the rocket payload. The spatial resolution of the probe is approximately equal to the beam diameter (1-2mm). The instrument employs a 2.5 keV energy electron beam to induce fluorescence in the ambient gas. The resulting radiation is analyzed with a spectrally selective electro-optical detection system. Several versions of the EBFP were flown on Black Brant rockets from Fort Churchill, Manitoba, Canada; the results from these flights as well as the development of the instrumentation are discussed.

Available copies of this report are limited. Return this card to UTIAS, if you require a copy.

UTIAS REPORT NO. 197

Institute for Aerospace Studies, University of Toronto

DIAGNOSTICS WITH ROCKETBORNE ELECTRON BEAM FLUORESCENCE PROBES

deLeeuw, J. H., Davies, W.E.R., Haasz, A. A., Unger, J. I., 56 pages, 61 figures

1. Electron beam, 2. Fluorescence, 3. Excitation of N_2, O_2 and O_1, 4. Upper atmosphere, 5. Rotational and vibrational temperature, 6. Species concentration

I. deLeeuw, J. H., Davies, W.E.R., Haasz, A. A., Unger, J. I. II. UTIAS Report No. 197

An Electron Beam Fluorescence Probe (EBFP) has been developed for rocket flight applications in the 65-200 km altitude range. The EBFP is a non-perturbing probe which is capable of measuring vibrational and rotational temperatures as well as neutral gas species concentrations remote from the rocket payload. The spatial resolution of the probe is approximately equal to the beam diameter (1-2mm). The instrument employs a 2.5 keV energy electron beam to induce fluorescence in the ambient gas. The resulting radiation is analyzed with a spectrally selective electro-optical detection system. Several versions of the EBFP were flown on Black Brant rockets from Fort Churchill, Manitoba, Canada; the results from these flights as well as the development of the instrumentation are discussed.

Available copies of this report are limited. Return this card to UTIAS, if you require a copy.

UTIAS REPORT NO. 197

Institute for Aerospace Studies, University of Toronto

DIAGNOSTICS WITH ROCKETBORNE ELECTRON BEAM FLUORESCENCE PROBES

deLeeuw, J. H., Davies, W.E.R., Haasz, A. A., Unger, J. I., 56 pages, 61 figures

1. Electron beam, 2. Fluorescence, 3. Excitation of N_2, O_2 and O_1, 4. Upper atmosphere, 5. Rotational and vibrational temperature, 6. Species concentration

I. deLeeuw, J. H., Davies, W.E.R., Haasz, A. A., Unger, J. I. II. UTIAS Report No. 197

An Electron Beam Fluorescence Probe (EBFP) has been developed for rocket flight applications in the 65-200 km altitude range. The EBFP is a non-perturbing probe which is capable of measuring vibrational and rotational temperatures as well as neutral gas species concentrations remote from the rocket payload. The spatial resolution of the probe is approximately equal to the beam diameter (1-2mm). The instrument employs a 2.5 keV energy electron beam to induce fluorescence in the ambient gas. The resulting radiation is analyzed with a spectrally selective electro-optical detection system. Several versions of the EBFP were flown on Black Brant rockets from Fort Churchill, Manitoba, Canada; the results from these flights as well as the development of the instrumentation are discussed.

Available copies of this report are limited. Return this card to UTIAS, if you require a copy.

UTIAS REPORT NO. 197

Institute for Aerospace Studies, University of Toronto

DIAGNOSTICS WITH ROCKETBORNE ELECTRON BEAM FLUORESCENCE PROBES

deLeeuw, J. H., Davies, W.E.R., Haasz, A. A., Unger, J. I., 56 pages, 61 figures

1. Electron beam, 2. Fluorescence, 3. Excitation of N_2, O_2 and O_1, 4. Upper atmosphere, 5. Rotational and vibrational temperature, 6. Species concentration

I. deLeeuw, J. H., Davies, W.E.R., Haasz, A. A., Unger, J. I. II. UTIAS Report No. 197

An Electron Beam Fluorescence Probe (EBFP) has been developed for rocket flight applications in the 65-200 km altitude range. The EBFP is a non-perturbing probe which is capable of measuring vibrational and rotational temperatures as well as neutral gas species concentrations remote from the rocket payload. The spatial resolution of the probe is approximately equal to the beam diameter (1-2mm). The instrument employs a 2.5 keV energy electron beam to induce fluorescence in the ambient gas. The resulting radiation is analyzed with a spectrally selective electro-optical detection system. Several versions of the EBFP were flown on Black Brant rockets from Fort Churchill, Manitoba, Canada; the results from these flights as well as the development of the instrumentation are discussed.

Available copies of this report are limited. Return this card to UTIAS, if you require a copy.

AD-A033 680 TORONTO UNIV (ONTARIO) INST FOR AEROSPACE STUDIES F/G 4/1
DIAGNOSTICS WITH ROCKETBORNE ELECTRON BEAM FLUORESCENCE PROBES.(U)
OCT 75 J H DELEEUW, W E DAVIES, A A HAASZ AF-AFOSR-2091-71
UNCLASSIFIED UTIAS-197 AFOSR-TR-76-1408 NL

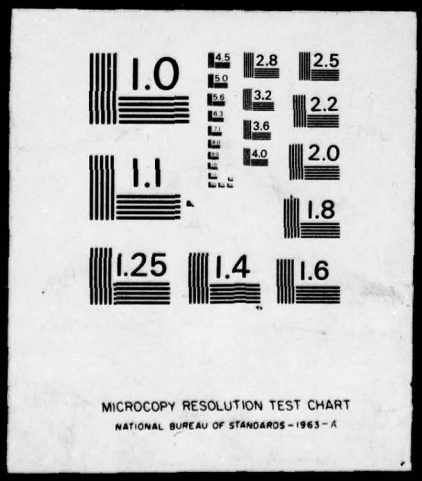
2 OF 2
AD A033680



END
DATE FILMED
2-77

2 OF 2

AD
A033680



SECURITY CLASSIFICATION OF THIS PAGE (When Data Entered)

REPORT DOCUMENTATION PAGE

READ INSTRUCTIONS BEFORE COMPLETING FORM

1. REPORT NUMBER: (19) (18) AFOSR - TR - 76 - 1408
2. GOVT ACCESSION NO.
3. RECIPIENT'S CATALOG NUMBER

4. TITLE (and Subtitle): (6) DIAGNOSTICS WITH ROCKETBORNE ELECTRON BEAM FLUORESCENCE PROBES.
5. TYPE OF REPORT & PERIOD COVERED: (9) INTERIM rept.
6. PERFORMING ORG. REPORT NUMBER: Report No 197

7. AUTHOR(s): (10) J. H. DELEEUW, W. E. R. DAVIES, A. A. HAASZ ↓ J. L. UNGER
8. CONTRACT OR GRANT NUMBER(s): (15) ✓AF - AFOSR[illegible]-2091-71

9. PERFORMING ORGANIZATION NAME AND ADDRESS
UNIVERSITY OF TORONTO
INSTITUTE FOR AEROSPACE STUDIES, 4925 DUFFERIN ST
DOWNSVIEW, ONTARIO, CANADA M3H 5T6

10. PROGRAM ELEMENT, PROJECT, TASK AREA & WORK UNIT NUMBERS
681307
(16) 9781-03
61102F
(17) 93

11. CONTROLLING OFFICE NAME AND ADDRESS
AIR FORCE OFFICE OF SCIENTIFIC RESEARCH/NA
BLDG 410
BOLLING AIR FORCE BASE, D C 20332

12. REPORT DATE: (11) Oct 75
13. NUMBER OF PAGES: 95

14. MONITORING AGENCY NAME & ADDRESS (if different from Controlling Office): (14) UTIAS-197 (12) 98p.
15. SECURITY CLASS. (of this report): UNCLASSIFIED
15a. DECLASSIFICATION/DOWNGRADING SCHEDULE

16. DISTRIBUTION STATEMENT (of this Report)

Approved for public release; distribution unlimited.

17. DISTRIBUTION STATEMENT (of the abstract entered in Block 20, if different from Report)

18. SUPPLEMENTARY NOTES

19. KEY WORDS (Continue on reverse side if necessary and identify by block number)

ELECTRON BEAM
FLUORESCENCE
EXCITATION OF N_2, O_2 and O_1
UPPER ATMOSPHERE
ROTATIONAL AND VIBRATIONAL TEMPERATURE
SPECIES CONCENTRATION

20. ABSTRACT (Continue on reverse side if necessary and identify by block number)

An Electron Beam Fluorescence Probe (EBFP) has been developed for rocket flight applications in the 65-200 km altitude range. The EBFP is a non-perturbing probe which is capable of measuring vibrational and rotational temperatures as well as neutral gas species concentrations remote from the rocket payload. The spatial resolution of the probe is approximately equal to the beam diameter (1 - 2 mm). The instrument employs a 2.5 keV energy electron beam to induce fluorescence in the ambient gas. The resulting radiation is analyzed with a spectrally selective electro-optical detection system. Several versions of the

DD FORM 1 JAN 73 1473 EDITION OF 1 NOV 65 IS OBSOLETE

UNCLASSIFIED 178920
SECURITY CLASSIFICATION OF THIS PAGE (When Data Entered)

KB

EBFP were flown on Black Brant rockets from Fort Churchill, Manitoba, Canada; the results from these flights as well as the development of the instrumentation are discussed.